The Role of Mechanical Stress and Deformation in Lithium Metal Battery Design

By

Guangyu Liu

A dissertation submitted in partial fulfillment
of the requirements for the degree of
Doctor of Philosophy
(Mechanical Engineering)
in the University of Michigan
2018

Doctoral Committee:

Professor Wei Lu, Chair
Professor Christian Lastoskie
Professor Donald Siegel
Professor Anna Stefanopoulou

Guangyu Liu

gyliu@umich.edu

ORCID iD: 0000-0003-2413-6087

Acknowledgements

First and foremost, I sincerely thank Prof. Wei Lu, my advisor and committee chair, for giving me the unique opportunity to work on many different yet fascinating research areas. During my PhD study, Prof. Lu not only guided me through the basic training of lithium ion and lithium metal battery research, but also taught me how to tackle a complicated mechanical engineering problem in general. His dedication to research, passion to work, and critical thinking helped me greatly in sharpening my thoughts and developing my skills.

I am extremely thankful to my committee members, Professor Anna Stefanopoulou, Professor Donald Siegel, and Professor Christian Lastoskie, for inspiring me with more complete picture of my research. Their insightful suggestions and comments have been detrimental for the completion of the work presented in this dissertation.

I would like to thank my colleagues in my lab for their help and friendship. A special thank you to Dr. Xianke Lin for introducing me into the lithium battery degradation research during my first year of PhD. I would also like to say thank you to my past colleagues from GM/UM Advanced Battery Coalition for Drivetrains for their support over the years, from whom I learned experimental skills and modeling techniques for battery study.

Finally, I would like to thank my family and friends for the love and support that made me through the difficult times. They have always been my source of energy and resolution.

The author would like to acknowledge the support provided by the U.S. Department of Energy, General Motor, Denso, and Department of Mechanical Engineering at University of Michigan.

Table of Contents

List of Tables

List of Figures

Abstract

To meet increasing energy density demand of consumer electronics, electric vehicles and grid-scale storage, lithium metal has been proposed to be the anode choice for the next generation of lithium ion battery due to its high theoretical capacity and low electrochemical potential. However, the dendrite growth during the lithium deposition process has been the most critical issue that prevents the commercialization of lithium metal battery because it can not only cause capacity loss but also lead to internal short circuit and safety hazard. At the same time, SEI growth would also lead to active material loss and impedance failure.

In this dissertation, first, the failure mechanisms of lithium metal battery were studied in details with in-situ experiments. The results showed that dendrite growth was highly coupled with SEI formation, and at large current density, the sharp tips of lithium dendrites would penetrate separator and eventually lead to short circuit. Second, electrochemical models were developed to simulate the concurrent evolution of dendrite morphology and SEI layer, and suggested that uniform SEI layer and smaller SEI resistivity would be beneficial to form stable lithium surface morphology during deposition. Third, linear stability analysis was conducted for suppressing lithium dendrite with thin film to show that the mechanical blocking strategy would only be effective if the thin film thickness and modulus meet a critical design criterion. Fourth, a new lithium dendrite suppression strategy using piezoelectric feedback mechanism was proposed, and a proof of concept design was implemented and tested with experiments. The results showed that using a piezoelectric separator can effectively suppress lithium dendrite

growth and prevent short circuit during the cycling of lithium metal battery. In the last part, a novel battery pack design consisting of many micro batteries carried by an inert fluid was proposed to achieve higher energy and power density comparing to conventional battery pack design, and provide unique capabilities such as battery scaling with vehicle life, superfast refilling, heat dissipation and ongoing battery recycling.

Chapter 1

Introduction

1.1 Background on Lithium Metal Battery

Using lithium metal as anode is not a new idea. In fact, one of the earliest rechargeable lithium battery designs in the 1970s employed lithium metal as anode [1]. However, this design was soon given up as researchers discovered dendrite formation during the lithium deposition process, which is the inherent process when charging the battery. Instead, in 1991, SONY released the first commercial Li-ion battery which implemented a $Li_{1-x}CoO_2$ / C design, and since then lithium ion battery has gain tremendous development in application across different fields, from commercial electronics to electric vehicles [2]. The recent decades has seen rapid increase in global energy consumption and CO_2 emission, which reminds people to think about reducing fossil fuel consumption to mitigate global warming. Meanwhile the uncertainty in international politics has made it clear that innovation in energy storage research is not only crucial to national energy security, but also to meet the increasing energy and power demand. Under this background, vehicle electrification has gained momentum in many countries, for example, France committed to banning new petrol and diesel car sales by 2040 [3].

The emergence of electric vehicle has poses new challenges for lithium ion battery design as it take more power and energy to keep a car moving while also make sure the driver is safe under all accounts. However, the recent volumetric energy density increase has been mainly driven by

sophisticated cell engineering, including active particle size distribution control and current collector architecture changes, which has been reaching the limits [2]. It is now widely accepted that we need new battery strategies to meet the growing demand for energy density and power density, thus new battery chemistries beyond the conventional lithium ion battery design need to be developed. Under such circumstances, lithium metal battery, i.e. using lithium metal as anode, was proposed again.

Figure 1.1 Renault's Zoe electric car as one of France's electric car commitments [3]

Theoretically, lithium metal is the most attractive anode choice for lithium based battery, as it has the highest theoretical capacity (3860 mAh/g), and the lowest electrochemical potential (-3.04 V vs. standard hydrogen electrode). Imagine if the anode of lithium ion battery can be successfully replaced by lithium metal, the specific energy can be increased by more than 40%, up to 400 Wh/kg, which would greatly reduce the battery pack weight for all applications [4]. In

electric vehicle application, this means one can drive the car for 40% mileage further than the current battery could allow. This will make even the smaller electric vehicle BMW i3, which now has a design mileage after one full charge of 114 miles, much more attractive to the customers. One can never emphasize too much about how important the sales growth is for a new market such as electric vehicle, as history lesson was written by General Motor for their failed EV1 program due to poor market reaction [5]. Now if we move to a more advanced chemistry, lithium air battery can reach energy density of more than 1100Wh/L, which would put the battery on the same level of energy density of gasoline, and at which point it would only be reasonable for most people to drive electric vehicles instead of an internal combustion engine powered car.

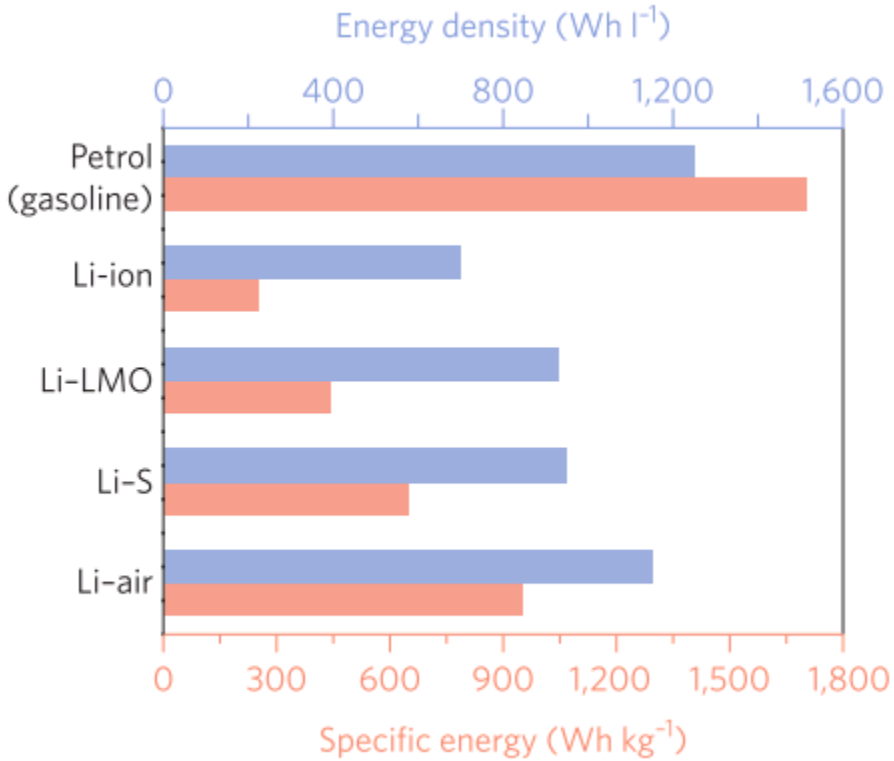

Figure 1.2 Energy density and Specific energy comparison between different lithium based battery chemistries and petrol [4].

As lithium ion battery are approaching the limit of their capabilities, the topic of lithium metal anode was revived both in academics and industry. In this thesis, the concept of lithium metal battery refers to the structure where the anode of the lithium ion battery is lithium metal battery and the cathode material is conventional transition metal oxide intercalation materials such as $Li_{1-x}CoO_2$ (LCO) etc. A typical lithium metal battery would consist five components inside the packaging enclosure: two current collectors for each electrode, lithium metal foil as anode, metal oxide porous electrode as cathode, and a separator, which could be conventional polymer based porous separator with liquid electrolytes or novel solid electrolyte as separator.

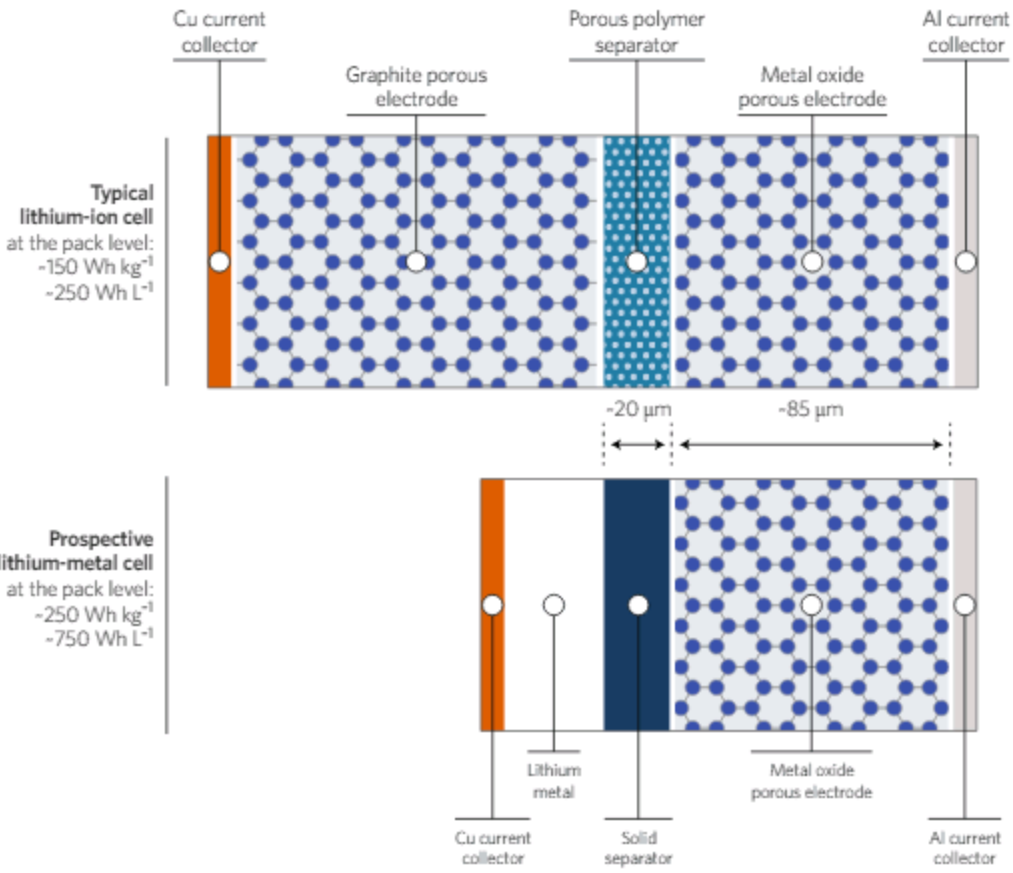

Figure 1.3 Comparison between the typical structures of lithium metal battery and lithium ion battery [6].

1.2 Motivation

As promising as lithium metal battery is, stable cycling of lithium metal is still a very challenging task to accomplish. This dissertation is dedicated to understand the failure mechanisms of lithium metal battery from the basic physics and chemistry, and propose solutions to improve the lithium metal battery design.

The initial experimental study was designed to identify the key failure modes of lithium metal battery during cycling, and analyze how each failure modes are coupled. In order to achieve these objectives, in-situ experiments were designed to observe the morphology evolution of

lithium metal surface during cycling, and the electrochemical behavior of the cell at the same time. Material characterization was conducted to provide insights for the surface reaction and the transport process.

The modelling work focuses on simulating the discovered failure mechanisms of lithium metal battery. To fully capture the coupling effect of different failure mechanisms, this study would dive into the detailed electrochemistry equations and build the model from ground up. The methodology of this modeling procedure could also benefit future model development for other novel battery chemistry. As the backbone of the model is the basics of electrochemistry, the model framework is less chemistry specific, and can be adapted to analyze similar battery chemistry by parameterizing the model for the new battery chemistry.

The new material proposal was aimed to provide an alternative method to improve lithium metal battery design in addition to the existing literatures. It would also demonstrate how the experimental study and modeling work to understand the failure mechanism can help profoundly on how to discover new designs for lithium metal battery, or battery in general. The procedures to test the new material that were developed in this dissertation would also serve as example test plans for future study on similar topics.

The battery pack design work was to demonstrate how to think on the system level and utilize the cell level knowledge to improve battery pack design. This dissertation emphasizes the importance of system requirements and the methodology used in this work can be instructional to design battery packs.

1.3 Literature Review

In this section, the contemporary researches on lithium metal battery were reviewed. First, the challenges faced by researchers when designing lithium metal battery were discussed. Second,

the models proposed in the past to describe the phenomena in lithium metal battery were compared. Last, different design proposals for lithium metal battery were summarized.

1.3.1 Challenges of Lithium Metal Battery

It has always been challenging to use lithium metal as anode safely, as lithium morphology would tend to be dendritic and mossy during the deposition process [7]. The dendritic morphology also means that during the lithium dissolution process, many dendrites will lose contact with the lithium substrate as the dissolution is not always uniform, leading to what was called “dead lithium”, which is essentially the loss of active material [8]. To deal with the issue of dead lithium, researchers usually deploy excess lithium in the cell design, which inevitably decreases the energy density and cancelled one of the major benefits of lithium metal battery [9]. On the other hand, dendrite growth during the deposition process would result in potential hazard of short circuit [10]. This is because as the dendrites grow, the dendrite tip will get into contact with the separator, and eventually penetrate the separator. This was also the major reason that lithium metal anode was abandoned for the initial commercial lithium based battery [11]. Dendrite formation is one of the most challenging issue of lithium metal battery and has been a major research topic in the energy storage field for the past decade.

At the interface between lithium and liquid electrolyte, a passive film called solid-electrolyte-interphase (SEI) would form due to the side reaction between lithium and the components of electrolyte [12]. Taking the popular EC/DMC $LiPF_6$ electrolyte for example, ROCO2Li and ROLi species would form at first, and further reduce to Li_2CO_3 [13]. If there was not dramatic surface morphology change of the lithium, the SEI would have stabilized the surface and prevent further side reaction. This is usually what happens on the surface of the graphite anode in a typical lithium ion battery, where the surface of graphite is relatively consistent during each

cycle given the current density is not too large [14]. In this case, the SEI layer would preserve a double layer structure, with a thinner inorganic layer beneath the slowly growing outer organic layer [15]. As characterized by researchers, the growth rate of SEI layer on graphite surface would decrease as cycle numbers goes up [16], thus explaining the logic behind the formation cycles for a new assembled battery (formation cycles are low current cycles completed for new assembled batteries before the batteries are put into practical application).

However, the coupling of dendrite growth and SEI formation makes things more complicated for lithium metal SEI. The morphology change of lithium metal upon deposition and dissolution are both so large that the SEI layer cannot accommodate. This leads to the breakdown of SEI layer near the dendrite growing points. Due to the instability of lithium exposed directly in the electrolyte, new SEI would form to repair the cracked surface film [17]. This coupled phenomenon would keep repeating itself, resulting to a very quick impedance growth over time [18]. In fact, many lithium metal battery designs suffered from impedance failures before the dendrite could develop enough to cause short circuit [19]. The dendrite growth behavior and how it is coupled with the SEI growth is highly dependent on the applied current density, and lower current would usually result in less dendritic structure [20]. This makes sense because when the current is lower, the dendrite surface velocity is also lower, thus the SEI formation can be quick enough to repair the cracked surface film so that the lithium can be confined by a more complete SEI layer for most of the time. However, using a low current also goes against the initial intention of introducing lithium metal as anode, as high power density was the demanding feature. Therefore forming a more compact SEI even under high current density has been a major direction of improving lithium metal battery design.

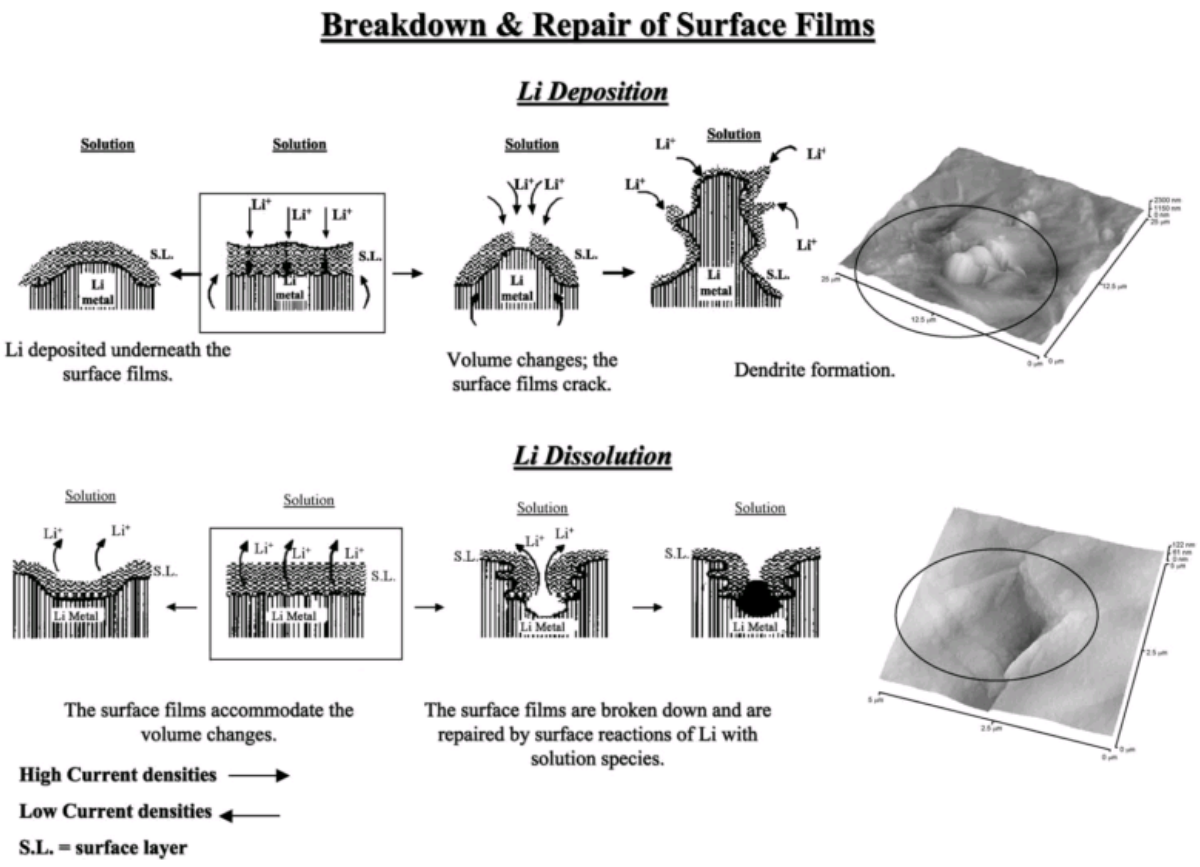

Figure 1.4 Coupling between dendrite growth and SEI formation for lithium metal anode [17].

In order to understand the detailed process of the dendrite growth, numerous efforts were made to visualize the evolution of lithium surface morphology during deposition and dissolution. The traditional way of understanding surface morphology is to use AFM, SEM, TEM and variations of microscopic instruments observe the anode surface after cycling the lithium metal battery [21], [22]. The in-situ observation of lithium dendrite growth have become more and more popular as the technology progresses. With the help of high definition cameras, optical footages are now clear enough to show vividly how the morphology changes over time under different current densities and with different electrolyte [23]–[25]. Efforts have also been made in micro scale in situ observation [26], [27]. Recently, the Nobel Prize winning cryo-TEM was

used to observe lithium dendrite to reveal the atomic structure of lithium dendrite [28]. These studies greatly enriched people's understanding of the failure mechanisms of lithium metal battery.

1.3.2 Models of Lithium Metal Battery

Various models have been proposed to simulate lithium dendrite formation and growth during the past decades. The majority of existing models are based on the work of Barton and Bockris in the analysis of silver dendrites [29], which argued that lithium deposition is faster on protrusions because of the larger spherical diffusion flux comparing to the flux toward a flat surface. This flux leads to narrowing of the dendrite tip, while surface tension prevents infinite dendrite thinning [30]. Monroe and Newman[31] applied this approach in a parallel-electrode lithium/polymer cell and derived a one-dimensional model for an isolated needle-like dendrite. In subsequent papers, they further extended the model to include the effect of mechanical pressure on dendrite growth and evaluated the effectiveness of using bulk solid electrolyte to block dendrite growth [32], [33]. A series of COMSOL simulation were done based on this model to reveal the redistribution of lithium over cycling [34], [35]. Chazalviel [36] introduced a model of dendritic growth in a high electric field where the growth rate is determined by the space charge developed upon the anion depletion near the electrode. This model requires a high current above the critical level to trigger dendrite formation, thus does not apply to those dendrites observed under low currents. The model was supplemented by follow-up papers to include surface non-uniformity as a trigger of dendrite formation under small currents [37], [38]. Yamaki *et al.* [39] assumed lithium as a fluid and analyzed three types of dendrite shape depending on the value of the surface tension and pressure. Chen *et al.* [40] developed a

nonlinear phase-field model to investigate the dendritic pattern as a function of applied voltage and initial electrode surface morphology.

The dendrite growing process was also considered as the roughening of a planar surface, which often involved a Mullins-Sekerka type stability analysis [41]. Aogaki and Makino conducted a linear stability analysis on the electrodes in diffusion-limited electrodeposition under galvanostatic condition, predicting faster powder formation and smaller powder size given increasing current density and decreasing bulk concentration and temperature. A similar result was achieved by Sundstrom and Bark in the study of the electrode morphological stability during electrodeposition with a stagnant binary electrolyte by solving the stability problem numerically as an eigenvalue problem [42]. Haataja et al. developed a formalism to predict morphology evolution during electrodeposition with arbitrary supporting electrolyte, which was used to study the effect of additives in the electrolyte on the electrodeposition process [43], [44]. A complete review of lithium dendrite modeling work can be found in the article by Li et al [45].

1.3.3 Designs of Lithium Metal Battery

To improve the lithium metal battery design, researchers have tried various strategies including electrolyte engineering, deposition host design, solid electrolyte, coating layer etc. [46]. Among these strategies, electrolyte gains most focus as electrolyte innovation for lithium metal anode may also be applicable for more advanced lithium based batteries in the future, while also providing insights for other battery electrolyte design. SEI composition is widely believed to depend on the components of electrolyte. Bis(fluorosulfonyl)imid (FSI^-) anion was found to form a robust SEI layer on the surface of lithium metal [47], [48]. LiTFSI and LiFSI salts are two promising candidates for next generation electrolyte of lithium metal battery [49], [50]. DOL and DME solvents exhibit good SEI formation and long term stability, and are

proposed as solvents to combine with LiTFSI and LiFSI salts to serve as electrolyte [51]. Recently, 'solvent-in-salt' electrolyte was explored, in which the salt concentration is high and the salt holds the dominant position in the electrolyte rather than the solvent [52]. The high concentration leads to rapid formation of SEI layer and also prevents salt depletion even at high rate, thus can protect the lithium electrode and allow high current cycling (10mA/cm^2) with good Coulombic efficiency (97% over 500 cycles) [53]. Additives with higher reduction potentials than the salt and solvents would usually help reinforce SEI formation [54]. Fluorinated compounds were extensively investigated as HF would help form LiF inorganic layer quickly on the lithium surface, which would greatly improve the SEI robustness [55], [56]. Halogenated salt additives would to form fluorine-rich products in SEI and making the lithium easier to go through the SEI layer and deposit underneath [57], [58]. $LiNO_3$ is an additive that was found effective in Li-S batteries [59] and the concept was implemented for general lithium metal batteries [60]. Artificial SEI layers and coating structures are also efficient approaches to protect lithium metal anode [61]. Nanostructured hollow carbon nanospheres were proved to be useful in this case due to the high conductivity and superior cycling stability [62]. Ceramic coating [63] and Li_3N based protecting layer films [64], [65] were also proposed to act as artificial SEI layers.

Solid electrolyte is another popular approach to prevent lithium dendrite growth and side reactions of lithium [66]. The basic idea is to mechanically block the propagation of lithium dendrite using the solid material, either inorganic ceramic electrolytes or solid polymer electrolytes [4]. Solid electrolytes were found effective when exhibit high modulus, sufficient lithium ion conductivity, electrochemical stability and low resistance [67]–[71]. Inorganic ceramics excel at mechanical strength and ionic conductivity in general, however suffer at interfacial resistance as a good surface adhesion with lithium metal cannot be easily formed [72].

Solid polymer electrolytes have better adhesion and electrochemical stability [73] comparing to inorganic ceramics, but their mechanical modulus is much smaller, which might not be strong enough to block the dendrite growth [37]. The low ionic conductivity is another issue with solid polymer electrolyte, thus improving ionic conductivity has been a major focus for the researchers [74], [75]. Notable strategies that showed promising results include combination of solid polymer electrolyte and inorganic ceramics [76]–[78], reinforcement using block copolymers [79], [80], nanoparticle embedment [81]–[83].

1.4 Dissertation Organization

In this dissertation, Chapter 2 discusses the failure mechanisms of lithium metal battery which were studied in details with in-situ experiments. Chapter 3 and Chapter 4 are dedicated to develop models to describe and analyze the lithium dendrite growth and why it is hard to suppress dendrite formation effectively. Chapter 5 discusses a new strategy to suppress lithium dendrite growth by using a piezoelectric separator. Chapter 6 proposes a novel battery pack design that consists of many micro batteries carried by an inert fluid.

In Chapter 2, an in-situ experiment setup was built to investigate the failure mechanisms of lithium metal battery. The in-situ cell was able to be monitored through an optical window during lithium deposition and stripping processes, which reveals the morphology evolution of lithium surface during cycling of lithium metal battery. With the help of potentiostat, the impedance changes were also measured in between cycles. The in-situ study shows that the lithium dendrite growth and impedance growth are the two major failure mechanisms of lithium metal battery. For the first case, direct evidence was found that the separator could be penetrated by the lithium dendrite, suggesting that dendrite growth could lead to potential short circuits. For the second case, it was found that the impedance grows very quickly during the first few cycles

of the in-situ cell. The coupling of these two mechanisms were confirmed with in-situ study that the SEI would be penetrated by the lithium dendrite at multiple points and new SEI would form which would lead to more impedance growth. The in-situ study results motivates the development of modeling work to simulate and analyze lithium dendrite growth and SEI formation.

In Chapter 3, a model was developed that enables simulations of concurrent coupled lithium dendrite growth, SEI formation and growth on the dendrite surface, dendrite penetration of the SEI layer, and SEI regrowth. The concept of SEI coverage density is introduced, which is conceptually similar to SEI thickness but broader. SEI and dendrite growth interacts with each other by evolving dendrite morphology, stretching of SEI by the dendrite surface, and the effect of evolving SEI thickness (coverage density) on lithium deposition reaction. The model shows that even under low current density, small protrusions on lithium surface can still grow into dendrites by penetrating SEI and causing inhomogeneous electrical resistance on dendrite surface. It was found that dendrite growth shows two distinct stages: fast acceleration during SEI penetration, and stable growth after reaching an equilibrium SEI thickness at the dendrite tip. Under low current density, increasing current scales up the growth rate of dendrite without much shape change. High current density causes dendrite morphology to change significantly, forming a needle shape. The model also shows that local SEI defects/inhomogeneity can induce dendrite formation and growth. The results suggest that flat lithium surface, uniform SEI layer, and low SEI resistivity are important to reduce dendrite formation.

In Chapter 4, linear stability analysis were conducted for the popular lithium dendrite suppression strategy, that is, thin film coating. A modified Butler-Volmer equation was developed to describe the effect of mechanical blocking layer and surface tension based on free

energy change. It was found that the mechanical effect on the reaction kinetics has two contributions: shift of the equilibrium and scale of the reaction current density. A full model coupling the diffusion and electro-migration driven dendrite growth and implemented the stress-impacted kinetics was implemented. The perturbation analysis provides the solution to the full model in the large wavenumber domain with the assumption of fully supported electrolyte and elastic deformation. The results show that the addition of the coating film can decrease the critical wavenumber and the effectiveness of suppression depends on the thickness and modulus of the thin film. Thus the mechanical blocking strategy would only be effective if the thin film thickness and modulus meet a critical design criterion. This motivates the exploration of new strategies for lithium dendrite suppression.

In Chapter 5, a piezoelectric feedback mechanism was proposed as a new strategy to suppress lithium dendrite growth and to design lithium metal battery safely. Polarized polyvinylidene fluoride (PVDF) film was used as separator in lithium metal battery setup to demonstrate this concept. When PVDF film was deformed due to local surface instability of the deposited lithium, piezoelectric overpotential would form to cancel the spherical diffusion effect, and suppress further growth of the initial protrusion. Comparing to mechanical blocking strategies, piezoelectric feedback strategy is more effective against small scale local instabilities, thus provide more protection against separator penetration during lithium deposition. Optical in-situ cell study showed that the polarized PVDF film can confine the lithium deposition into a flat surface, even when starting from an uneven surface, while non-polarized PVDF film would fail under the same condition. Coin cell results confirmed that the piezoelectric feedback mechanism were effective under realistic lithium metal battery setups. The study suggests the application of

piezoelectric material in lithium dendrite suppression as a new research direction of lithium metal battery.

In Chapter 6, a novel battery system composed of many micro- or nano-scale batteries was proposed. Each battery is a self-contained Li-ion micro-battery enclosed in an insulating shell, and can charge/discharge wirelessly or through contacts. Thousands of such batteries are carried by an inert fluid to form a power fluid to drive an electric vehicle. This power fluid can be stored in the tank and replaced easily with a fully charged fluid by refilling once its energy is depleted. The system can provide better energy density, higher power density, and extremely fast "charging" within minutes. The architecture eliminates the large over-capacity design in the current battery packs, significantly reducing the weight and cost. It would also enable progressive improvements of vehicle performance by replacing the micro-batteries. The battery system has flexible geometry, and therefore can essentially go into a storage space of any geometry, allowing uniform design of battery configurations for diverse applications.

1.5 Contributions

The contributions of this dissertation include:

- In-situ evidence of separator penetration by the lithium dendrite in Chapter 2. This is one of the first direct observations of how the lithium dendrite penetrates the separator and leads to a short circuit in real time. Together sharp tips of the lithium dendrites found in the SEM study, the potential hazard of lithium dendrites should be still emphasized even when they seems harmless in macro scale as they can penetrates separator in the micro scale.
- A concurrent model to simulate coupled dendrite growth and SEI penetration in Chapter 3. This is the first model that captures the coupling effect of the two major

failure mechanisms in lithium metal battery. The model was able to explain the reason that a uniform SEI with low resistivity would help form stable surface morphology during lithium deposition.

- A design criterion for thin film used for lithium dendrite suppression based on linear stability analysis in Chapter 4. To develop this criterion, first, the pressure modified Butler-Volmer equation was derived from an energy point of view that quantifies the reaction over-potential caused by deformation. The design criterion explained why a lot of thin film designs failed to suppress lithium dendrite due to inadequacy of thickness and modulus.
- A new strategy to suppress lithium dendrite growth using piezoelectric separator in Chapter 5. The piezoelectric feedback mechanism can be explained with the piezoelectric over-potential caused by the local deformation of the separation during the lithium dendrite formation. PVDF was identified as a suitable material for this strategy and proved to be effective in lithium dendrite suppression and short circuit prevention. This strategy opens up a new direction in lithium metal battery design.
- A novel battery pack design consists of many micro batteries carried by an inert fluid in Chapter 6. This pack design possesses many advantages over traditional pack design: higher power and capacity density, battery scaling with vehicle life, superfast refilling, efficient battery operation, ongoing battery recycling, heat self-dissipation and flexible geometry.

Chapter 2

In-situ Study of Lithium Metal Battery Failure Mechanisms

2.1 Introduction

In this chapter, the detailed failure mechanisms of lithium metal battery was discussed based on our in-situ observation of the lithium deposition and dissolution process. The in-situ cell design and fabrication was demonstrated. Methods to prepare the materials and assemble the in-situ cell were included, and the testing setup was explained. Our results showed that lithium metal battery has two major failure modes: separator penetration by dendrite and impedance failure. The in-situ observation also confirmed the strong coupling between these two failure mechanisms, suggesting that in the follow up modeling work, it cannot be neglected.

The in-situ cell design is mainly inspired by some commercial cells with quartz windows for optical microscope analysis as well as some self-made systems [25], and the intuition is to create an optical window in the traditional polymer shelled testing cell, so that the cross section of the lithium metal can be clearly observed by a microscope. During cycling the cell, the current, voltage, and impedance can be measured by a potentiostat, providing a complete picture of how the cell electrochemical behavior is evolving over time as well as the surface morphology change in real time. A major discovery presented in this chapter is the clear footage of the process of dendrite penetrating the separator.

2.2 Methods

The fabrication of in-situ cell was completed in the machine shop of ME department, University of Michigan, with the instruction from the fabrication specialist Kent Kruss (the author wants to thank him for his generous help). A 3D design of the in-situ cell parts is presented in Figure 2.1.

First, PTFE plastics block was milled into the shape of the outer shell. PTFE material was chosen for it is easy to cut and can provide a little buffer space for the assembly process thanks to its softness. The pocket dimension and O-ring rove depth has to be controlled precisely so that the other parts can fit into the slots tightly. PVC plastics bar was milled and used as the electrode holders and spacers, and the material was chosen based on its high stiffness and hardness so that it won't suffer from deformation or scratches during repeatedly assembly. Both PTFE and PVC meet the requirements that no side reaction would occur even exposed to the electrolyte components. The electrode holders' dimension is crucial to the convenience of later assembly. Here the dimension were controlled such that the combined parts of two electrode holders and the spacer has a slightly smaller dimension than the dimension of the pocket of the outer shell. The cover of the cell was made out of aluminum with a quartz glass as the optical window. Aluminum was chosen for it is easy to mill a flat surface while also provide enough strength for the bolt tightening action and good stability under different environment conditions. The cell is sealed using Viton O-rings, which showed great resistance to chemical etching. Two copper screws served as the electrode poles to conduct current from electrodes inside the cell to outside of the cell.

To assemble the in-situ cell, lithium metal foil was cut into pieces so that they can be fitted into the electrode holder slots. A copper wire was used to connect the lithium metal to the copper

screw and conduct the current. The electrolyte used was 1M $LiPF_6$ in EC/DMC (1:1) purchased from Sigma Aldrich. Before each assembly, the inner parts and the pocket of the outer shell was cleaned using DMC solvent to remove any residues from previous experiments. The separator used was from Celgard which is a commercial PE (Polyethylene) based separator. The assembly of the cell was always conducted in an Argon filled glovebox. An assembled view of the cell was shown in Figure 2.2.

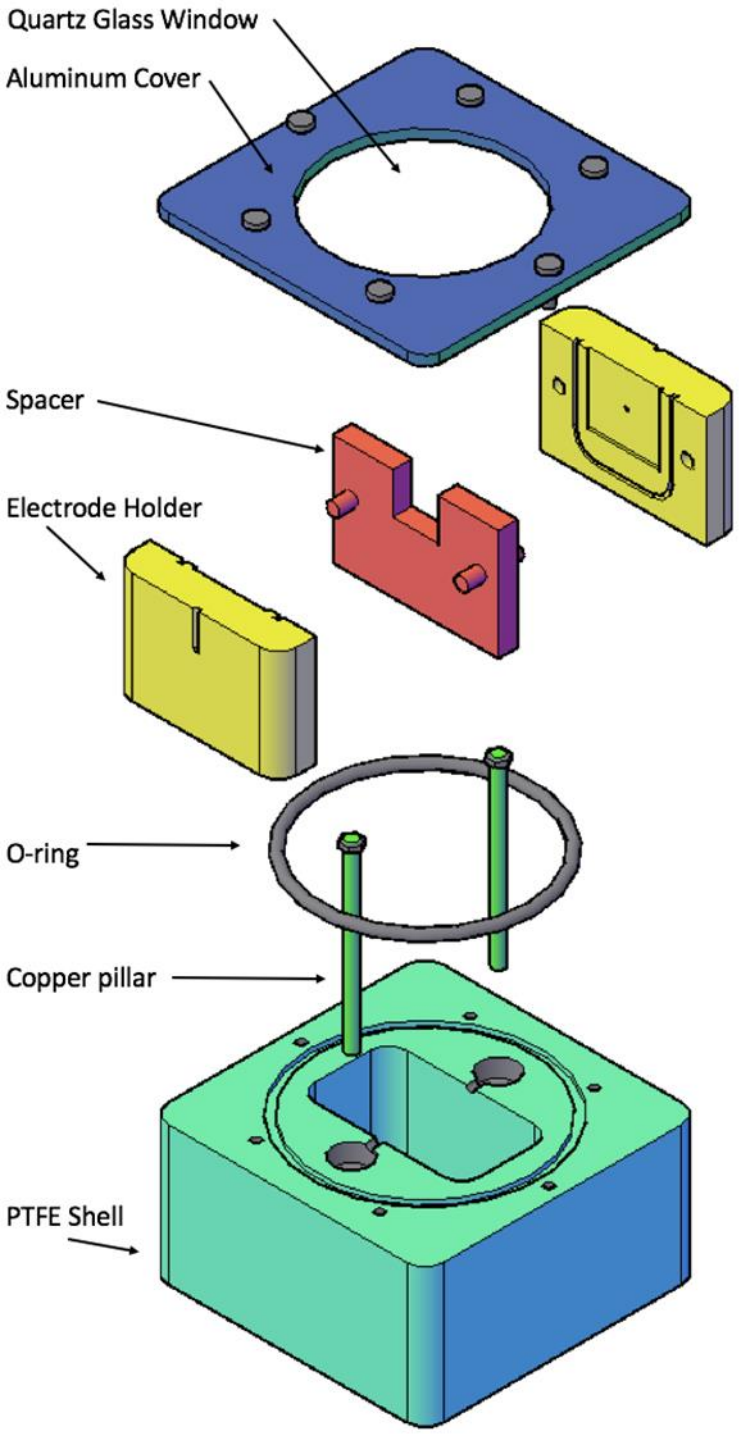

Figure 2.1 Separate view of in-situ cell parts.

Electrochemical testing of in-situ cell was conducted using a VMP3 Biologic potentiostat under galvanostatic condition. EIS measurements were done every five cycles between frequencies 1 Hz to 10 kHz. The data was further processed using MATLAB. During the electrochemical testing, an optical microscope was used to capture the evolution video for the lithium surface through the optical window of the in-situ cell.

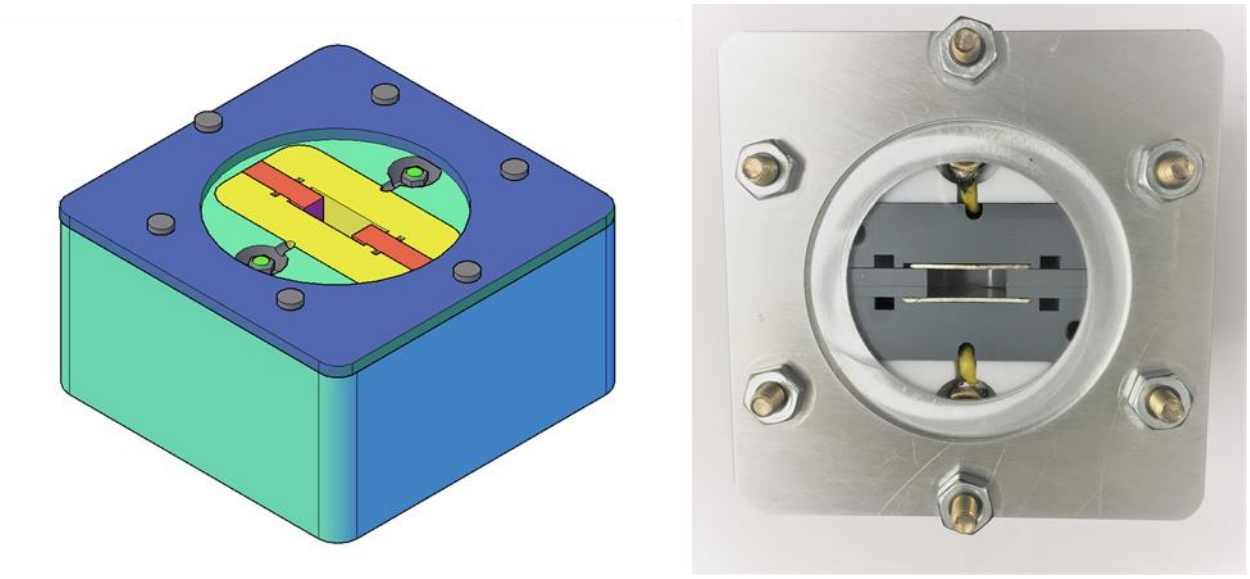

Figure 2.2 Assembled view of in-situ cell. Left: 3D design view. Right: Top view of the in-situ cell.

2.3 Results

Figure 2.3 shows the snapshots of the typical evolution of lithium surface under the current density of 1 mA/cm^2. The dendrite initiates at multiple points on the lithium surface when the current is first applied. Then as these structures grow into the dendritic shapes, they will merge into each other and form ‘bush-like’ mossy lithium. Notice there is a large volume expansion associated with the lithium deposited.

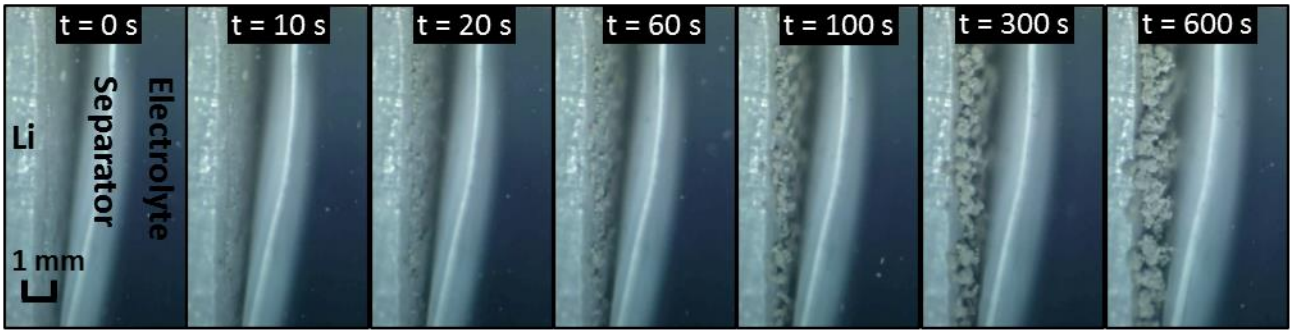

Figure 2.3 Lithium surface morphology evolution under current density 1mA/cm^2.

Figure 2.4 shows how the dendrite penetrates the separator. Although we can't directly see the lithium deposited under the Celgard separator, the darker color indicates that the deposition results in close contact between the lithium surface and the separator. After a certain time (15mins), the lithium dendrite penetrates the separator and quickly grows into a 'bush'. This dendrite can break from the lithium substrate and become 'dead' lithium (Figure 2.5), or it can continue grow and lead to short circuit once it reaches the other electrode (in this setup another separator was put on the counter electrode to prevent this dangerous situation from happening).

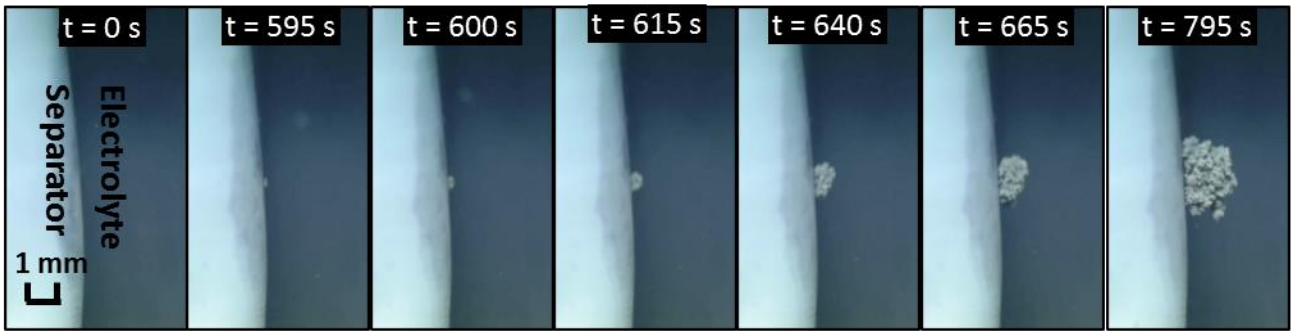

Figure 2.4 Penetration of separator by the lithium dendrite.

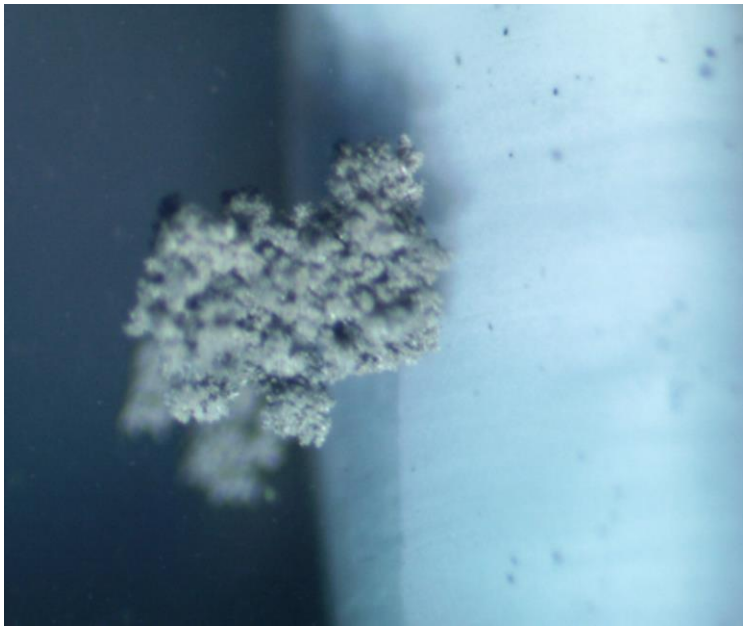

Figure 2.5 Part of the penetrated dendrite broke away from the substrate and floats on top of the electrolyte.

Under SEM (Figure 2.6), we can see that although seemingly harmless in micro-scale, these lithium dendrites have sharp ‘needle’ shapes in nano-scale. These sharp tips of the dendrites keep pushing the separator until penetration happens at certain local points.

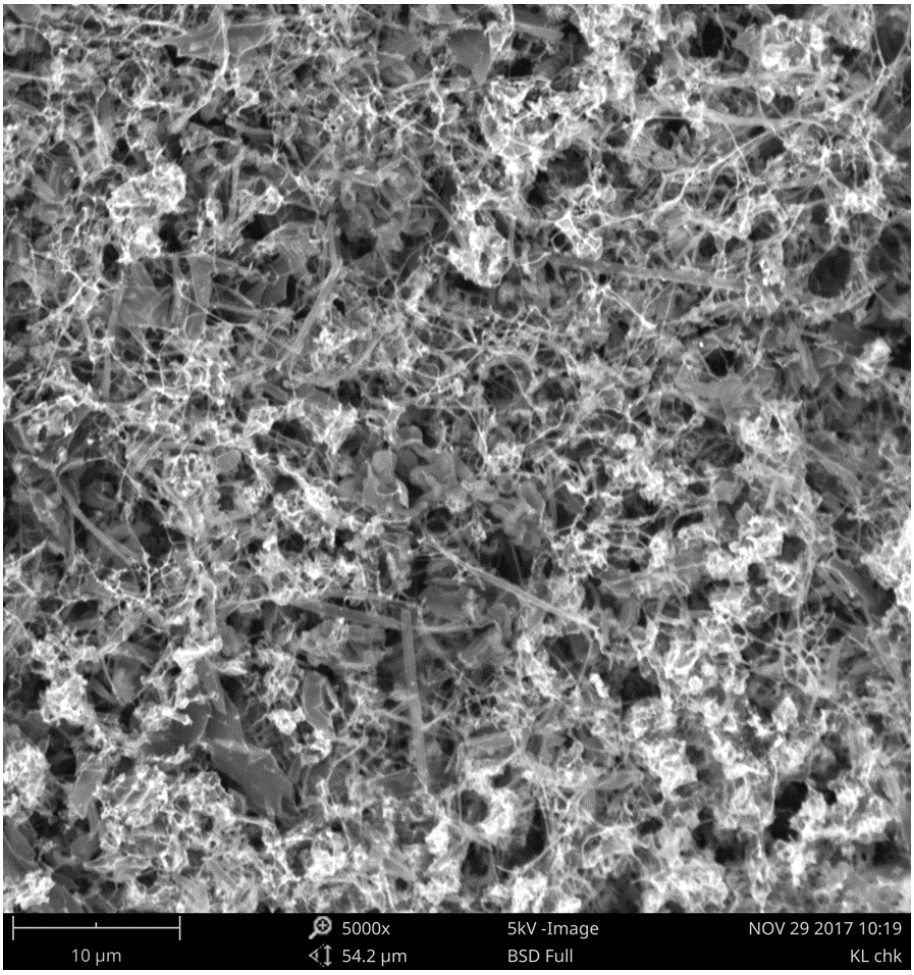

Figure 2.6 SEM image of the lithium surface shows the sharp tips of dendrites.

The short circuit failure is only one of the failure modes of lithium metal battery. When cycled under galvanostatic conditions, the EIS measurement also suggests a massive impedance increase after just 5 cycles (Figure 2.7). This is due to the formation of SEI layer on the lithium surface during the deposition. The growth of dendrites will penetrate the SEI at the tip area and thus expose the fresh lithium again and result in more SEI formation. Our in-situ study confirms that dendrite growth and impedance increase are the two major reasons that causes failure in lithium metal battery cycling. Here the EIS measurements was done after each complete deposition cycle, where in each cycle, the constant current was applied for a fixed period of 10

mins in one direction and then switch to the reverse direction for lithium dissolution. As in a symmetric cell, there is no definition of state of charge, one can use the period in between the cycles as reference stage for the impedance measurement.

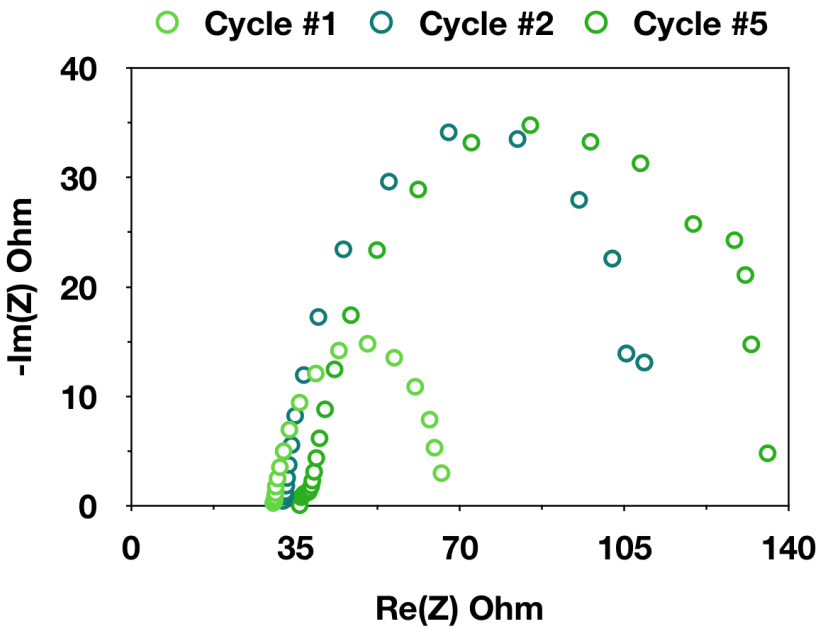

Figure 2.7 EIS measurement shows the rapid impedance of the in-situ cell increase over cycles.

The voltage response was also measured during the deposition process. As there would be separator penetration in some cases which would cause fluctuation in voltage signals, only the ones that survived 10 minutes was included in Figure 2.8. When the current is first applied, the voltage quickly spikes to about 0.6 V which corresponding to the initiation of dendrites. Afterwards it would drop a little before rising again due to the blocking of the separator. The variation across trials is likely caused by the variation of impedance in each assembly. As the assembly process of in-situ cell is purely by hand, the tightness of the contact between the electrode and the current collector can vary, leading to different contact resistance. However, the trend preserves across each measurements.

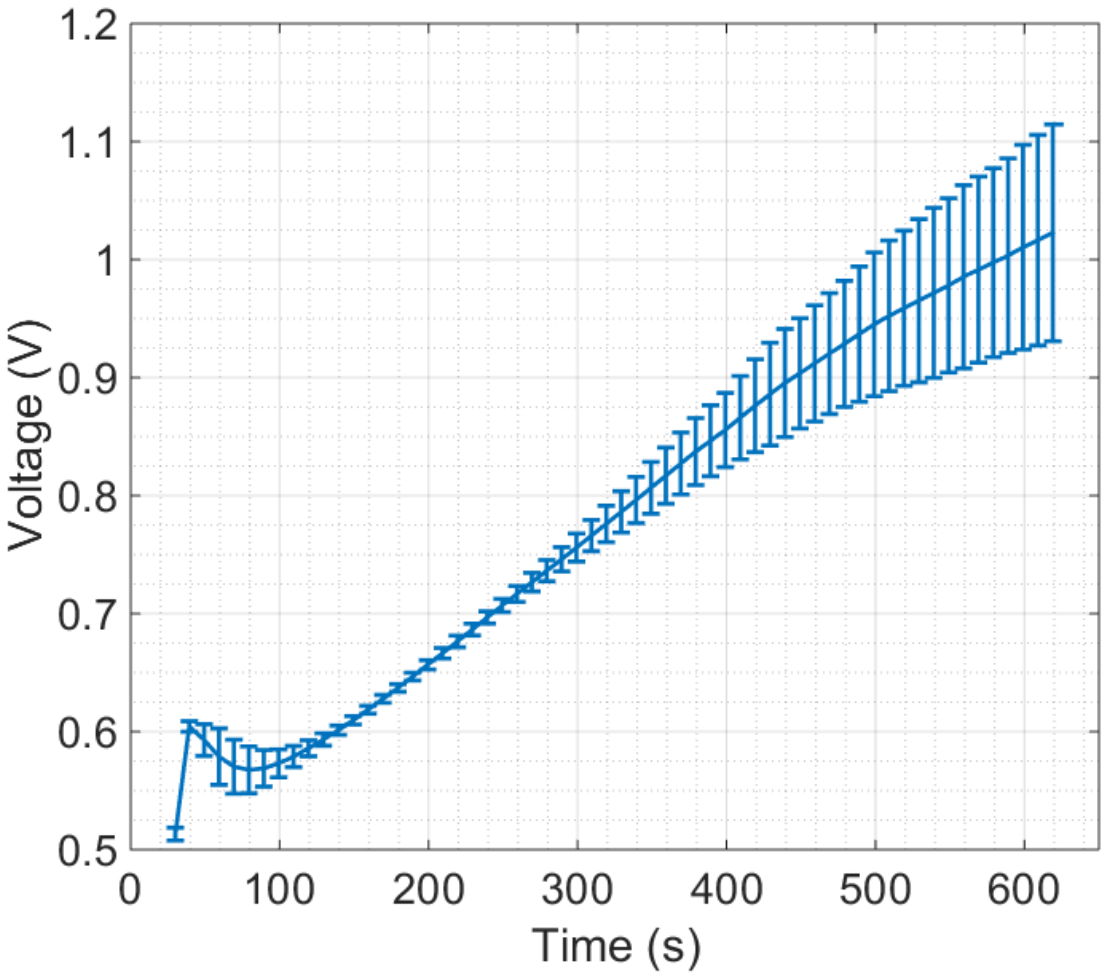

Figure 2.8 Voltage over time when applied with constant current density 1mA/cm^2. The variation of measurements is likely due to the fabrication process of symmetric cell as each assembly may vary slightly in impedance due to different contact resistance.

The reverse cycle was investigated with a similar setup. Figure 2.9 shows that the color of the bush changed from bright to dark as the lithium is stripped off the substrate. This implies that the dendrite growth and SEI formation is highly coupled. As the volume expansion during the lithium deposition and dissolution is so large, the SEI layer is not flexible enough to keep in pace

with the surface movement of the lithium dendrite. Thus the SEI would break and reform, leading to more impedance growth.

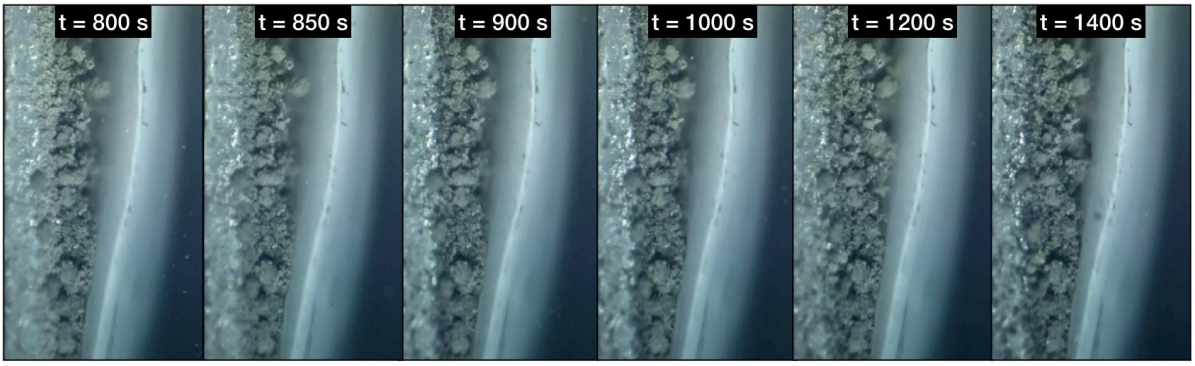

Figure 2.9 Snapshots of lithium dissolution process.

2.4 Conclusion

In this chapter, in-situ observation of lithium dendrite growth was conducted with an optical in-situ cell. It was found that dendrite penetrating separator and impedance increase are the two major failure mechanisms of lithium metal battery. After initial formation, the dendrites will grow into bushes given a typical current density. During this process, the SEI layer keeps breaking down and new SEI would be formed to repair the surface film. Due to this coupled evolution, the impedance would grow quickly. At certain point, the cell may experience impedance failure, that is, the impedance is too large for the cell to support any reasonable power loads. On the other hand, there would be cases where the dendrite tip penetrates the separator before the impedance failure happens, then the cell would have a safety hazard as a short circuit could easily happen when the dendrite keeps growing and reaches the counter electrode. During both lithium deposition and dissolution period, some dendrites would break away from the

substrate and is lost in the electrolyte, which would result in Coulomb efficiency drop. The results of this chapter directly motivated the modeling work in the following chapters. In the later chapters, both models for dendrite growth and SEI evolution would be considered to reflect what was observed from the in-situ experiment. At the same time, this in-situ setup provides a perfect method to characterize the performance of a lithium metal battery design by observing the lithium surface morphology evolution in real time, which in the later chapter was used again for demonstrating the piezoelectric feedback mechanisms.

Chapter 3

Concurrent Model of Lithium Dendrite Growth and SEI Penetration

3.1 Introduction

Lithium metal is thermodynamically unstable in organic electrolyte solvents, so that an interphase would form between lithium metal and the electrolyte solution. This thin film on the surface of lithium metal anode, known as the solid electrolyte interphase (SEI), is widely believed to have a significant impact on the cycling performance of lithium metal batteries.[84] The formation and growth of SEI consumes active lithium material and electrolyte solvent, resulting in permanent capacity loss, though a SEI layer also passivates the lithium surface and slows down the side reaction. If the electrolyte is not designed carefully, a SEI layer might grow so thick that eventually leads to high-impedance failure of the battery.[85] Moreover, the SEI layer is usually not strong enough to accommodate the morphological evolution of lithium surface and can be penetrated by lithium dendrites. Then SEI will regrow on the exposed lithium surface and consume more active materials.[86] Due to this inherent coupling between SEI growth and dendrite formation, the distribution and property of SEI have significant impacts on the morphology of lithium metal anode.

Current works on lithium dendrite growth have neglected the evolving SEI layer on top of it, though the two are inherently coupled. In this chapter, we present a model that enables simulations of concurrent lithium dendrite growth, SEI formation and growth, dendrite

penetration through the SEI layer, and SEI regrowth on the exposed surface. Our model includes the electrochemical process of dendrite growth, the process of SEI growth on a moving dendrite surface, and coupling of the two processes by considering SEI stretching associated with the dendrite growth beneath it and the effect of SEI resistance on reaction current for dendrite growth. With this model we have evaluated the effect of various parameters, such as applied current, SEI resistivity, and initial SEI distribution on dendrite formation. The results have provided important insights on how to reduce dendrite formation, which can guide the design of lithium metal batteries.

3.2 Model Development

Figure 3.1 shows a parallel electrode cell. The negative electrode at the bottom is a lithium metal (we will refer it as 'substrate') with a moving boundary governed by the lithium deposition rate. The substrate surface is described by the curve $z = z(x,t)$, where x, z are coordinates and *t* is time. For a two dimensional surface the form is given by $z = z(x, y, t)$, where y is another coordinate. A SEI layer on the substrate surface separates it from the electrolyte. The electrolyte is assumed to be EC (ethylene carbonate)-based with $LiPF_6$ as salt. The counter electrode only serves as the source of lithium ions during the charging process.

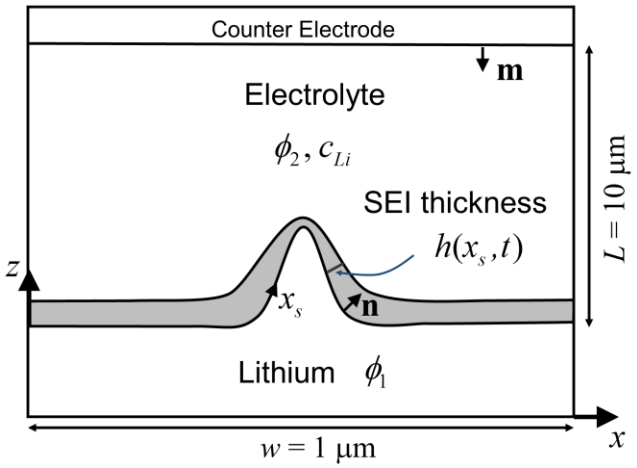

Figure 3.1 Two dimensional geometry of lithium metal battery considered in this model.

We first introduce the concept of SEI coverage density, $h(x_s, y_s)$, which is a spatial dependent variable on the metal substrate surface and is defined as the volume of SEI on a unit area of the substrate surface. Here x_s, y_s are the surface coordinates (Figure 3.1 shows x_s). $h(x_s, y_s)$ can be understood as the SEI thickness at location x_s, y_s, but the definition of SEI coverage density is more general. For instance, the definition is applicable even for a submonolayer of SEI molecules, where the usual concept of thickness becomes unclear. The definition is applicable no matter what is the SEI material, whether it is elastic, ductile or brittle. While here we define the coverage density based on volume, it can also be defined by mass or moles per unit area. The essence is that we can relate SEI proprieties, such as resistance, to the coverage density. Local SEI growth will increase the SEI coverage density, while stretching of the substrate surface will decrease it since the volume will be distributed on a larger surface area. Here the stretching of substrate surface comes purely from the geometric effect associated with the substrate morphology. The physical meaning of the SEI coverage density decrease due to stretching can be understood as the decrease of local SEI resistance due to porosity increase and crack formation

in the SEI layer. Imagine a scenario where the SEI layer, with a porous structure, was stretched to a larger surface area with its thickness unchanged. Then the porosity of the SEI must have increased significantly to accommodate the total volume change caused the surface area increase. It means either more pores have been generated inside the SEI layer, or there have been crack formations in some regions along the SEI surface, both of which will decrease the SEI resistance. The definition of SEI coverage density allows us to mathematically account for this SEI resistance drop in a more elegant way. On the other hand, the change of SEI thickness will also reflect directly in SEI resistance. Thus, in this chapter use the terms of SEI coverage density and SEI thickness interchangeably. We will simply refer SEI coverage density by SEI thickness since it is easier to understand.

Next we consider the mass conservation. To explain the idea, we look at a two dimensional problem so that the substrate surface is a one dimensional curve. The SEI layer on the substrate surface is described by its thickness $h(x_s)$ or $h(x)$. Consider a small SEI line element and denote its length at time *t* by l. After a time interval dt, the length of the element becomes $l + dl$, while its thickness becomes $h + dh$. Denote the SEI growth rate from electrochemical reaction by q_{SEI}, which is defined as the increase of SEI thickness per unit time due to reaction. The mass conservation gives

$$(l + dl)(h + dh) - lh = q_{SEI} l dt \ . \tag{3.1}$$

We define the strain rate of the substrate surface by $\dot{\varepsilon} = d\varepsilon / dt = dl / (l dt)$. With $dl = l\dot{\varepsilon} dt$, We can rewrite Eq. (3.1) into a growth equation

$$\frac{\partial h}{\partial t} = q_{SEI} - \dot{\varepsilon} h \ . \tag{3.2}$$

This equation shows that the overall SEI growth rate is the growth rate from electrochemical reaction minus the rate of coverage density reduction due to stretching of the substrate surface area.

The strain rate $\dot{\varepsilon}$ results from the geometric effect of evolution of the substrate surface morphology. It is related to the normal velocity of the substrate surface, v_n, and the surface curvature, κ, by $\dot{\varepsilon} = v_n \kappa$. Here convex surfaces are defined to have positive curvature. Then Eq. (3.2) becomes

$$\frac{\partial h}{\partial t} = q_{SEI} - v_n \kappa h \,. \tag{3.3}$$

It can be shown that Eq. (3.3) is also applicable to a two dimensional surface, where κ is the sum of the principal curvatures, or $\kappa = 2\kappa_m$ with κ_m being the mean curvature. For a one dimensional surface, the curvature is given by

$$\kappa = \frac{-\dfrac{\partial^2 z}{\partial x^2}}{\left(1 + \left(\dfrac{\partial z}{\partial x}\right)^2\right)^{3/2}}. \tag{3.4}$$

With EC as the electrolyte solvent, the component of SEI is considered to be made of $(CH_2OCO_2Li)_2$, and the SEI formation reaction occurs at the interface between lithium and electrolyte.[87] The growth rate of SEI from electrochemical reaction is governed by

$$q_{SEI} = -\frac{\Omega_{SEI}}{2F} i_{SEI} \,, \tag{3.5}$$

where Ω_{SEI} is the molecular volume of SEI, F is Faraday constant, and the SEI formation current density i_{SEI} is determined by the following Tafel-type kinetics[88]

$$i_{SEI} = -e^{-\lambda h} F k_{SEI} c_{EC} \exp\left(\frac{-\alpha_{SEI} F(\phi_1 - \phi_2 - R_{SEI} i_t)}{RT}\right). \tag{3.6}$$

Here λ is a scale factor of SEI formation current with respect to the SEI thickness, k_{SEI} is the SEI reaction rate coefficient, c_{EC} is solvent concentration, α_{SEI} is the charge transfer coefficient of SEI formation reaction, ϕ_1 is the lithium substrate potential, ϕ_2 is the electrolyte potential, i_t is the total lithium current density whose expression will be given later, *R* is gas constant, and *T* is temperature. The SEI resistance, R_{SEI}, is assumed proportional to the SEI thickness by

$$R_{SEI} = r_{res} h, \tag{3.7}$$

where r_{res} is the resistivity of SEI.

The growth of SEI is obtained by solving Eqs. (3.3 - 3.7). Note that the growth of SEI is coupled with dendrite growth by the lithium surface morphology $z(x,t)$, curvature κ, normal velocity of the substrate surface v_n, SEI resistance R_{SEI}, total lithium current i_t, and the electrolyte potential which depends on the surface morphology of the substrate.

To model dendrite formation and growth, we need to solve the concentration and potential fields in the electrolyte domain, and calculate the normal velocity of the lithium interface. The mass conservation is governed by the Nernst-Plank equation and electroneutrality, namely

$$\frac{\partial c_i}{\partial t} = -\nabla \cdot \mathbf{N}_i, \tag{3.8}$$

$$\mathbf{N}_i = -D_i \nabla c_i - \frac{z_i F D_i c_i}{RT} \nabla \phi_2, \tag{3.9}$$

$$\sum_i z_i c_i = 0, \tag{3.10}$$

where subscript i represents the species, which can be 'Li' (lithium ion) or '-' (salt anion PF_6^-). For each species, c_i is the concentration, $\mathbf{N}_i$ is the flux of species, D_i is the diffusion coefficient, and z_i is the charge number. The electroneutrality gives $c_- = c_{Li}$.

The current density, $\mathbf{i} = F\sum_i z_i \mathbf{N}_i$, is governed by

$$\nabla \cdot \mathbf{i} = 0 . \tag{3.11}$$

The boundary conditions on the lithium substrate surface are

$$\mathbf{N}_{Li} \cdot \mathbf{n} = \frac{i_t}{F}, \tag{3.12}$$

$$\mathbf{N}_- \cdot \mathbf{n} = 0, \tag{3.13}$$

where **n** is the normal direction of the substrate surface. We set $\phi_1 = 0$.

The total lithium current density is given by

$$i_t = i_{Li} + i_{SEI}, \tag{3.14}$$

where the reaction current density, i_{Li}, is described by the Butler–Volmer equation,

$$i_{Li} = i_0\left(\exp\left(\frac{(1-\alpha)F\eta}{RT}\right) - \exp\left(-\frac{\alpha F\eta}{RT}\right)\right). \tag{3.15}$$

Here i_0 is the exchange current density given by $i_0 = FK(c_{Li})^{1-\alpha}$, where K is the lithium deposition rate coefficient and α is the charge transfer coefficient for lithium deposition. A negative i_{Li} corresponds to lithium deposition. The over-potential, η, is given by

$$\eta = \phi_1 - \phi_2 - R_{SEI} i_t - U_{eq}, \tag{3.16}$$

where U_{eq} is the equilibrium over-potential. Note that with consideration of stress on the substrate surface, the over-potential used in Eq. (3.15) can be replaced by a generalized form

$\eta_{total} = \eta - \Omega_{Li}\sigma / F$, where Ω_{Li} is the molecular volume of lithium atom and σ is the hydrostatic stress. Using the typical parameters in Table I, i_0 is about 18.6 A/m^2. With even a low current density of $|i_{Li}|$ = 10 A/m^2, we will have $|\eta_{total}|$ =13.4 mV according to Eq. (3.15). A higher current leads to a larger $|\eta_{total}|$. The pressure on lithium surface exerted by surface tension is $\gamma\kappa$, and the corresponding hydrostatic stress has similar or smaller magnitude. A large surface energy density can potentially suppress the dendrite growth. However, the effect of surface tension is highly dependent on the electrolyte choice and electrode surface engineering, which is not the focus of this chapter. Therefore in this work we neglect the effect of surface energy to avoid unnecessary complexity.

The boundary conditions at the counter electrode are

$$\mathbf{N}_{Li} \cdot \mathbf{m} = \frac{I}{F}, \tag{3.17}$$

$$\mathbf{N}_{-} \cdot \mathbf{m} = 0, \tag{3.18}$$

where $\mathbf{m}$ is the normal direction of the counter electrode surface and I is the current density applied to the counter electrode.

The normal velocity of the substrate surface is given by

$$v_n = -\frac{\Omega_{Li}}{F} i_{Li}. \tag{3.19}$$

The cell was charged under the galvanostatic condition with a constant current density I applied to the counter electrode. COMSOL Multiphysics was used to implement the model into finite element to simulate the evolution using the moving mesh module. Below is a brief description of the implementation. The concentration and potential profiles are simulated by the tertiary current distribution module which solves mass conservation and current density

conservation based on the Nernst-Planck equation and the Poisson equation. On the lithium metal surface, the lithium deposition current is determined by the Butler-Volmer equation, which is further used to calculate the normal velocity of the surface. The surface morphology is updated by the moving mesh module based on the normal velocity, with re-meshing invoked when necessary. The SEI formation current density, which is determined by the Tafel-type kinetics, is passed to the boundary ODE module to simulate the evolution of SEI thickness. We update the boundary of the counter electrode based on the moving mesh module with a velocity of $v_m = -\Omega_{Li} I / F$ in the normal $\mathbf{m}$ direction. Table 1 lists the values of parameters used in simulations based on literature values.[15], [34], [88]

Table 1 Simulation parameters

Parameter	Value	Unit	Source
Faraday constant F	96485.3	$\mathrm{C/mol}$	
Gas constant R	8.31	$\mathrm{J/(mol \cdot K)}$	
Temperature T	293.15	K	
Initial electrolyte concentration $c_{Li,0}$	1000	$\mathrm{mol/m^3}$	
Li ion diffusion coefficient D_{Li}	7.5×10^{-11}	$\mathrm{m^2/s}$	[88]
Salt anion PF_6^- diffusion coefficient D_-	1.3×10^{-10}	$\mathrm{m^2/s}$	[88][a]
Lithium deposition rate coefficient K	6.1×10^{-6}	$\mathrm{mol^{0.5}/(m^{0.5} \cdot s)}$	[34]
Charge transfer coefficient α	0.5		[34]
Li atom molar volume Ω_{Li}	1.2998×10^{-5}	$\mathrm{m^3/mol}$	[34]
SEI molecule molar volume Ω_{SEI}	9.586×10^{-5}	$\mathrm{m^3/mol}$	[88][b]
Charge transfer coefficient α_{SEI}	0.5		[88]
Solvent EC concentration c_{EC}	4541	$\mathrm{mol/m^3}$	[88]
SEI reaction scale factor λ	1.2×10^7	$\mathrm{1/m}$	[88]
SEI reaction rate coefficient k_{SEI}	6×10^{-10}	$\mathrm{m/s}$	[88]
SEI resistivity r_{res}	2×10^5	$\Omega \cdot \mathrm{m}$	[15]

3.3 Results

In the simulation we set the distance between the two electrodes to be 10 μm and the width of the simulation domain to be 1 μm. We start with a case where a protrusion having a Gaussian height profile exists at the lithium metal surface. The height of the protrusion is 200 nm. The initial SEI thickness is uniform with a value of 10 nm. The simulation is run with a low current density of $I = 10$ A/m^2.

Figure 3.2(a) shows snapshots of the lithium surface morphology and SEI coverage density as a function of evolution time. The results show that dendrite growth has two distinct stages. In the first 10 seconds, the SEI around the dendrite tip is stretched thinner, while the shape of dendrite does not change much. In the next 40 seconds, the dendrite grows longer, driven by the higher lithium deposition rate at the tip area.

Notice that the curvature at the bottom area of a dendrite where it curves to the flat surface is negative or concave. The SEI coverage density or thickness in this area will increase due to negative stretching or compression, in addition to the growth from electrochemical reaction. The larger SEI thickness at the bottom corners of the dendrite causes lithium to grow slower than the flat area, so that the bottom of dendrite appears to slightly pinch into the substrate surface with a V-shape, as shown in Figure 3.2(b). This makes it easier for the dendrite to break away from the substrate.

To highlight the importance of integrating SEI in modeling dendrite growth, we run a simulation with the same parameters but without SEI, as shown in Figure 3.2(c). Comparing it with Figure 3.2(a), we can clearly see the difference in morphology and height, which are rounder and shorter without any V-shape at the bottom corner. We can observe that when there is no SEI, this protrusion will not grow into dendrite.

The two dendrite growth stages are further confirmed by the height and growth rate profile in Figure 3.3. Figure 3.3(b) shows that the dendrite growth rate accelerates quickly at the beginning. After about 10 s, the acceleration slows down considerably, which is reflected by the sharp change of slope at about 10 s. This transition can be explained by comparing the SEI thickness in the flat area and in the tip area, as shown in Figure 3.3(c). In the first stage of growth, the SEI thickness in the tip area decreases quickly. When the SEI thickness around the dendrite tip is low enough, the growth of SEI balances the decrease of SEI caused by stretching. Then the SEI thickness reaches local equilibrium, as shown by the horizontal line after 10 s. This is the second stage of growth. In contrast, the SEI thickness in the flat area keeps increasing. According to Eq. (3.3), both surface normal velocity and surface curvature affect SEI growth.

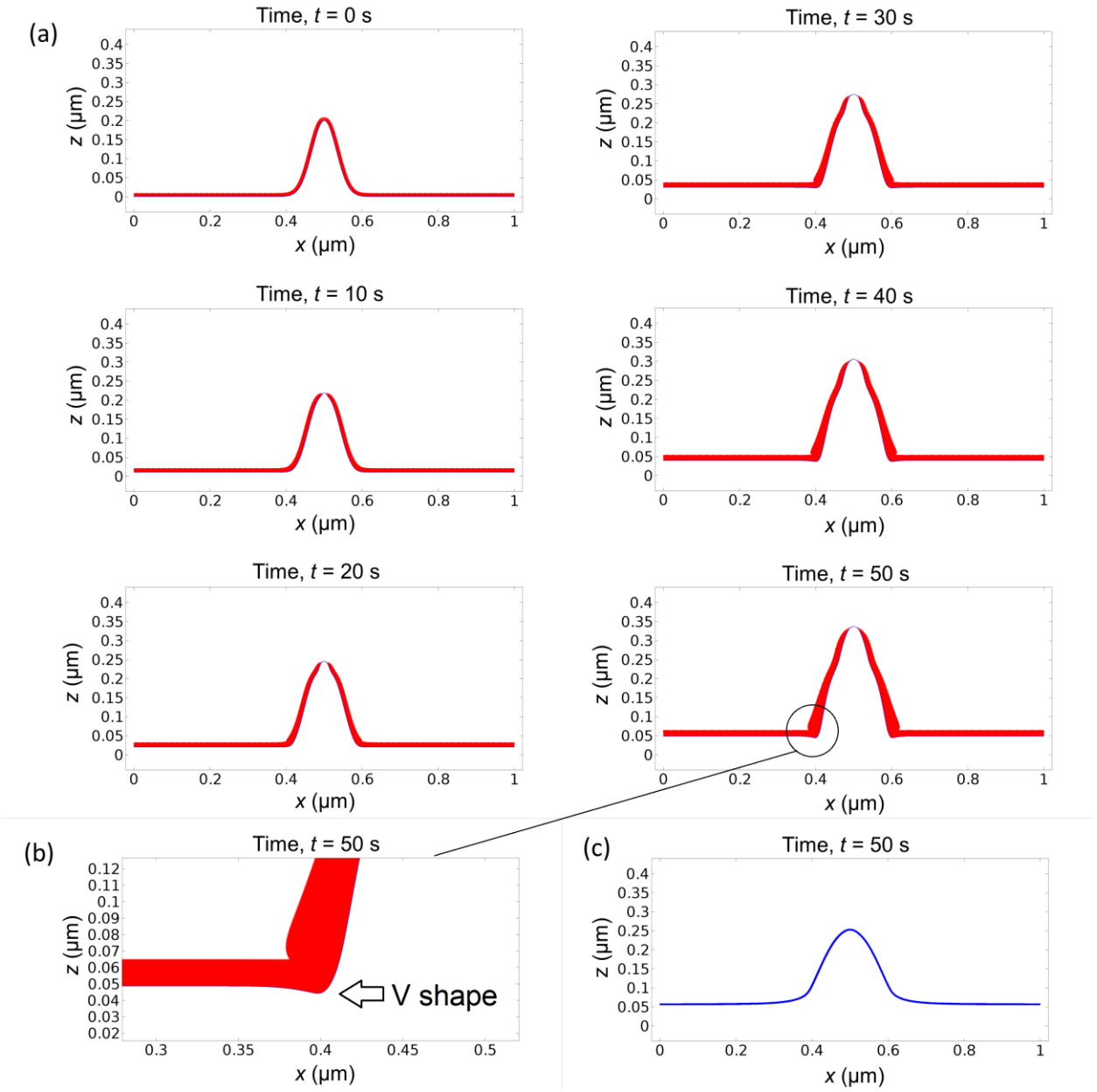

Figure 3.2 (a) Concurrent evolution of lithium surface morphology (blue line) and SEI layer thickness (red layer) starting with an initial surface protrusion and uniform initial SEI thickness. The applied current density is 10 A/m^2. (b) Zoom-in of the left bottom corner of the dendrite at t = 50 s. The dendrite appears to slightly pinch into the substrate surface with a V-shape due to the thick SEI and therefore slow growth at the corner. (c) Morphology at t=50 s without integrating SEI in the simulation. The shape is rounder and shorter without any V-shape at the bottom corner.

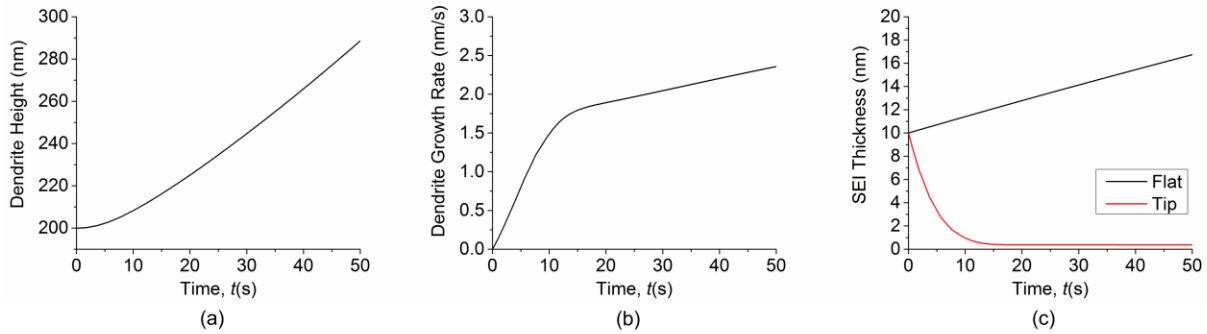

Figure 3.3 Dendrite height (a), growth rate (b) and SEI coverage density in the flat region vs. dendrite tip area (c) as a function of time, starting with lithium surface with an existing protrusion and uniform SEI coverage.

As shown in Figure 3.4, the initial normal velocity of the lithium surface is almost uniform. So the large curvature at the dendrite tip area is the main reason that causes the SEI thickness to decrease very quickly at the beginning. As the difference in SEI thickness between the tip area and the flat area becomes larger, the difference in surface normal velocity between the two areas also becomes larger. These two effects together lead to the large acceleration of dendrite growth rate in the first stage. After the SEI thickness at the tip reaches equilibrium, the dendrite growth rate can still increase slowly because the SEI keeps growing in other areas. This results in increasing difference in SEI resistance and lithium surface velocity between the tip area and the flat area, causing the tip area to appear accelerating due to slowing down of growth in the flat area.

Integrating the SEI thickness over the lithium surface, we can obtain the total amount of SEI formed during the simulation period. Figure 3.5 shows the comparison of normalized total SEI between the case with an initial surface protrusion and the case of a perfectly flat surface. The normalized total SEI is given by the ratio of the SEI volume at time t to the initial SEI volume. We find that SEI penetration and reformation lead to about 40% more electrolyte

consumption. Hence dendrite growth coupled with SEI penetration and formation causes reduced Coulombic efficiency.

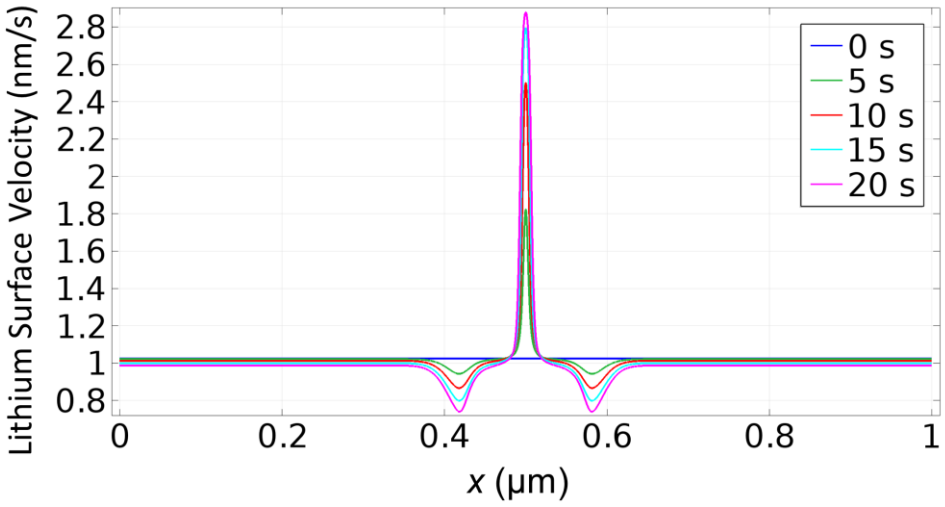

Figure 3.4 Lithium interface velocity distribution evolution in the first 20 seconds of simulation.

Overall, our simulations show that even with low applied current density, a protrusion can grow into dendrite by penetration of the SEI layer and by the resulting difference in SEI resistance between the tip and flat areas. This explains the experimental observations of dendrite formation and growth even under low current density.[37], [38]

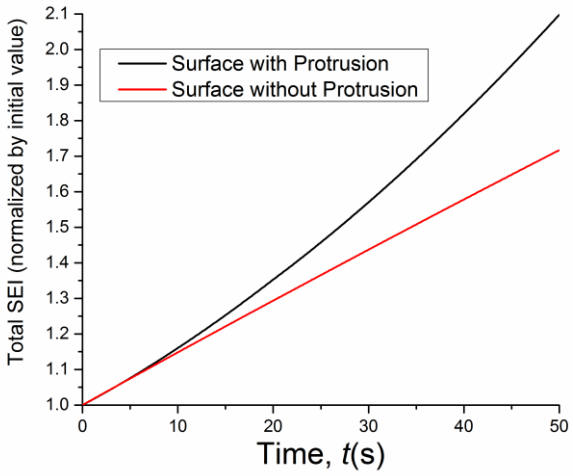

Figure 3.5 Total amount of SEI formed at the lithium interface with an existing protrusion in comparison with the case of a perfectly flat surface. The value is normalized to the initial SEI amount.

We have applied our coupled model to investigate the impact of several parameters on dendrite growth. We start by investigating the effect of applied current density. Under low current density, the magnitude of applied current has little effect on dendrite shape, as shown in Figure 3.6. Instead, increasing the applied current mainly scales up the dendrite growth rate, as shown in Figure 3.7. We can observe that increasing current density causes the SEI to grow faster in the flat area, while at the same time causes the SEI thickness at the tip area to decrease faster. The equilibrium SEI coverage density or thickness at the tip is smaller with larger applied current density.

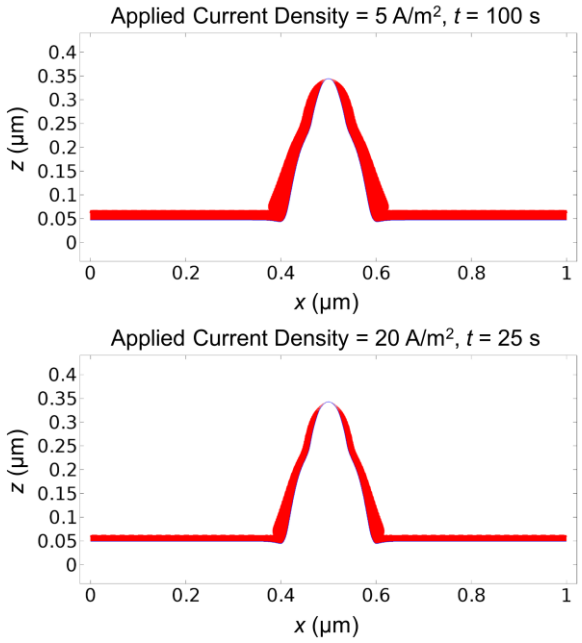

Figure 3.6 Lithium interface (blue line) and SEI coverage density distribution (red layer) under low current densities: 5 A/m^2 at t=100s (upper plot) and 20 A/m^2 at t=25s (lower plot).

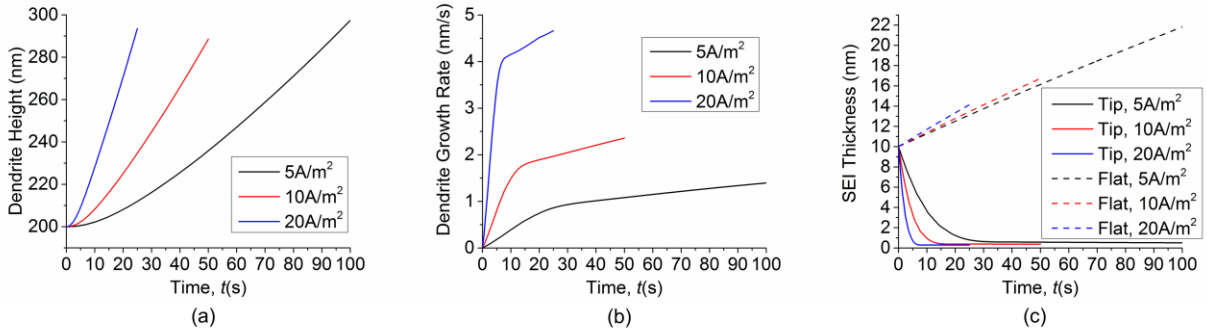

Figure 3.7 Under different current density in low current range, the comparison of dendrite height (a), dendrite growth rate (b), and SEI coverage density in the flat region vs. dendrite tip area (c) as a function of time.

However, if we apply high current density, the protrusion will grow very quickly into a sharp needle shape, as shown in Figure 3.8. Comparing the morphology at 0.1 s with current density of 1000 A/m^2 in Figure 3.8 and the morphology at 10 s with current density of 10 A/m^2

in Figure 3.2, we can observe the dramatic difference in dendrite shape, though the total amount of deposited lithium is the same. This is because with higher current density, the potential drop across the SEI layer due to its resistance is larger. In addition, the Butler-Volmer equation operates in the non-linear regime under high current density, so that even a small potential drop across the SEI layer can cause a significant effect. Therefore, SEI inhomogeneity plays a critical role. The small SEI resistance at the tip area promotes local dendrite growth strongly, leading to a sharp needle shape.

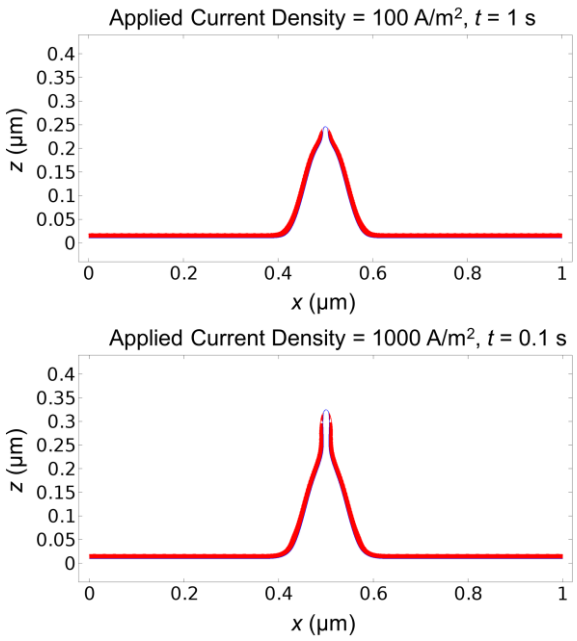

Figure 3.8 Lithium interface (blue line) and SEI coverage density distribution (red layer) under high current densities: 100 A/m^2 at t=1s (upper plot) and 1000 A/m^2 at t=0.1s (lower plot).

To summarize, the impact of current density depends on its magnitude. Under low current density, increasing current density will scale up the dendrite growth rate without changing the dendrite shape much. Under high current density, the effect of SEI resistance becomes critical. Increasing current density will not only speed up the dendrite growth, but also result in sharp needle-shaped dendrites, which are dangerous to battery safety.

Next we examine the effect of SEI resistivity. We only change the SEI resistivity, and keep other parameters and the applied current density of 10 A/m^2 the same. The SEI resistivity in Figure 3.2 or Table I is taken as the reference and noted as r_{res1}. The results in Figure 3.9 show that SEI resistivity has a significant impact on dendrite shape. The dendrite grows faster and sharper after we double the SEI resistivity ($r_{res} = 2r_{res1}$), as can be observed by comparing Figure 3.9 with Figure 3.2. After we reduce the SEI resistivity to $r_{res} = 0.1r_{res1}$, the dendrite becomes rounder and less dangerous. Dendrite growth rate also increases with the SEI resistivity, as shown in Figure 3.10. Increasing the SEI resistivity causes the SEI in the flat area to only grow slightly slower, but causes the SEI thickness at the dendrite tip area to decrease significantly faster.

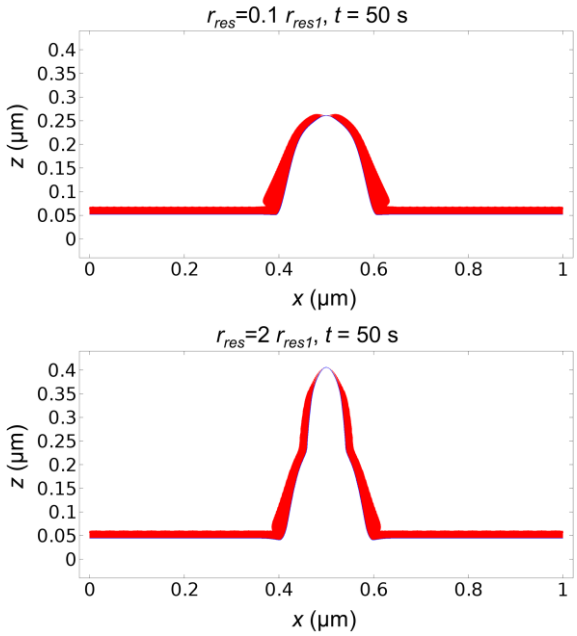

Figure 3.9 Lithium interface (blue line) and SEI coverage density distribution (red layer) with different SEI resistivities.

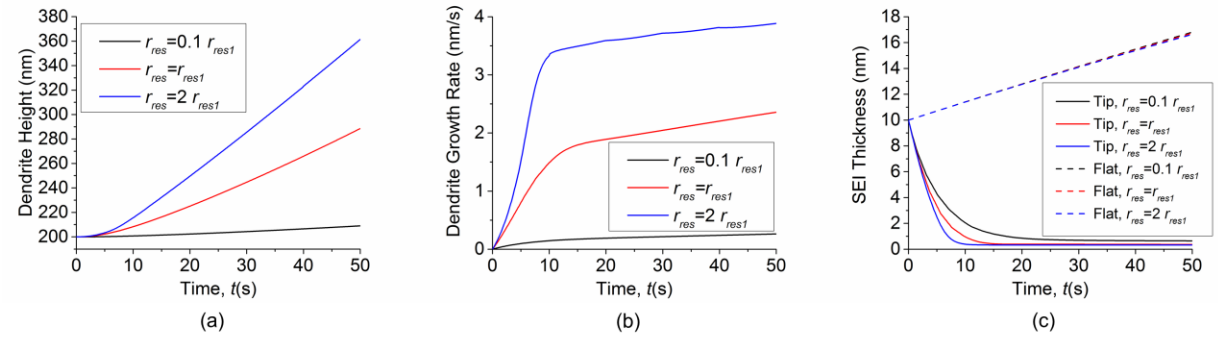

Figure 3.10 Effect of SEI resistivity on dendrite and SEI growth. (a) Dendrite height. (b) Dendrite growth rate. (c) SEI thickness in the flat area and in the dendrite tip area. Increasing the SEI resistivity causes the SEI in the flat area to grow only slightly slower, but causes the SEI thickness at the dendrite tip area to decrease significantly faster.

The predicted impact of SEI resistivity is consistent with experimental observations.[89] High SEI resistance will not only cause the dendrite grow faster, but also lead to sharper dendrites. Furthermore, an increase of the total resistance of the SEI layer can eventually cause impedance failure of the battery if not designed properly. Hence low SEI resistance is an important consideration in electrolyte design.

In addition to considering dendrite growth from existing protrusions on the lithium surface, we also performed simulations to investigate the impact of local SEI defects or inhomogeneity on dendrite formation. We run a simulation with an initially flat lithium surface and a local SEI defect in the center, i.e. an area without SEI coverage. The applied current density is still set at $10 A/m^2$ and all parameters are kept the same as previous simulations. Figure 3.11 shows the morphology evolution as a function of time. As the SEI coverage density is low in the defect area, the lithium deposition rate is locally high, resulting in the formation of a dendrite. Once again we can notice that the bottom of the dendrite appears pinching into the surface, as a result of the thick SEI at the corners due to the negative curvature.

Figure 3.12 gives the evolution of dendrite height, dendrite growth rate and SEI thickness. Figure 3.12(b) shows that the dendrite growth rate first decreases a little and then increases gradually. This is because the SEI thickness in the defect is initially zero, so the SEI is firstly repaired to the equilibrium value. The process consumes lithium flux and reduces the lithium deposition rate for a short period of time. Our simulation shows that local SEI defects or inhomogeneity can induce dendrite formation.

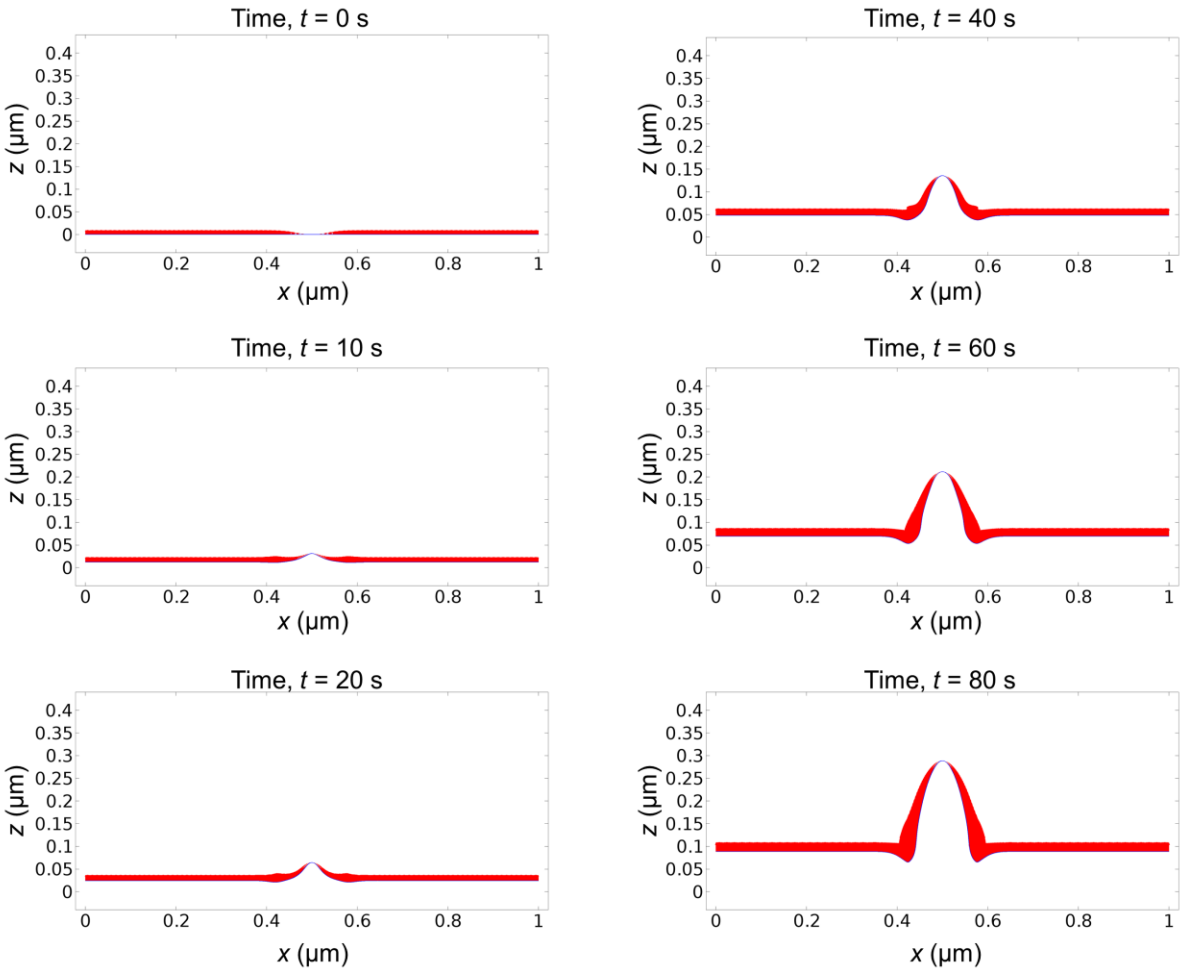

Figure 3.11 Concurrent evolution of lithium surface morphology (blue line) and SEI layer thickness (red layer) starting with a flat lithium surface and a local SEI defect in the center. The applied current density is 10 A/m^2.

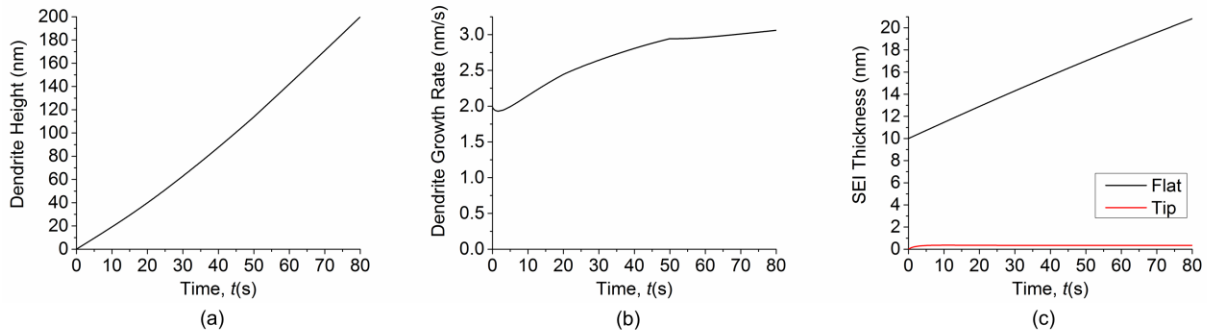

Figure 3.12 (a) Dendrite height as a function of time. (b) Dendrite growth rate as a function of time. (c) Comparison of SEI thickness in the flat area and in the dendrite tip area as a function of time. Simulation starts with a flat lithium surface and a local SEI defect in the center.

3.4 Conclusion

In this chapter we have developed a coupled dendrite and SEI growth model. Dendrite growth stretches the SEI and changes the curvature of the SEI layer, affecting the SEI evolution. SEI growth changes the resistance and reaction current, affecting the dendrite growth. The model has been used to investigate the impact of applied current density, SEI resistivity and SEI defects/inhomogeneity on dendrite formation and growth.

With a uniform initial SEI thickness, existing protrusions on the lithium surface can grow into dendrites. The growth shows two stages: quick acceleration during the SEI penetration process, and stable growth after reaching an equilibrium SEI thickness at the dendrite tip. The penetration and re-formation of SEI caused by dendrite growth consumes more electrolyte, and therefore reduces the Coulombic efficiency. Under low current density, increasing the current density will speed up the dendrite growth without changing the dendrite shape much. Under high current density, increasing the current will not only speed up the dendrite growth but also result in sharper needle-like dendrites. SEI resistivity significantly affects the shape and the growth rate

of dendrites. Dendrites will be rounder and less dangerous with low SEI resistivity. SEI defects/inhomogeneity can induce dendrite formation and growth even when the lithium surface is perfectly flat. Our results suggest that a flat initial lithium surface and a uniform SEI layer with low resistance are important to reduce dendrite formation and growth, and to avoid the decrease of Coulombic efficiency associated with SEI penetration and re-formation.

The model developed in this chapter provides a framework that can be further expanded to investigate a broad range of phenomena related to the interaction and concurrent growth of SEI and dendrite. More physics, such as mechanical deformation and growth of dendrites when their growth is confined by another solid such as a separator or a film, heat generation and its effect on dendrite growth, or interaction between multiple dendrites, can be incorporated to study various processes. These studies will lead to more fundamental understanding of dendrite growth and better design of lithium metal batteries.

Chapter 4

Linear Stability Analysis of Thin Film Blocking

4.1 Introduction

Extensive theoretical analyses have been done to understand the lithium dendrite formation and growth mechanisms since the first observation in 1980 [90]. Barton and Bockris proposed the first comprehensive model of dendrite growth in silver deposition process [29], arguing the enhanced spherical diffusion at the dendrite tip as the reason of dendrite growth with inadequate surface tension for preventing the amplification of surface roughness at the electrode, which was later applied by Monroe and Newman [91] to explain dendrite formation in lithium metal battery system. The model was extended further to include the elasticity, viscous drag, and mechanical pressure as additional influencing factors [32].

Experimental efforts to suppress dendrite formation and growth have been focusing on electrolyte modification. Organic electrolytes were seen as a promising solution to make lithium metal battery a practical design, as it can form a passive film called solid-electrolyte interphase (SEI), stabilizing the lithium electrodes over time [84]. Unfortunately, most researchers found that the SEI film, with its limited flexibility, could be easily cracked by the morphological changes of the lithium metal caused by the uniformity of the deposition/dissolution, thus failed to suppress the dendrite formation and caused more lithium loss due to the SEI re-formation at the broken points [17]. Further efforts have been made by changing the components of the

electrolyte in form of solvent [7], [92], [93], salt [52], [94], [95] and additives [96]–[98], in order to improve the stability and uniformity of the SEI film. Detailed summary on the related progress can be found in the review papers [45], [99].

Coating layer and solid electrolyte have also been used to mechanically block the growth of lithium dendrite. For example, a lithium conductive Li_3N film was prepared on Li metal surface as a protective layer, with suppressed dendrite growth reported when cycled in conventional organic electrolytes [100]. Some high molecular weight polymers, such as PEO, are found to be thermodynamically stable with Li even at a high temperature up to 100 ^oC, which leads to intensive experimental explorations for Solid PEO-based electrolytes in Li metal battery application [101]. The basic idea is to use the solid electrolyte to mechanically block lithium dendrite growth. Experimental study can be guided by theoretical analysis. Although Monroe and Newman [33]have developed a model bulk solid electrolyte, suggesting that the dendrite suppression can be achieved if the shear modulus of the blocking layer is about twice that of the Li anode (10^9 Pa), a thorough analysis specific for the thin film effect on the electrode stability has not been conducted yet.

In this chapter, we discuss the effect of coating film layer on lithium dendrite growth based on electrochemical modeling and linear perturbation analysis. The chapter is organized as follows. In Section 2, we derive the modified Butler-Volmer equation from a free energy point of view, showing that the stress effect on the reaction kinetics has two contributions: shift of the equilibrium and scale of the reaction current density. Section 3 presents the elastic solution to the stress problem associated with the system consisting of lithium substrate and coating layer during electrodeposition. In Section 4, a complete model of dendrite growth to account for both diffusion and stress effect is presented and analyzed with linear perturbation technique similar to

the method used in Sundstrom and Bark's paper [42]. Section 5 shows the suppression of lithium dendrite growth can be significant with the presence of coating layer, along with further discussion on how the results of the model can guide the experimental study in terms of coating material choice. Section 6 is conclusion. The list of symbols and their definitions used in this chapter are given in Section 7.

4.2 Effect of Deformation on Reaction Kinetics

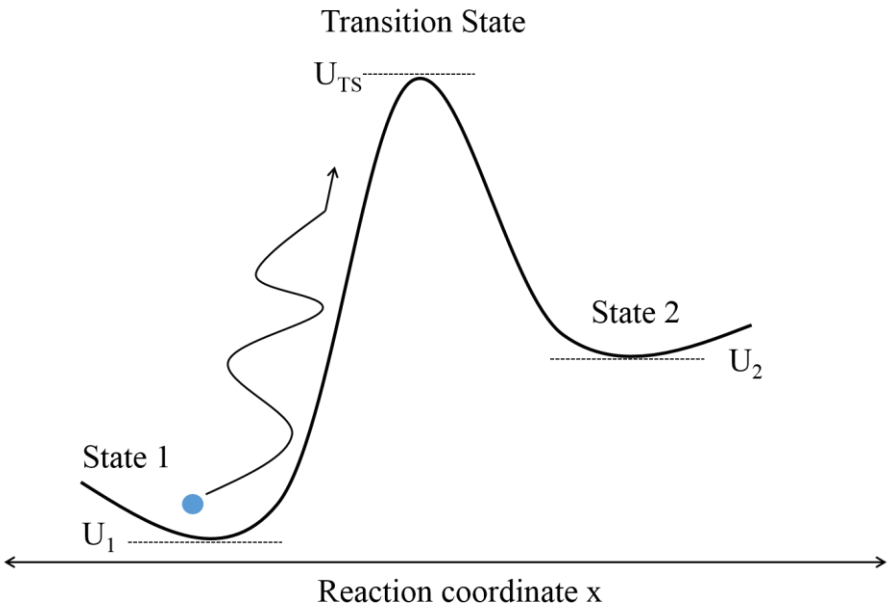

Figure 4.1 Potential energy route of a reacting molecule according to transition state theory.

In this section, the effect of deformation on reaction kinetics is discussed using an analogy to the derivation of the Butler-Volmer (BV) equation. Consider a reversible reaction $1 \leftrightarrow 2$, Figure 4.1 shows the potential energy route a molecule may go through during the reaction. Based on the transition state theory, the molecules need to overcome the energy barrier to escape from

state 1 to state 2. The mean escape rate per molecule is related to the statistic average frequency of these rare events as:

$$r_{1\to 2} = r_0 \exp(-\frac{U_{TS} - U_1}{RT}) \tag{4.1}$$

The net reaction rate then sums as:

$$r = r_{1\to 2} - r_{2\to 1} = r_0 \exp(-\frac{U_{TS} - U_1}{RT}) - r_0 \exp(-\frac{U_{TS} - U_2}{RT}) \tag{4.2}$$

For the Faradaic reaction in our case, $M^{z_R} \leftrightarrow M^{z_O} + ne^-$, the energy of state 1 is simply the chemical energy of the metal state, while the energy of the state 2 is the sum of the energy of the cations and electrons:

$$U_1 = \mu^0_{M^{z_R}} + RT \ln a_{M^{z_R}} + z_R F\phi \tag{4.3}$$

$$U_2 = \mu^0_{M^{z_O}} + RT \ln a_{M^{z_O}} + z_O F\phi - nF\phi_e \tag{4.4}$$

The only remaining unknown in the rate equation is the transition state energy, which we can get by assuming that the electrostatic energy of the transition state is a weighted average of the oxidized and reduced states:

$$U_{TS} = U^0_{TS} + \alpha z_R F\phi + (1-\alpha)(z_O F\phi - nF\phi_e) \tag{4.5}$$

Thus, the net reaction rate is:

$$\begin{aligned} r &= r_0 \exp[-\frac{U^0_{TS} + \alpha z_R F\phi + (1-\alpha)(z_O F\phi - nF\phi_e) - (\mu^0_{M^{z_R}} + RT \ln a_{M^{z_R}} + z_R F\phi)}{RT}] \\ &- r_0 \exp[-\frac{U^0_{TS} + \alpha z_R F\phi + (1-\alpha)(z_O F\phi - nF\phi_e) - (\mu^0_{M^{z_O}} + RT \ln a_{M^{z_O}} + z_O F\phi - nF\phi_e)}{RT}] \\ &= k_a a_{M^{z_R}} \exp[\frac{(1-\alpha)nF\Delta\phi}{RT}] - k_c a_{M^{z_O}} \exp[-\frac{\alpha nF\Delta\phi}{RT}] \end{aligned} \tag{4.6}$$

where $k_a = r_0 \exp(-\frac{U^0_{TS} - \mu^0_{M^{z_R}}}{RT})$, $k_c = r_0 \exp(-\frac{U^0_{TS} - \mu^0_{M^{z_O}}}{RT})$, and $\Delta\phi = \phi - \phi_e$.

In the experiments, the overpotential $\eta = \Delta\phi - \Delta\phi_{eq}$ is more often used as a measurement of the deviation of from the equilibrium potential $\Delta\phi_{eq} = \frac{RT}{nF}\ln(\frac{k_c a_{M^{z_O}}}{k_a a_{M^{z_R}}})$, which refers to the potential when the net reaction rate is zero. The current can be related to the overpotential as:

$$i = i_0\{\exp[\frac{(1-\alpha)nF\eta}{RT}] - \exp[-\frac{\alpha nF\eta}{RT}\}] \tag{4.7}$$

where $i_0 = nF(k_a a_{M^{z_R}})^{\alpha}(k_c a_{M^{z_O}})^{1-\alpha}$. The above equation is the form of Butler-Volmer equation that people commonly use.

Now let's focus on a reaction where the reactant is metal, $M \leftrightarrow M^{n+} + ne^-$. Consider the system is under deformation, and the mechanical impact on the energy of each species is denoted as $\Delta_m\mu_i$.

$$U_1 = \mu_M^0 + \Delta_m\mu_M \tag{4.8}$$

$$U_2 = \mu_{M^{n+}}^0 + RT\ln a_{M^{n+}} + nF\phi + \Delta_m\mu_{M^{n+}} - nF\phi_e + n\Delta_m\mu_{e^-} \tag{4.9}$$

Despite the detailed expression for $\Delta_m\mu_i$, we first look at the impact of these terms on the reaction kinetics. Here we make the assumption that the energy of the transition state is also a weighted average of the oxidized and reduced states:

$$U_{TS} = U_{TS}^0 + (1-\alpha)nF(\phi-\phi_e) + \alpha_m\Delta_m\mu_M + (1-\alpha_m)(\Delta_m\mu_{M^{n+}} + n\Delta_m\mu_{e^-}) \tag{4.10}$$

which will result in the net reaction rate to be:

$$\begin{aligned} r &= r_0\exp[-\frac{U_{TS}^0 + (1-\alpha)nF(\phi-\phi_e) + \alpha_m\Delta_m\mu_M + (1-\alpha_m)(\Delta_m\mu_{M^{n+}} + n\Delta_m\mu_{e^-}) - (\mu_M^0 + \Delta_m\mu_M)}{RT}] \\ &- r_0\exp[-\frac{U_{TS}^0 + (1-\alpha)nF(\phi-\phi_e) + \alpha_m\Delta_m\mu_M + (1-\alpha_m)(\Delta_m\mu_{M^{n+}} + n\Delta_m\mu_{e^-}) - (\mu_{M^{n+}}^0 + RT\ln a_{M^{n+}} + nF\phi + \Delta_m\mu_{M^{n+}} - nF\phi_e + n\Delta_m\mu_{e^-})}{RT}] \\ &= k_a\exp[\frac{(1-\alpha)nF\Delta\phi}{RT}]\exp[\frac{(1-\alpha_m)\Delta_m U}{RT}] - k_c a_{M^{n+}}\exp(-\frac{\alpha nF\Delta\phi}{RT})\exp(-\frac{\alpha_m\Delta_m U}{RT}) \end{aligned} \tag{4.11}$$

where $\Delta_m U = \Delta_m\mu_{M^{n+}} + n\Delta_m\mu_{e^-} - \Delta_m\mu_M$ is defined as the mechanical effect that influences the system equilibrium, thus the reaction rate is affected by the deformation only through this term.

However, the mechanical effect also affects the experimental measurements of overpotential $\eta = \Delta\phi - \Delta_m\phi_{eq}$, as the equilibrium potential would be shifted due to the deformation as $\Delta_m\phi_{eq} = \frac{RT}{nF}\ln(\frac{k_c a_{M^{n+}}}{k_a}) - \frac{\Delta_m U}{nF}$, which is the potential when the system is under the same stress state and the net reaction rate is zero. The relationship between the current density and the overpotential is:

$$i = i_0 \exp[\frac{(\alpha - \alpha_m)\Delta_m U}{RT}]\{\exp[\frac{(1-\alpha)nF\eta}{RT}] - \exp(-\frac{\alpha nF\eta}{RT})\} \tag{4.12}$$

where $i_0 = nF(k_a)^{\alpha}(k_c a_{M^{n+}})^{1-\alpha}$. The above equation takes the same form with many previous works. It indicates that the mechanical effect on the reaction kinetics has two contributions: shift of the equilibrium and scale of the reaction current density.

In most reported experiments [102], the stress only influences the anodic reaction rate, thus $\alpha_m = 0$ and using a common value $\alpha = 0.5$ would simplify the kinetics equation as:

$$i = i_0 \exp(\frac{\Delta_m U}{2RT})\sinh(\frac{nF\eta}{2RT}) \tag{4.13}$$

Now it remains to be determined how the mechanical effect should be expressed in $\Delta_m U$. As electrons have much smaller volume than the atoms and ions, it is difficult to define the mechanical effect on them. Thus in this chapter, we treat the term $\Delta_m\mu_{e^-}$ as zero. Otherwise, for a general species i under deformation, the molar free energy deviation from the undeformed state can be expressed as:

$$\Delta_m\mu_i = \Delta_m G_i / N_i \tag{4.14}$$

where $\Delta_m G$ is the Gibbs free energy change due to the mechanical effect, N_i is the molar number of the species.

The Gibbs free energy of elastic solid is:

$$G = U - TS + PV - V^0 \sigma_{ij}^d \varepsilon_{ij}^d \tag{4.15}$$

which has the differential form derived via Legendre transforms of the internal energy:

$$dG = SdT + \sum_i \mu_i dN_i + VdP - V^0 \varepsilon_{ij}^d d\sigma_{ij}^d = SdT + \sum_i \mu_i dN_i + V^0 dP - V^0 \varepsilon_{ij} d\sigma_{ij} \tag{4.16}$$

where σ_{ij}^d and ε_{ij}^d are the deviator stress and strain respectively, and the initial state is referred as state 0.

The change in Gibbs free energy due to mechanical effect at constant temperature condition thus can be calculated as:

$$\Delta_m \mu_i = (V^0 dP - V^0 \varepsilon_{ij} d\sigma_{ij}) / N_i = \bar{V}_i [P - P^0 - \varepsilon_{ij} (\sigma_{ij} - \sigma_{ij}^0)] \tag{4.17}$$

where $\bar{V}_i$ is the molar volume of the species.

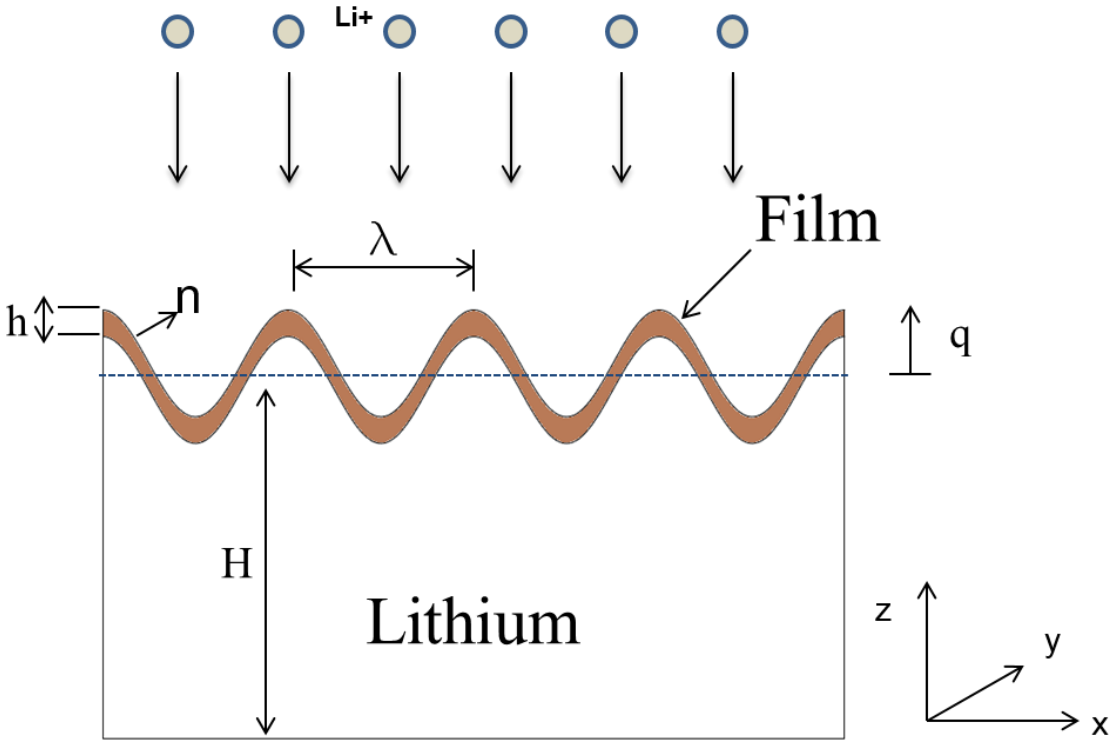

Figure 4.2 Schematics of the system we study in this paper.

The specific system that we are interested in this chapter is shown in Figure 4.2, and the related reaction $Li \leftrightarrow Li^+ + e^-$ happens at the substrate/film interface. For the lithium ions in the film, we assume the free energy of the film is shared by the ions. For the lithium atoms in the substrate, we assume the surface layer atoms take part in the reaction, with the free energy calculated at the interface position. Also, we assume there is no residual stress in the initial state of the system. Under these assumptions, the kinetic equation becomes:

$$i = 2i_0 \exp\left(\frac{-\bar{V}_{Li}(P_{Li} - \int \varepsilon_{ij}^s d\sigma_{ij}^s)}{2RT}\right)\sinh\left(\frac{F\eta}{2RT}\right) \tag{4.18}$$

where the superscripts s represent the values for the substrate.

4.3 Solution to the Stress Problem

In this section we will solve the stress of the system presented in Fig. 2. The problem can be interpreted as a wrinkled film bonded to a solid substrate, which has been solved by Huang et al. (2005). Here we follow the same routine, which starts with application of von Karman plate theory to the film. Let u_1 and u_2 be the in-plane displacement and q be the deflection, with ε_{ij}^0 as the initial strain when the film is flat. The membrane strain can be found as:

$$\varepsilon_{ij}^f = \varepsilon_{ij}^{f,0} + \frac{1}{2}\left(\frac{\partial u_i^f}{\partial x_j} + \frac{\partial u_j^f}{\partial x_i}\right) + \frac{1}{2}\frac{\partial q}{\partial x_i}\frac{\partial q}{\partial x_j} \tag{4.19}$$

The in-plane and out-plane equilibrium require:

$$\frac{\partial N_{ij}}{\partial x_j} = T_i \tag{4.20}$$

$$-\frac{E^f h^3}{12[1-(\nu^f)^2]}\frac{\partial^4 q}{\partial x_i \partial x_i \partial x_j \partial x_j} + \frac{\partial}{\partial x_j}\left(N_{ij}\frac{\partial q}{\partial x_i}\right) = T_3 \tag{4.21}$$

where T_1 and T_2 are the shear stresses on the interface and T_3 is the normal stress.

The membrane forces are calculated through the Hooke's law:

$$N_{ij} = \frac{E^f h}{1-(\nu^f)^2}[(1-\nu^f)\varepsilon_{ij}^f + \nu^f \varepsilon_{kk}^f \delta_{ij}] \tag{4.22}$$

Consider now the film is subjected to a sinusoidal deflection with $q = A\cos(\omega x)$. Based on Huang's results (2005), the shear stress on the interface would be neglectable, making simplification possible. The assumption of T_1 and T_2 being zero would result in uniformal membarane forces in the film, consequently requiring uniformal strains. Thus substitute the expression of the deflection into the strain equation would give us the in-plane displacement:

$$u_x^f = \frac{1}{8}\omega A^2 \sin(2\omega x) \text{ and } u_y^f = 0 \tag{4.23}$$

If we assume there is no initial strain, the strain field is:

$$\varepsilon_{xx}^f = \frac{1}{4}\omega^2 A^2, \varepsilon_{yy}^f = 0, \varepsilon_{xy}^f = 0 \tag{4.24}$$

where we assume the initial shear strain is zero.

The resulting stress field is:

$$N_{xx} = \frac{E^f h}{4[1-(\nu^f)^2]}\omega^2 A^2, N_{yy} = \frac{\nu^f E^f h}{4[1-(\nu^f)^2]}\omega^2 A^2, N_{xy} = 0 \tag{4.25}$$

The normal stress can be computed as:

$$\begin{aligned} T_3 &= -\frac{E^f h^3}{12[1-(\nu^f)^2]}\frac{\partial^4 q}{\partial x^4} + N_{xx}\frac{\partial^2 q}{\partial x^2} \\ &= -\frac{E^f h^3}{12[1-(\nu^f)^2]}\omega^4 A\cos(\omega x) - \frac{E^f h}{4[1-(\nu^f)^2]}\omega^4 A^3\cos(\omega x) \end{aligned} \tag{4.26}$$

As for the substrate of thickness H>>h, we treated as a semi-infinite body and assume its deformation is within the range of elasticity prediction. For simplification, we treat the problem as a two dimensional system and mark the interface as $z = 0$. The displacement formulation of governing equation for linear elasticity is:

$$\frac{\partial^2 u_i^s}{\partial x_j \partial x_j} + \frac{1}{1-2\nu}\frac{\partial^2 u_j^s}{\partial x_i \partial x_j} = 0 \tag{4.27}$$

The boundary conditions for the displacement are:

$$u_x^s(x, z \to -\infty) = 0 \tag{4.28}$$

$$u_z^s(x, z \to -\infty) = 0 \tag{4.29}$$

With the same assumption of zero shear stress as in the membarane force analysis, the traction boundary condition is:

$$\sigma_{xz}^s(x, z = 0) = 0 \tag{4.30}$$

$$\sigma_{zz}^s(x, z = 0) = T_3 \tag{4.31}$$

The problem can be solved with a separate variable approach. Considering the stress would decay as $z \to -\infty$, a general solution for the displacement equation takes the form of:

$$u^s = (C_1 + C_2 z)\sin(\omega x)\exp(\omega z) + (C_3 + C_4 z)\cos(\omega x)\exp(\omega z) \tag{4.32}$$

A quick glance at the displacement boundary condition would indicate that u_z only contains the $\cos(\omega x)$ terms, requiring the u_x containing only $\sin(\omega x)$ terms to balance the equation.

The enforcement of the boundary conditions and the governing equation would yield the following displacement field of the substrate:

$$u_x^s = \frac{T_3}{\cos(\omega x)}\left[\frac{(\nu^s - 1)(1 - 2\nu^s + \omega z)}{E^s \omega(1 - 2\nu^s)}\right]\sin(\omega x)\exp(\omega z) \tag{4.33}$$

$$u_z^s = \frac{T_3}{\cos(\omega x)}\left[\frac{(\nu^s - 1)(2 - 2\nu^s - \omega z)}{E^s \omega(1 - 2\nu^s)}\right]\cos(\omega x)\exp(\omega z) \tag{4.34}$$

The stress field of the substrate at the interface is:

$$\sigma_{xx}^s(x, z = 0) = T_3 \tag{4.35}$$

$$\sigma_{zz}^s(x, z = 0) = T_3 \tag{4.36}$$

The pressure term is calculated as:

$$P_{Li} = -\frac{\sigma_{xx}^s(x, z = 0) + \sigma_{zz}^s(x, z = 0)}{3} = -\frac{2}{3}T_3 \tag{4.37}$$

The term for free energy change in this case can be simplified as:s

$$\Delta_m U = -(P_{Li} - \varepsilon_{ij}^s \sigma_{ij}^s)\bar{V}_{Li} \tag{4.38}$$

4.4 Stability Analysis

The system can be described by the following conservation of mass and charge equations:

$$\frac{\partial c_i}{\partial t} = -\nabla N_i \tag{4.39}$$

$$\nabla \cdot i = 0 \tag{4.40}$$

$$i = F\sum_i z_i N_i \tag{4.41}$$

Note that the conservation of charge is automatically satisfied by the mass conservation equation. The flux of ion is governed by the Nernst-Plank equation based on dilute solution theory:

$$N_i = -\frac{FD_i z_i}{RT} c_i \nabla \phi - D_i \nabla c_i + c_i \vec{v} \tag{4.42}$$

In binary electrolyte systems, the mass conservation equations become:

$$z_1 \frac{\partial c_1}{\partial t} = \frac{Fz_1 D_1}{RT} \nabla \cdot (z_1 c_1 \nabla \phi) + D_1 z_1 \nabla^2 c_1 \tag{4.43}$$

$$z_2 \frac{\partial c_2}{\partial t} = \frac{Fz_2 D_2}{RT} \nabla \cdot (z_2 c_2 \nabla \phi) + D_2 z_2 \nabla^2 c_2 \tag{4.44}$$

Rearrange the two equations with the introduction of $C = z_1 c_1 = -z_2 c_2$ and the condition $\vec{u} = \vec{0}$, we can get:

$$\nabla \cdot (C \nabla (\frac{Fz_1 \phi}{RT})) + P \nabla^2 C = 0 \tag{4.45}$$

$$\frac{\partial C}{\partial t} = D \nabla^2 C \tag{4.46}$$

where two new parameters were introduced as $P = \frac{z_1(D_1 - D_2)}{D_1 z_1 - D_2 z_2}$ and $D = \frac{D_1 D_2 (z_1 - z_2)}{D_1 z_1 - D_2 z_2}$.

For the specific system in our concern, the electrolyte has a salt of form LiX. The fact that $c_1 = c_{Li^+}, c_2 = c_{X^-}, z_1 = 1, z_2 = -1$ further simplifies the governing equations as:

$$\nabla \cdot (C\nabla(\frac{F\phi}{RT})) + P\nabla^2 C = 0 \tag{4.47}$$

$$\frac{\partial C}{\partial t} = D\nabla^2 C \tag{4.48}$$

where $P = \frac{D_1 - D_2}{D_1 + D_2}$ and $D = \frac{2D_1 D_2}{D_1 + D_2}$.

Assuming the electrode surface profile is described by the function $z = f(x,t)$, the movement of the interface is governed by:

$$\frac{\partial f}{\partial t}\vec{e}_y \cdot \vec{n} = -\overline{V}_{Li}\vec{N}_1 \cdot \vec{n} \tag{4.49}$$

In dilute electrolyte, one can show that it can be simplified as:

$$\frac{\partial f}{\partial t}\vec{e}_y \cdot \vec{n} = \frac{\overline{V}_{Li}}{F} i \tag{4.50}$$

The boundary conditions at the electrode surface are:

$$\vec{N}_1 \cdot \vec{n} = \frac{i}{F} \tag{4.51}$$

$$\vec{N}_2 \cdot \vec{n} = 0 \tag{4.52}$$

which can be rearranged into:

$$\nabla C \cdot \vec{n} = -\frac{i}{2FD_1} \tag{4.53}$$

$$C\nabla(\frac{F\phi}{RT}) \cdot \vec{n} = \nabla C \cdot \vec{n} \tag{4.54}$$

The current density at the surface is described by the modified Butler-Volmer equation. For the system without coating film layer, the changed terms are caused by the surface tension:

$$i = Fk_a \exp[\frac{(1-\alpha)nF(\phi - V_0 + \gamma\overline{V}_{Li^+}\frac{\partial^2 f}{\partial x^2})}{RT}] - Fk_c C \exp(-\frac{\alpha nF(\phi - V_0 + \gamma\overline{V}_{Li^+}\frac{\partial^2 f}{\partial x^2})}{RT}) \quad (4.55)$$

For the system with coating film layer, the equation is:

$$i = Fk_a \exp[\frac{(1-\alpha)F(\phi - V_0) + \Delta_m U}{RT}] - Fk_c C \exp(-\frac{\alpha F(\phi - V_0)}{RT}) \quad (4.56)$$

Assume the perturbation amplitude of the electrode surface is much smaller than the perturbation wavelength, we can expand the profile functions as follows with $\varepsilon << 1$:

$$f(x,t) = f_0(t) + \varepsilon f_1(x,t) \quad (4.57)$$

$$i(x,t) = i_0 + \varepsilon i_1(x,t) + O(\varepsilon^2) \quad (4.58)$$

$$C(x,z,t) = C_0(z) + \varepsilon C_1(x,z,t) + O(\varepsilon^2) \quad (4.59)$$

$$\phi(x,z,t) = \phi_0(z) + \varepsilon\phi_1(x,z,t) + O(\varepsilon^2) \quad (4.60)$$

$$\Delta_m U(x,t) = \varepsilon U_1(x,t) \quad (4.61)$$

The terms used in boundary conditions can also be expanded as:

$$C(x,\varepsilon f_1,t) = C_0(0) + \frac{dC_0}{dz}|_0 \varepsilon f_1 + \varepsilon C_1(x,0,t) + O(\varepsilon^2) \quad (4.62)$$

$$\nabla C(x,\varepsilon f_1,t) = \varepsilon\frac{\partial C_1}{\partial x}|_0 \vec{e}_x + (\frac{dC_0}{dz}|_0 + \frac{d^2C_0}{dz^2}|_0 \varepsilon f_1 + \varepsilon\frac{\partial C_1}{\partial z}|_0)\vec{e}_y + O(\varepsilon^2) \quad (4.63)$$

$$\phi(x,\varepsilon f_1,t) = \phi_0(0) + \frac{d\phi_0}{dz}|_0 \varepsilon f_1 + \varepsilon\phi_1(x,0,t) + O(\varepsilon^2) \quad (4.64)$$

$$\nabla\phi(x,\varepsilon f_1,t) = \varepsilon\frac{\partial\phi_1}{\partial x}|_0 \vec{e}_x + (\frac{d\phi_0}{dz}|_0 + \frac{d^2\phi_0}{dz^2}|_0 \varepsilon f_1 + \varepsilon\frac{\partial\phi_1}{\partial z}|_0)\vec{e}_y + O(\varepsilon^2) \quad (4.65)$$

$$\vec{n} = (-\varepsilon\frac{\partial f_1}{\partial x},1) + O(\varepsilon^2) \quad (4.66)$$

Substitute the expansions into the governing equations:

$$\varepsilon \frac{\partial C_1}{\partial t} = \frac{d^2 C_0}{dz^2} + \varepsilon\left(\frac{\partial^2 C_1}{\partial x^2} + \frac{\partial^2 C_1}{\partial z^2}\right) \tag{4.67}$$

$$\varepsilon C_0 \frac{\partial^2 \phi_1}{\partial x^2} + \frac{\partial}{\partial z}\left[(C_0 + \varepsilon C_1)\frac{d\phi_0}{dz}\right] + \varepsilon \frac{\partial}{\partial z}\left(C_0 \frac{\partial \phi_1}{\partial z}\right) + P\frac{d^2 C_0}{dz^2} + P\varepsilon\left(\frac{\partial^2 C_1}{\partial x^2} + \frac{\partial^2 C_1}{\partial z^2}\right) = 0 \tag{4.68}$$

$$\frac{df_0}{dt} + \varepsilon \frac{\partial f_1}{\partial t} = \frac{\overline{V}_{Li}}{F}(i_0 + \varepsilon i_1) \tag{4.69}$$

The boundary conditions are also treated in a similar way:

$$\frac{dC_0}{dz}\Big|_0 + \frac{d^2 C_0}{dz^2}\Big|_0 \varepsilon f_1 + \varepsilon \frac{\partial C_1}{\partial z}\Big|_0 = -\frac{1}{2FD_1}(i_0 + \varepsilon i_1) \tag{4.70}$$

$$\begin{aligned}&\{C_0(0) + \frac{dC_0}{dz}\Big|_0 \varepsilon f_1 + \varepsilon C_1(x,0,t)\}\left(\frac{d\phi_0}{dz}\Big|_0 + \frac{d^2\phi_0}{dz^2}\Big|_0 \varepsilon f + \varepsilon \frac{\partial \phi_1}{\partial z}\Big|_0\right)\\ &= \frac{dC_0}{dz}\Big|_0 + \frac{d^2 C_0}{dz^2}\Big|_0 \varepsilon f_1 + \varepsilon \frac{\partial C_1}{\partial z}\Big|_0\end{aligned} \tag{4.71}$$

The current density at the electrode without film is expanded as:

$$\begin{aligned}i_0 + \varepsilon i_1 = {} & Fk_a \exp\{\frac{(1-\alpha)F[\phi_0(0) + \frac{d\phi_0}{dz}\Big|_0 \varepsilon f_1 + \varepsilon\phi_1(x,0,t) - V_0 + \gamma\overline{V}_{Li^+}\varepsilon\frac{\partial^2 f_1}{\partial x^2}]}{RT}\}\\ & - Fk_c[C_0(0) + \frac{dC_0}{dz}\Big|_0 \varepsilon f_1 + \varepsilon C_1(x,0,t)]\\ & \exp\{-\frac{\alpha F[\phi_0(0) + \frac{d\phi_0}{dz}\Big|_0 \varepsilon f_1 + \varepsilon\phi_1(x,0,t) - V_0 + \gamma\overline{V}_{Li^+}\varepsilon\frac{\partial^2 f_1}{\partial x^2}]}{RT}\}\end{aligned} \tag{4.72}$$

The current density at the electrode with film is expanded as:

$$\begin{aligned}i_0 + \varepsilon i_1 = {} & Fk_a \exp\{\frac{(1-\alpha)F[\phi_0(0) + \frac{d\phi_0}{dz}\Big|_0 \varepsilon f_1 + \varepsilon\phi_1(x,0,t) - V_0] + \varepsilon U_1}{RT}\}\\ & - Fk_c[C_0(0) + \frac{dC_0}{dz}\Big|_0 \varepsilon f_1 + \varepsilon C_1(x,0,t)]\\ & \exp\{-\frac{\alpha F[\phi_0(0) + \frac{d\phi_0}{dz}\Big|_0 \varepsilon f_1 + \varepsilon\phi_1(x,0,t) - V_0]}{RT}\}\end{aligned} \tag{4.73}$$

Identify the coefficients of ε^n, and we can get the zeroth order and first order problems respectively for $n = 0,1$.

Zeroth order problem:

$$0 = \frac{d^2 C_0}{dz^2} \tag{4.74}$$

$$\frac{d}{dz}(C_0 \frac{d\phi_0}{dz}) + P \frac{d^2 C_0}{dz^2} = 0 \tag{4.75}$$

$$\frac{df_0}{dt} = -\frac{\overline{V}_{Li}}{F} i_0 \tag{4.76}$$

Boundary conditions at $z = 0$ are:

$$\frac{dC_0}{dz}|_0 = -\frac{i_0}{2FD_1} \tag{4.77}$$

$$C_0(0) \frac{d\phi_0}{dz}|_0 = \frac{dC_0}{dz}|_0 \tag{4.78}$$

$$i_0 = Fk_a \exp\{\frac{(1-\alpha)F[\phi_0(0) - V_0]}{RT}\} - Fk_c C_0(0) \exp\{-\frac{\alpha F[\phi_0(0) - V_0]}{RT}\} \tag{4.79}$$

The solution can be easily found with the additional assumption that the bulk concentration is known beyond a boundary layer of thickness δ.

$$C = C_b, \text{at } z = \delta \tag{4.80}$$

$$C_0(z) = C_b - \frac{i_0}{2FD_1}(\delta - z) = C_b[1 - \frac{i_0}{i_L}(1 - \frac{z}{\delta})] \tag{4.81}$$

$$\phi_0(z) = \ln(C_0) + const = \ln\{C_b[1 - \frac{i_0}{i_L}(1 - \frac{z}{\delta})]\} + const \tag{4.82}$$

where the limiting current is introduced as a parameter:

$$i_L = 2FD_1 C_b / \delta \tag{4.83}$$

And the constant in the potential profile satisfies:

$$i_0 = Fk_a \exp\{\frac{(1-\alpha)F[\ln\ C_b(1-\frac{i_0}{i_L}) + const\ - V_0]}{RT}\} - Fk_c C_0(0)\exp\{-\frac{\alpha F[\ln\ C_b(1-\frac{i_0}{i_L}) + const\ - V_0]}{RT}\} \tag{4.84}$$

First order problem:

$$\frac{\partial C_1}{\partial t} = \frac{\partial^2 C_1}{\partial x^2} + \frac{\partial^2 C_1}{\partial z^2} \tag{4.85}$$

$$C_0\frac{\partial^2 \phi_1}{\partial x^2} + \frac{\partial}{\partial z}[C_1\frac{d\phi_0}{dz}] + \frac{\partial}{\partial z}(C_0\frac{\partial \phi_1}{\partial z}) + P(\frac{\partial^2 C_1}{\partial x^2} + \frac{\partial^2 C_1}{\partial z^2}) = 0 \tag{4.86}$$

$$\frac{\partial f_1}{\partial t} = \frac{\overline{V}_{Li}}{F} i_1 \tag{4.87}$$

Boundary conditions at $z = 0$ are:

$$\frac{d^2 C_0}{dz^2}|_0\ f_1 + \frac{\partial C_1}{\partial z}|_0 = -\frac{i_1}{2FD_1} \tag{4.88}$$

$$\{\frac{dC_0}{dz}|_0\ f_1 + C_1(x,0,t)\}\frac{d\phi_0}{dz}|_0 + C_0(0)(\frac{d^2\phi_0}{dz^2}|_0\ f + \frac{\partial \phi_1}{\partial z}|_0) = \frac{d^2 C_0}{dz^2}|_0\ f_1 + \frac{\partial C_1}{\partial z}|_0 \tag{4.89}$$

Current density at the surface without film:

$$\begin{aligned} i_1 = {} & Fk_a\{\frac{(1-\alpha)F[\frac{d\phi_0}{dz}|_0\ f_1 + \phi_1(x,0,t) + \gamma\overline{V}_{Li^+}\frac{\partial^2 f_1}{\partial x^2}]}{RT}\}\exp\{\frac{(1-\alpha)F[\phi_0(0) - V_0]}{RT}\} \\ & - Fk_c\{-\frac{\alpha F[\frac{d\phi_0}{dz}|_0\ f_1 + \phi_1(x,0,t) + \gamma\overline{V}_{Li^+}\frac{\partial^2 f_1}{\partial x^2}]}{RT}C_0(0) \\ & + \frac{dC_0}{dz}|_0\ f_1 + C_1(x,0,t)\}\exp\{-\frac{\alpha F[\phi_0(0) - V_0]}{RT}\} \end{aligned} \tag{4.90}$$

Current density at the surface with film:

$$i_1 = Fk_a\{\frac{(1-\alpha)F[\frac{d\phi_0}{dz}|_0 \ f_1 + \phi_1(x,0,t)] + U_1}{RT}\}\exp\{\frac{(1-\alpha)F[\phi_0(0) - V_0]}{RT}\}$$
$$- Fk_c\{-\frac{\alpha F[\frac{d\phi_0}{dz}|_0 \ f_1 + \phi_1(x,0,t)]}{RT}C_0(0) \tag{4.91}$$
$$+ \frac{dC_0}{dz}|_0 \ f_1 + C_1(x,0,t)\}\exp\{-\frac{\alpha F[\phi_0(0) - V_0]}{RT}\}$$

In order to complete the perturbation analysis, we need to further simplify the equations with the assumption that the system has reached steady state and the profile functions have the following mode:

$$f_1 = A\cos(\omega x) \tag{4.92}$$

$$i_1 = I\cos(\omega x) \tag{4.93}$$

$$C_1 = \theta(z)\cos(\omega x) \tag{4.94}$$

$$\phi_1 = \Phi(z)\cos(\omega x) \tag{4.95}$$

Energy term from Equation (38) also simplifies to the following expression as we only consider the first order term:

$$U_1 = -\frac{\overline{V}_{Li}E^f h^3}{18[1-(\nu^f)^2]}\omega^4\cos(\omega x) \tag{4.96}$$

Substitution of these expressions into the governing equations and boundary conditions results in the following problem:

$$0 = \theta'' - \omega^2\theta \tag{4.97}$$

$$C_0(0)\Phi'' + C_0'(0)\Phi' - \omega^2 C_0(0)\Phi + (\theta\phi_0')' = 0 \tag{4.98}$$

$$\frac{\partial A}{\partial t} = \frac{\overline{V}_{Li}}{F}I \tag{4.99}$$

with boundary conditions:

$$\theta'|_0 = -\frac{I}{2FD_1} \tag{4.100}$$

$$\theta\phi_0'|_0 + C_0\Phi'|_0 = \theta'|_0 \tag{4.101}$$

The case without film has the additional boundary condition as:

$$\begin{aligned} I = {} & Fk_a\{\frac{(1-\alpha)F[\phi_0'A + \Phi(0) - \gamma\overline{V}_{Li^+}\omega^2 A]}{RT}\}\exp\{\frac{(1-\alpha)F[\phi_0(0) - V_0]}{RT}\} \\ & - Fk_c\{-\frac{\alpha F[\phi_0'A + \Phi(0) - \gamma\overline{V}_{Li^+}\omega^2 A]}{RT}C_0(0) + C_0'(0)A + \theta(0)\}\exp\{-\frac{\alpha F[\phi_0(0) - V_0]}{RT}\} \end{aligned} \tag{4.102}$$

while the case with film has the additional boundary condition as:

$$\begin{aligned} I = {} & Fk_a\{\frac{(1-\alpha)F[\phi_0'A + \Phi(0)] + U_1}{RT}\}\exp\{\frac{(1-\alpha)F[\phi_0(0) - V_0]}{RT}\} \\ & - Fk_c\{-\frac{\alpha F[\phi_0'A + \Phi(0)]}{RT}C_0(0) + C_0'(0)A + \theta(0)\}\exp\{-\frac{\alpha F[\phi_0(0) - V_0]}{RT}\} \end{aligned} \tag{4.103}$$

One can show that the solutions to the problem have the forms of:

$$\theta = \hat{\theta}e^{-\omega z} \tag{4.104}$$

$$\Phi = \hat{\theta}\frac{\phi_0'' - \omega\phi_0'}{\omega C_0'}e^{-\omega z} + \hat{\Phi}\exp -[\frac{C_0'}{2C_0} + \sqrt{(\frac{C_0'}{2C_0})^2 + \omega^2}]z \tag{4.105}$$

Use the boundary conditions to determine the constants:

$$\hat{\theta} = \frac{I}{2FD_1\omega} \tag{4.106}$$

$$\hat{\Phi} = -\hat{\theta}\frac{\phi_0' + \omega - C_0\frac{\phi_0'' - \omega\phi_0'}{C_0'}}{\frac{C_0'}{2} + \sqrt{(\frac{C_0'}{2})^2 + \omega^2 C_0^2}} = -\frac{I}{2FD_1\omega}\cdot\frac{\phi_0' + \omega - C_0\frac{\phi_0'' - \omega\phi_0'}{C_0'}}{\frac{C_0'}{2} + \sqrt{(\frac{C_0'}{2})^2 + \omega^2 C_0^2}} \tag{4.107}$$

The last constant *I* can be eliminated with the remaining boundary condition. Here we first show the result for the case without film:

$$I = \beta A \tag{4.108}$$

$$\beta = \frac{e^{(1-\alpha)\varphi} F^2 k_a (1-\alpha)(\phi_0' - \gamma \overline{V}_{Li^+} \omega^2) + e^{-\alpha\varphi}[F^2 k_c \alpha C_0 (\phi_0' - \gamma \overline{V}_{Li^+} \omega^2) + FRTk_c C_0']}{RT - F^2 k_a (1-\alpha) e^{(1-\alpha)\varphi} B_2 - F^2 k_c \alpha C_0 e^{-\alpha\varphi} B_2 + FRTk_c e^{-\alpha\varphi} B_1} \tag{4.109}$$

where $B_1 = \theta(0)/I, B_2 = \Phi(0)/I, \phi = \frac{F(\varphi_0(0) - V_0)}{RT}$.

Thus the growth of the perturbation is governed by:

$$\frac{d \ln A}{dt} = \frac{\overline{V}_{Li}}{F} \beta \tag{4.110}$$

Note that $\beta > 0$ for all ω if $\gamma = 0$, which means the surface tension is the only term that is compressing the growth of the perturbation. Setting $\beta = 0$ would give us a critical wavenumber:

$$\omega_{crit,\gamma} = \frac{1}{\sqrt{\gamma \overline{V}_{Li^+}}} \sqrt{\phi_0' + \frac{RTk_c e^{-\alpha\varphi} C_0'}{F(1-\alpha) k_a e^{(1-\alpha)\varphi} + \alpha k_c e^{-\alpha\varphi} C_0}} \tag{4.111}$$

For the case with film, the result only differs at the growth factor β:

$$\beta = \frac{e^{(1-\alpha)\varphi} F^2 k_a (1-\alpha)(\phi_0' - \frac{E^f h^3 \overline{V}_{Li}}{18[1-(\nu^f)^2]} \omega^4) + e^{-\alpha\varphi}(F^2 k_c \alpha C_0 \phi_0' + FRTk_c C_0')}{RT - F^2 k_a (1-\alpha) e^{(1-\alpha)\varphi} B_2 - F^2 k_c \alpha C_0 e^{-\alpha\varphi} B_2 + FRTk_c e^{-\alpha\varphi} B_1} \tag{4.112}$$

Now the critical wavenumber is related to the material properties of the film:

$$\omega_{crit,f} = \left(\frac{18[1-(\nu^f)^2]}{E^f h^3 \overline{V}_{Li}} \right)^{1/4} \left(\phi_0' + \frac{e^{-\varphi}(Fk_c \alpha C_0 \phi_0' + RTk_c C_0')}{F(1-\alpha) k_a} \right)^{1/4} \tag{4.113}$$

A more convenient way to compute the critical wavenumber is using the applied current as a parameter, which leads to the following forms of the critical wavenumber equation:

$$\omega_{crit,\gamma} = \frac{1}{\sqrt{\gamma \overline{V}_{Li^+}}} \sqrt{\frac{\frac{i_0}{i_L}}{\delta(1 - \frac{i_0}{i_L})} + \frac{RTk_c e^{-\alpha\varphi} \frac{C_b i_0}{\delta i_L}}{F(1-\alpha) k_a e^{(1-\alpha)\varphi} + \alpha k_c e^{-\alpha\varphi} C_b (1 - \frac{i_0}{i_L})}} \tag{4.114}$$

$$\omega_{crit,f} = \left(\frac{18[1-(\nu^f)^2]}{E^f h^3 \overline{V}_{Li}}\right)^{1/4} \left(\frac{\frac{i_0}{i_L}}{\delta(1-\frac{i_0}{i_L})} + \frac{e^{-\varphi}(Fk_c\alpha + RTk_c)\frac{C_b i_0}{\delta i_L}}{F(1-\alpha)k_a}\right)^{1/4} \tag{4.115}$$

4.5 Results

The two critical wavenumber equations (4.114) and (4.115) indicate that for both cases, the surface become more unstable as the limiting current is approached. This is consistent with experimental observations. To see the quantitative difference between the two cases, we need to plug the parameter values into the model. Literature values of the material properties of a lithium/polymer film system used for this analysis are shown in Table 2 [88][33].

Table 2 Parameters employed to the dendrite growth model

$\overline{V}_{Li} = 1.3\times10^{-5}\ \mathrm{m}^3/\mathrm{mol}$	$\overline{V}_{Li^+} = 1.1718\times10^{-4}\ \mathrm{m}^3/\mathrm{mol}$	$D_1 = 4\times10^{-10}\ \mathrm{m}^2/\mathrm{s}$	$\gamma = 0.04\ \mathrm{J/m}$
$F = 96485\ \mathrm{C/mol}$	$R = 8.314\ \mathrm{J/mol\cdot K}$	$T = 298\ \mathrm{K}$	$V_0 = 0\ \mathrm{V}$
$i_0 = 75\ \mathrm{A/m}^2$	$C_b = 1\times10^3\ \mathrm{mol/m}^3$	$k_a = k_c = 2\times10^{-10}$	$\alpha = 0.5$
$E^f = 100\ \mathrm{GPa}$	$\nu^f = 0.25$	$h = 2\times10^{-6}\ \mathrm{m}$	$\delta = 1\times10^{-3}\ \mathrm{m}$

Substituting the parameter values into the critical wavenumber equation of the case without film yields the critical wavelength as $2\pi/\omega_{crit,\gamma} \approx 0.07mm$, which is in good consistency with the literature values. As a comparison, the same set of parameters would yield the critical wavelength for the case with film as $2\pi/\omega_{crit,f} \approx 0.41mm$. This shows that the addition of the film can increase the surface stability.

The improvement can be illustrated clearer by considering the relationship between the critical wavenumber and the applied current. Figure 4.3 shows that each critical wavenumber curve can separate the quadrant into two regions, in the left of which the growth rate is positive thus unstable, while in the right region the growth rate is negative thus stable. Clearly the addition of the film increased the area of the stable region by decreasing the critical wavenumber except for very small current scenarios. The reason why the critical wavenumber is larger in the case with film than without film in the small current region is that the critical wavenumber is correlated to the different powers of the applied current in both cases. In fact, the terms under the square root and the terms inside the power of 0.25 bracket are of the same order of magnitude (both smaller than 1), thus a square root is smaller than the power of 0.25 of a value smaller than 1. Note that we normally would not conduct experiment in this small current region, it should not be our concern in design when choosing the film properties.

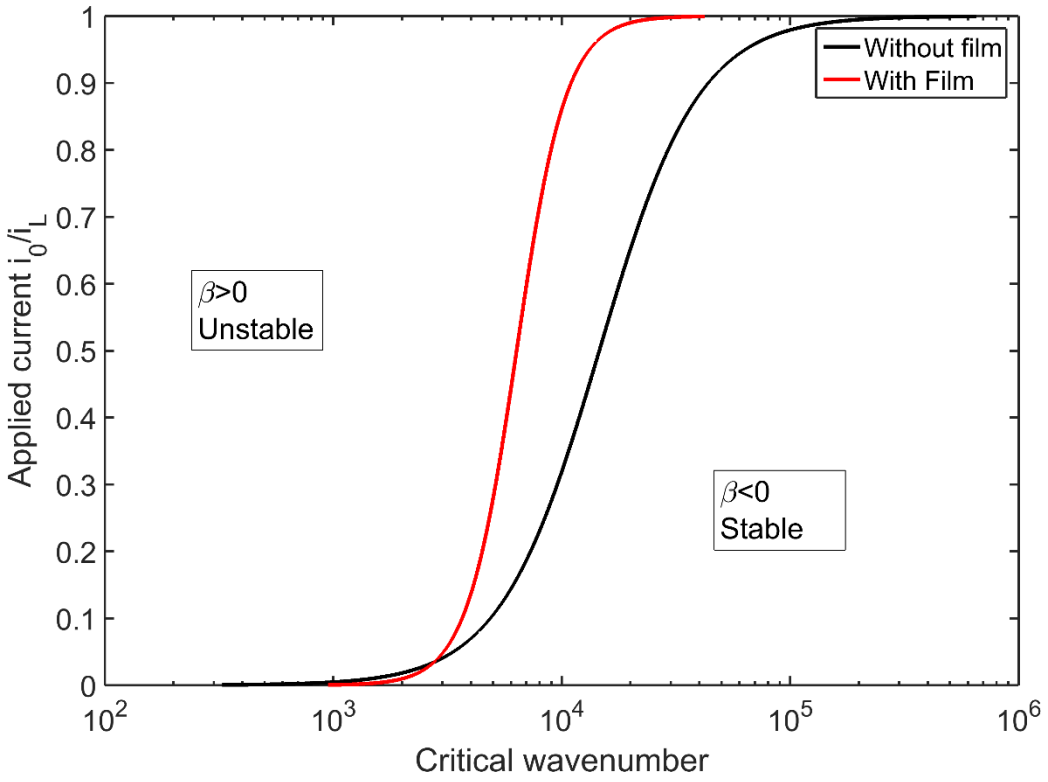

Figure 4.3 The relationship between the critical wavenumber and the applied current can be described by the critical wavenumber curve. Each curve separates the quadrant into two regions. The growth rate of the perturbation is positive on the left hand side of the curve, corresponding to unstable surface. The growth rate of the perturbation is negative on the right hand side of the curve, corresponding to stable surface. It is clear that the existence of film stabilizes the surface at a smaller critical wavenumber.

Using the parameters of Table 2 as a reference case, each parameter for the film properties can be varied at a time to show the effect of the corresponding parameter. Figure 4.4 shows the effect of changing the Young's modulus. As G is increased, the critical wavenumber curve moves towards smaller wavenumbers, resulting in a larger stable region. The line styles for the reference case and the case without film are kept the same as in Figure 4.3 for clarity.

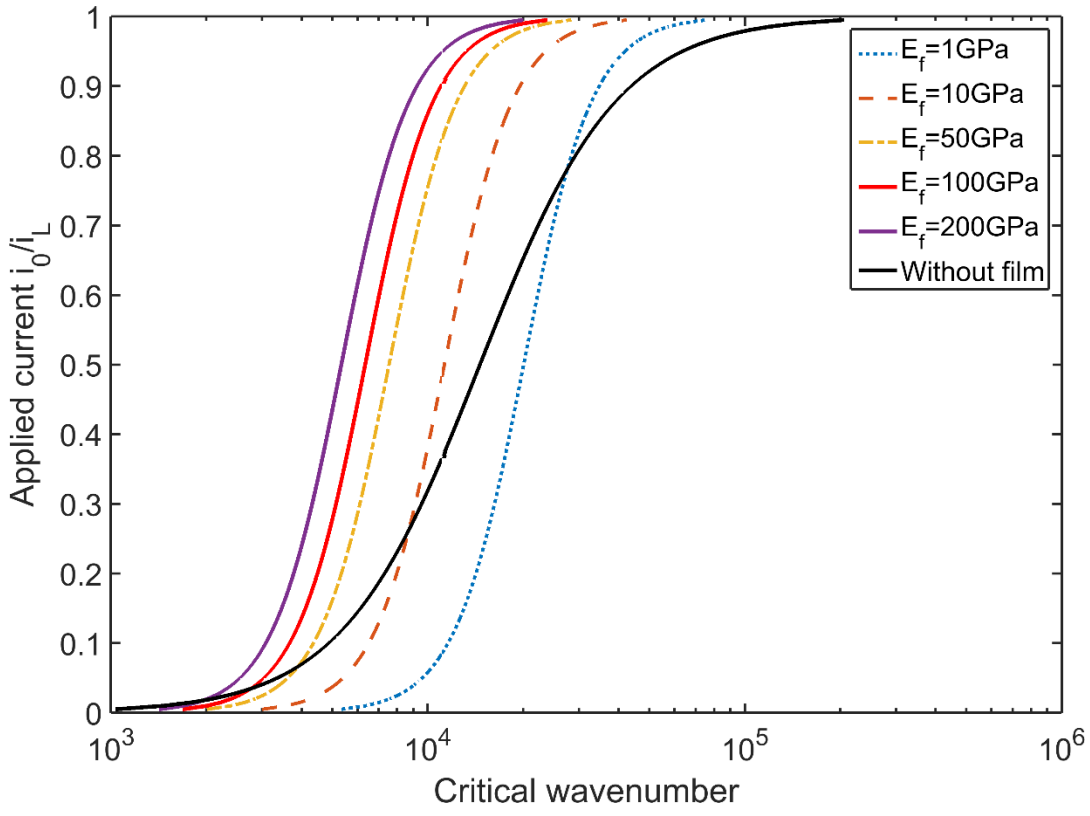

Figure 4.4 The effect of changing Young's modulus of the film. As the Young's modulus increases, the critical wavenumber curve shifts to the left, which means the surface is stabilized at a smaller critical wavenumber.

The effect of changing Poisson's ratio is not as noticeable since the range of viable Poisson's ratio is relatively narrow, although the larger Poisson's ratio shifts the critical wavenumber curve slightly more towards smaller wavenumbers (Figure 4.5).

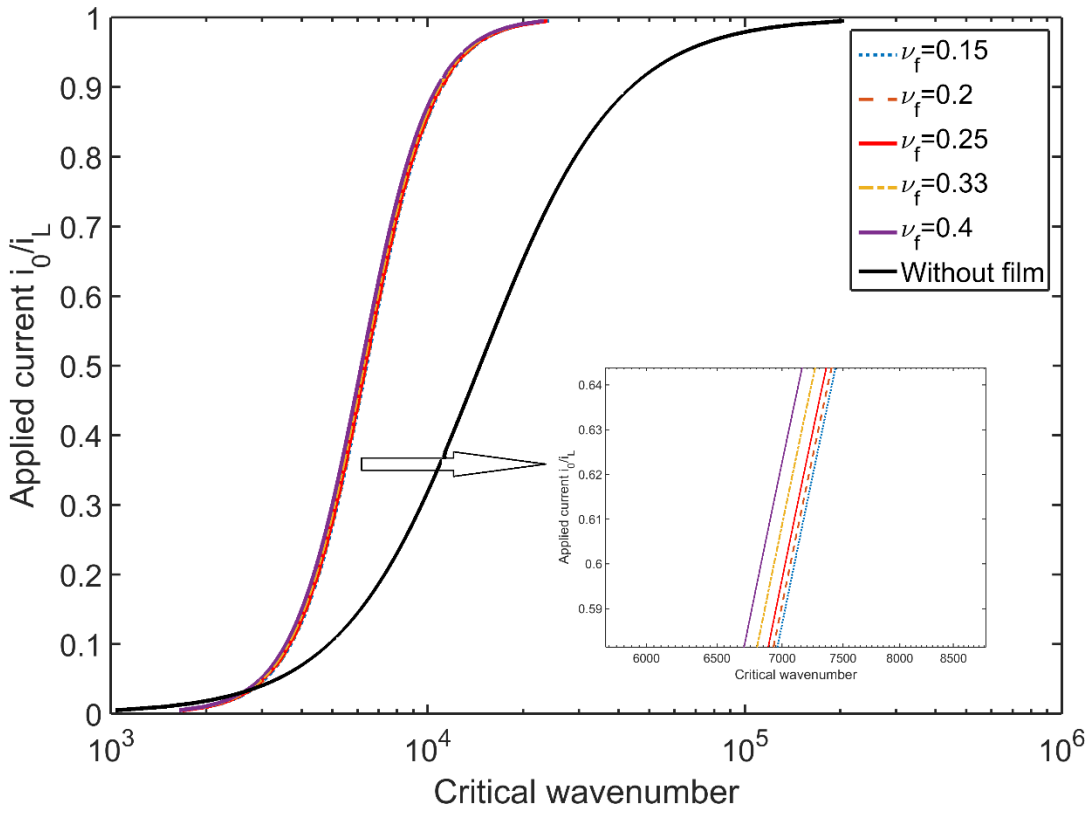

Figure 4.5 The effect of changing Poisson's ratio of the film. As the Poisson's ratio increases, the critical wavenumber curve shifts slightly to the left. However this effect is minimal as the range of Poisson's ratio is restricted.

The most efficient way to tune the system is to change the thickness of the film as it affects the critical wavenumber according to its power of 0.75. As the thicker film improves the dendrite suppression by shifting the critical wavenumber curves towards the smaller wavenumber (Figure 4.6). Note that the film of thickness larger than 5 μm results in a critical wavenumber curve that lies entirely to the left-hand-side of the curve of the case without film. This means even for very

low current situations, the film of such thickness can still be very effective in compressing the dendrite growth.

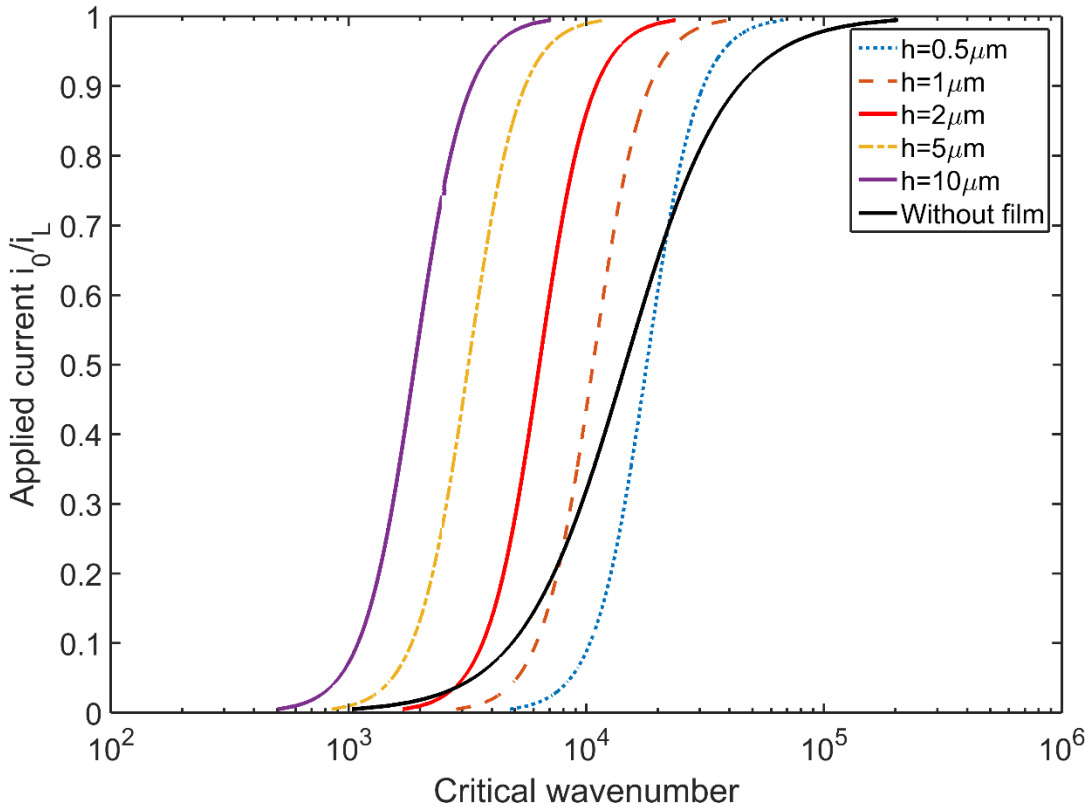

Figure 4.6 The effect of changing thickness of the film. As the thickness increases, the critical wavenumber curve shifts to the left, which means the surface is stabilized at a smaller critical wavenumber.

It is noteworthy that the above results are all based on the assumption of fully supported electrolyte. If the applied current exceeds the limiting current, the concentration near the electrode surface would drop to zero, which would make the analysis much more complicated thus is not pursued here. Another important assumption in this analysis is the elastic deformation of the electrode. Ferrese and Newman [104] in their paper argued that the mechanical blocking would result in plastic deformation of the lithium electrode, and providing a much larger impact on the dendrite suppression. Our model can also be easily extended into the plastic deformation domain with a relationship describing the change of the free energy associated with the plastic

deformation. However, using the parameters in Table I, and the perturbation magnitude of 0.1 μm, the maximum stress from our model is about 0.3MPa. It is less than the yielding strength (0.655MPa) claimed by Ferrese and Newman [104]. Thus the linear perturbation analysis in this chapter holds valid with the elastic deformation assumption.

To compare with Monroe and Newman's paper [33], we can use the $Li_{6.5}La_3Ta_{0.5}Zr_{1.5}O_{12}$ (LLZO) material as a reference material. The corresponding shear modulus of LLZO is about 50 GPa, which is much larger than the 10 GPa critical modulus Monroe's analysis suggested. However, dendrite formation has still been observed in LLZO at moderate current densities (0.5 mA/cm^2) [105]. We believe this is because Monroe's analysis was based on the assumption that the solid electrolyte is thick enough to be considered as a semi-infinite plate, which in most cases of the experiments is not true. Instead, the solid electrolytes are usually kept thin and should be treated as thin film in mechanical stress analysis.

Linking back to the in-situ experiments in Chapter 2, a critical wavelength of 0.5 mm may not be good enough to ensure there would be no short circuit. As shown in the SEM observation in Figure 2.6, the deposited lithium, even though appeared with a relatively large wavelength in the scale of millimeters, can still pose hazard due to its needle shaped nanostructures. One can further increase the critical wavelength by increasing the modulus and thickness of the film, but in fact, 200 GPa used in this demonstration calculation is already larger than the modulus most solid electrolyte known. For example, the aforementioned LLZO is one of the strongest solid electrolyte, and has a Young's modulus of 150 GPa [105]. That means we need to go thicker with the current solid electrolyte materials. But it would lead to another problem of larger impedance, which is not desirable due to the power requirements in most battery applications.

Thus the analysis of this chapter motivates us to search for a new strategy in addition to the mechanical blocking strategy.

4.6 Conclusion

A modified Butler-Volmer equation describing the effect of mechanical blocking layer and surface tension is derived based on free energy change. The derivation shows that the mechanical effect on the reaction kinetics has two contributions: shift of the equilibrium and scale of the reaction current density. A full model coupling the diffusion and electro-migration driven dendrite growth and the stress impact is implemented. Perturbation analysis is carried out to provide the solution to the full model in the large wavenumber domain with the assumption of fully supported electrolyte and elastic deformation. The results show that the addition of the film can significantly decrease the critical wavenumber and thus suppress the growth of the dendrite. The critical wavenumber equation derived can be used as instruction of film material choices. However, the current solid polymer electrolyte materials have much smaller modulus than the reference value used in Table 2, thus many designs failed because either the film is not strong enough or not thick enough. As discussed in the literature review in Chapter 1, adding thickness would also introduce more impedance and resistance into the system, which are not desirable. This motivates us to think beyond the mechanical blocking strategy and come up with new directions in suppressing lithium dendrite growth.

4.7 List of Symbols

$r_{i\to j}$	Reaction rate of the direction i→j
U_i	Total energy of the state i

μ_i	Chemical energy of species i
z_i	Charge number carried by species i
T	Temperature
n	Number of charges
ϕ	Electric potential
a_i	Activity of species i
α	Charge transfer coefficient
$\Delta_m \mu_i$	Chemical energy of species i change due to mechanical deformation
G	Gibbs free energy
S	Entropy
P	Pressure
V	Volume
q	Deflection amplitude of thin film
N_i	Number of moles of species i
ε_{ij}	Strain components ij
σ_{ij}	Stress components ij
$\overline{V_i}$	Molar volume of species i
ω	Frequency of surface waviness
λ	Wavelength of surface waviness
N_{ij}	Membrane force components ij
T_i	Film stress components i
u_i	Displacement components i
A	Amplitude of surface waviness
$\mathbf{N}_i$	Flux of species i
c_i	Concentration of species i
f	Surface profile
i	Current density
β	Growth rate of the waviness amplitude

Chapter 5

Lithium Dendrite Suppression with Piezoelectric Separator

5.1 Introduction

Experimental efforts to suppress lithium dendrite formation and growth have been focusing on electrolyte innovation and modification [106]. Organic electrolytes were found to be promising thanks to the formation of a passive film called solid-electrolyte interphase (SEI), which might potentially stabilize the lithium metal surface over time. Unfortunately, most researchers found that the SEI film, with its limited flexibility, could be easily cracked by the dramatic morphological changes of the lithium metal caused by the non-uniformity of the deposition current density, thus failed to suppress the dendrite formation and caused more lithium loss due to the SEI re-formation at the broken points [107]. Further efforts have been made by changing the components of the electrolyte in form of solvents, salts and additives in order to improve the stability and uniformity of the SEI film [53], [108].

Solid electrolyte has also been explored extensively to mechanically block the growth of lithium dendrite [109]. The basic idea is to utilize the effect that the elastic energy resulting from the lithium metal deformation can change the reaction over-potential and influence the electro-deposition rate locally [32], [33]. However, later researches showed that plastic deformation would always be associated with lithium metal, thus the resulting elastic energy will be distributed rather than stored locally, making the mechanical blocking feedback less effective

than desired [35], [110]. This means even larger elastic modulus is needed for solid electrolyte, but current results suggest the available materials might not be strong enough to serve the purpose. In addition, the poor ionic conductivity and the large concentration gradient during operations will favor dendritic growth, thus further hindering the success of solid electrolyte in general [79]. Gel electrolytes and stiff separators are being tested in hoping of solving these issues, but both still face challenges such as low ionic conductivity and high impedance [111], [112].

Applying a coating layer on top of lithium metal surface has also been a popular strategy to suppress lithium dendrite formation. In addition to the mechanical blocking purpose similar to solid electrolytes, coating layer can also introduce a negative feedback mechanism into the deposition kinetics, so that when dendrites try to grow, the over-potential distribution would favor flattening the surface. However, current approaches usually focus on shear hardening effect, which is a secondary order effect, and might not be sufficient to serve the dendrite suppression purpose [113].

In this article we report an experiment discovery that using a piezoelectric film as separator can help suppressing the formation of lithium dendrite and stabilize the lithium surface during electro-deposition. This finding suggests a new approach to suppress dendrite formation by utilizing the negative feedback mechanism where a negative over-potential would appear when the piezoelectric film is mechanically deformed by the surface protrusion, which would slow down the local deposition rate at the instability point, resulting in a flattened surface morphology. Unlike mechanical feedback, piezoelectric feedback is a first order effect that is very localized, thus can help stabilize the lithium surface during deposition process.

5.2 Methods

Mechanical blocking strategies for lithium dendrite suppression often suggest a critical wavenumber such that for any dendrite with smaller scale than the critical wavelength would be suppressed effectively. The typical critical wavelength is in the range of $10^{-5} – 10^{-3}$ m, which depends on the blocking materials used. However, the in-situ study showed that mechanical blocking can only be effective over a limited deposition period. Once a lithium dendrite gets in close contact with the separator, which is almost inevitable due to the quick volume expansion of lithium during deposition, there is a high chance that the dendrite will penetrate the separator. In the SEM study in Chapter 2, we can see that although seemingly harmless in micro-scale, these lithium dendrites have sharp 'needle' shapes in nano-scale. These sharp tips of the dendrites keep pushing the separator until penetration happens at certain local points. This result suggests that the mechanical blocking effect, although very intuitive, may not be effective enough to suppress the local structure of dendrites, thus is limited in short circuit prevention.

In this chapter, we proposed a new strategy, which utilizes the piezoelectric property of polyvinylidene fluoride (PVDF) film to suppress lithium dendrite growth. The intuition of this strategy is to generate a counter over-potential, which helps offset the concentration over-potential cause by the spherical diffusion at the tip of the dendrite, thus suppressing the further growth of the dendrite. The concept is illustrated in Figure 5.1. Piezoelectric film, after polarization under high voltage field, will accumulate opposite charges on each surface and generate potential across the film when deformed. Unlike the mechanical blocking mechanism, piezoelectric feedback is a local effect, as the overpotential across the film at each local region will be directly related to its local deformation. This means the piezoelectric film will try to

suppress the growth of protrusions of any scale, thus providing a much more stable surface morphology during lithium deposition.

Here we demonstrate the comparison between the mechanical blocking effect and the piezoelectric feedback effect with a simple reaction kinetics model inspired by Monroe's work [32]. In the mechanical blocking scenario, one can assume the lithium deposition kinetics is influenced by the mechanical deformation of the solid blocking material due to dendrite growth, and this deformation overpotential would be proportional the elastic energy. We can use the strain energy due to volume change as estimation of the elastic energy since the strain energy due to distortion would be secondary effect, and the resulting deformation overpotential is $(\sigma_h \Omega)/F$. σ_h is the hydrostatic stress, Ω is the molar volume for a lithium molecule, and F is the Faraday constant (96485 C/mol). This deformation overpotential would compete with the concentration overpotential trying to stabilize the lithium surface, and a critical wavelength below which the dendrite would not grow at given current density. As the stress is proportional to the strain and the material elastic modulus, this suggests that stronger solid electrolyte or separator could have a larger critical wavelength and be more effective in suppressing the dendrite growth. In the case of piezoelectric feedback scenario, in addition to the deformation overpotential of the mechanical blocking effect, a piezoelectric overpotential would also be generated when the film is deformed by the dendrite growth. This overpotential is directly proportional to the local stress and the piezoelectric constants of the film. One can estimate the piezoelectric overpotential as $gh\sigma$, where g is the piezoelectric constants that represents the voltage generated by a piezoelectric material per unit of mechanical stress applied, and h is the thickness of the film. Recall that the deformation overpotential is proportional to the hydrostatic stress and the coefficient is in the magnitude of 10^{-9}. The proportion of piezoelectric overpotential to the stress, however, is in the

order of 10^{-7} for PVDF film of 25 μm thickness (typical thickness of commercial Celgard separator). So with a PVDF film as separator, we could get a much larger critical wavelength and a more effective dendrite suppression result.

Using PVDF as separator was explored by Kim etc. to design self powered lithium battery that convert mechanical energy into chemical energy [114]. However, commercial PVDF film has very low porosity, which is hard for lithium ions to transport through. To deal with this challenge, we follow the paper's method to synthesize porous PVDF film by removing ZnO nanoparticles from PVDF matrixes to introduce more porosity (Figure 5.1(b)) while forming more beta-phase (which is the phase that has strong piezoelectric effect). XRD result (Figure 5.1(c)) shows the complete removal of ZnO in the film and strong peak of beta phase. (XRD results for PVDF with ZnO embedded film is included in Appendix A, where strong peaks for ZnO can be observed.) Another desired property of PVDF is that it's transparent once wetted by the organic electrolyte (Figure 5.1(d)). This allows us to observe the lithium deposition directly under the film, giving more insights of the lithium morphology change during deposition. The fabricated PVDF film showed that the piezoelectric parameters are consistent with other results in testing (Figure 5.1(e)). To elaborate, one can simply divide the response voltage by the applied strain and get the d_{31} piezoelectric constant of the film (this constant quantifies the magnitude of voltage response when applying a lateral strain). The results showed that the fabricated film has a d_{31} constant about 1.2 pC/N, which is smaller than that of the commercialized product (about 5 pC/N), suggesting there is still room to improve in the fabrication process.

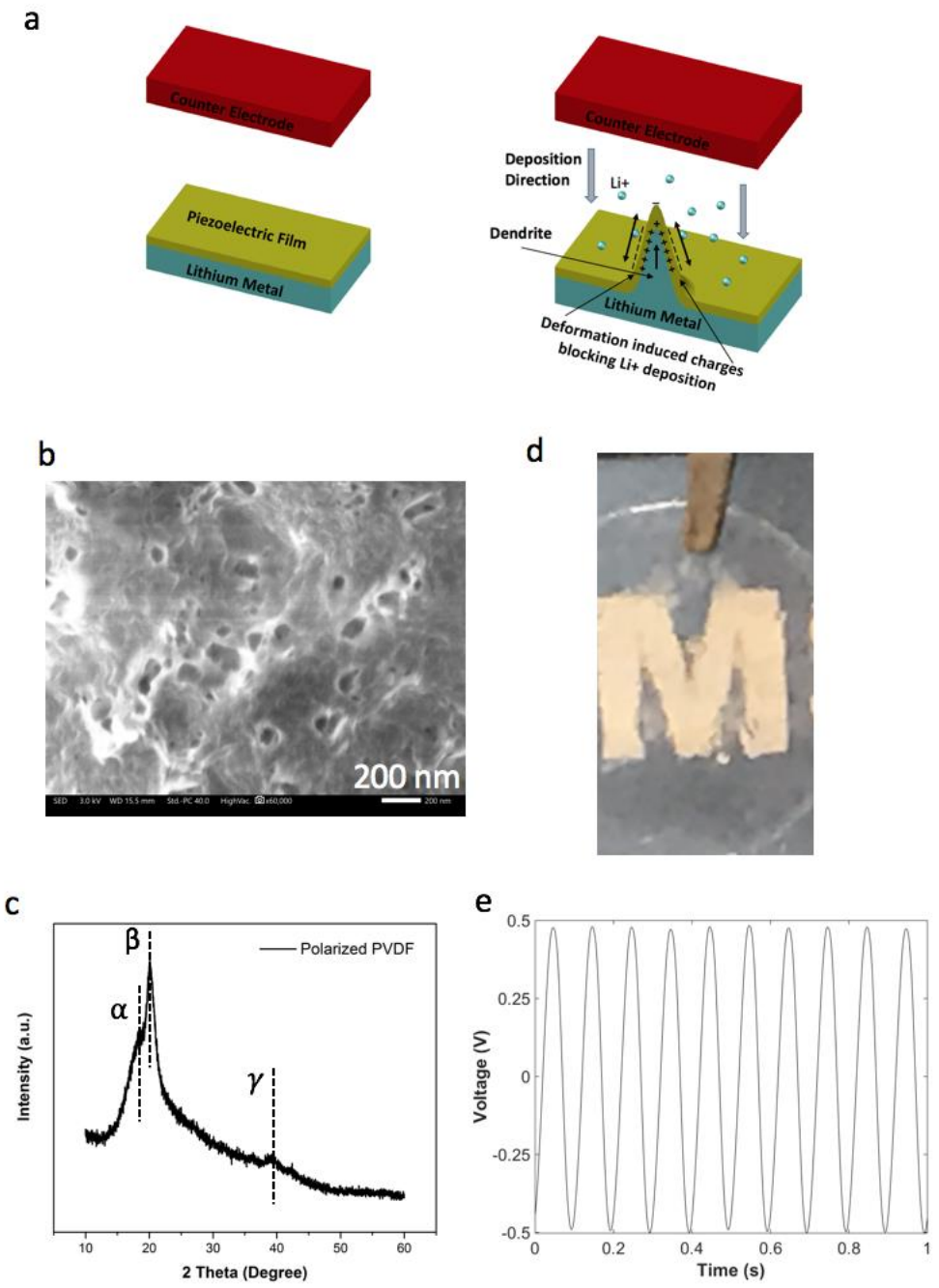

Figure 5.1 Concept of piezoelectric feedback and PVDF film properties. (a) Illustration of using polarized PVDF film to suppress lithium dendrite growth. (b) SEM image showing microporous structure of the PVDF film fabricated. (c) XRD results showing the growth of beta-PVDF and complete elimination of ZnO. (d) Transparency of PVDF film when wetted by organic electrolyte. (e) Characteristic piezoelectric signal obtained for an external applied strain of 1%, confirming the piezoelectric behavior of the fabricated PVDF film.

5.3 Results

To illustrate the benefits of piezoelectric effect of PVDF film, we compare the non-polarized (NP) PVDF film with the polarized (P+) film under the same deposition condition. As deposition onto a lithium substrate will fail at random points which are hard to capture under microscope, we modified the in-situ cell in Chapter 2 to use a copper needle as the deposition substrate. This allows us to focus onto the tip of the copper needle as it is highly probable that the penetration will happen in this region. This also accelerates the experiment as the current density is very large in this tip area. Before applying the current, the film is loosely placed on top of the copper needle. As shown in Figure 5.2(a), under the current of 2.5 mA (current density about 200 mA/cm^2), the NP film only survived about 5 minutes before getting penetrated by the lithium dendrite. In comparison (Figure 5.3(b)), the P+ film was able to suppress the lithium deposition at the tip area, thus leading to a flat lithium surface after 1 hour of deposition with no signs of penetration.

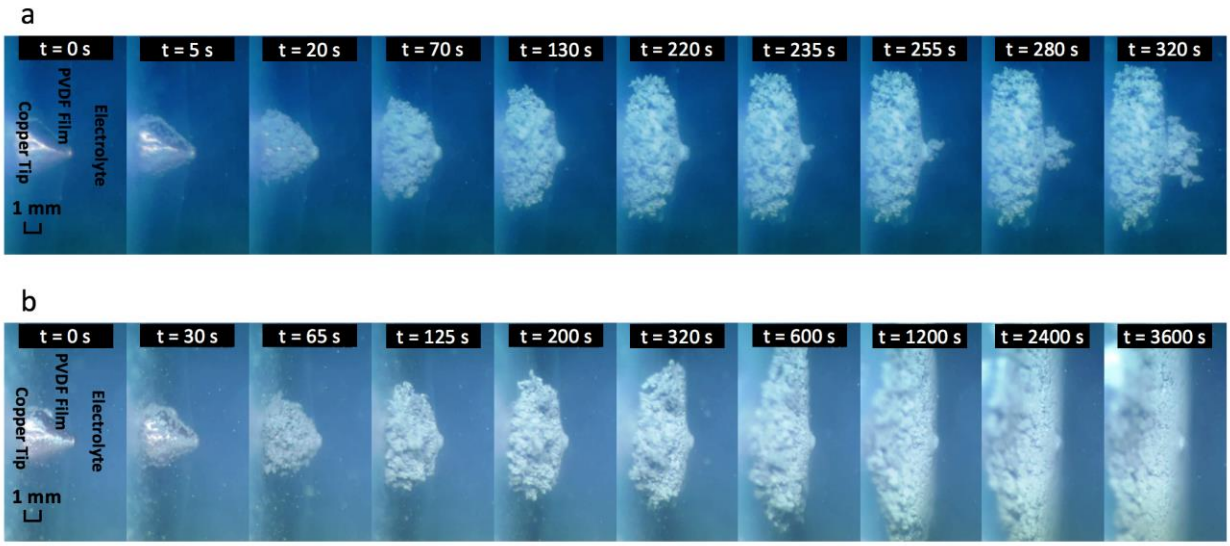

Figure 5.2 Comparison between NP and P+ PVDF film under applied current 2.5 mA (about 200 mA/cm^2). (a) NP film got penetrated after 10 mins. (b) P+ film successfully confined the deposited lithium into a flat surface.

This result is a direct proof that the piezoelectric effect of the PVDF film can provide further dendrite suppression in addition to its inherent mechanical blocking effect. For both the NP and P+ setups, initially lithium deposition onto the copper tip is unconstrained as the PVDF film is not in close contact with the copper electrode surface. Naturally due to spherical diffusion, the lithium deposition rate will be higher in the tip region than the base region of the copper electrode. As the gap between the film and the copper tip gets filled by the deposited lithium and SEI formation at the same time, the film is deformed locally. In the NP case, the deformation at the tip will generate a small elastic energy, which would impact the reaction kinetics such that further deposition in the deformed area is less energy favorite. However, as the elastic energy is small, it is not enough to counter the effect of spherical diffusion. Thus the dendrites will keep growing and eventually penetrate the PVDF film. In a real battery setup, as the counter electrode will also be close contact with the separator, this will lead to short circuit immediately. In the P+

case, in addition to the mechanical blocking effect, an electric overpotential will be generated due to the deformation. By placing the piezoelectric film in said orientation (pressing the film will generate an electric film pointing outward from the copper electrode), the piezoelectric overpotential will impact the overall overpotential and slow down the deposition at the tip region. Since this piezoelectric feedback is very local and relatively strong, the lithium dendrites will be suppressed successfully. In the end, the deposited lithium is confined nicely by the film and would not pose short circuit threats.

Apparently due to the current fabrication restrictions, such as non-uniform thickness at certain local points of the film and lower piezoelectric constants comparing to the commercial film, the film would still be penetrated when applying current density 3 mA which corresponding to 240 mA/cm^2. However, there is another interesting behavior of the PVDF before the penetration happens. As show in Figure 5.3, the voltage increases significantly before the penetration happens (at around 80 seconds). This suggests that the piezoelectric film could potentially alert the system that the cell is experiencing a huge protrusion in a local point of the separator and a short circuit could potentially happen. Thus the system can shut off the cell from the application network. One can consider this as a safety fuse feature of the piezoelectric film.

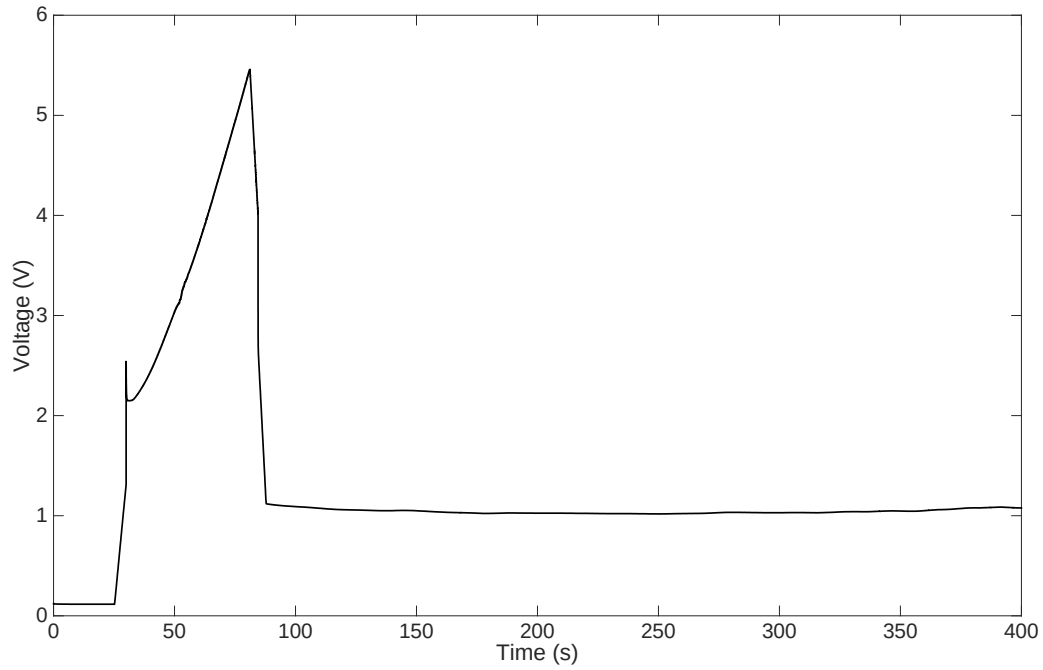

Figure 5.3 The voltage profile of the P+ in-situ cell setup under current 3 mA. Before the lithium dendrite penetrates the film at around 80 seconds, there is a significant increase in the voltage signal. The sudden voltage drop suggests the occurrence of the penetration.

Another demonstration of the suppressing effect is to use lithium foil with manually deformed surface morphology as deposition substrate. Figure 5.4 shows that as the deposition goes, the lithium surface got flattened by the P+ PVDF film. In real lithium metal batteries, the manufacturers will try their best to produce a flat surface for the lithium metal. However, in the extreme cases, the lithium surface might become uneven due to scratches during the cell assembly or large deformation of the cell enclosure. This result shows that even with an uneven lithium surface, the P+ PVDF film is able to confine the deposited lithium to a flat surface, eliminating the threats of short circuits due to unevenly distributed lithium deposition.

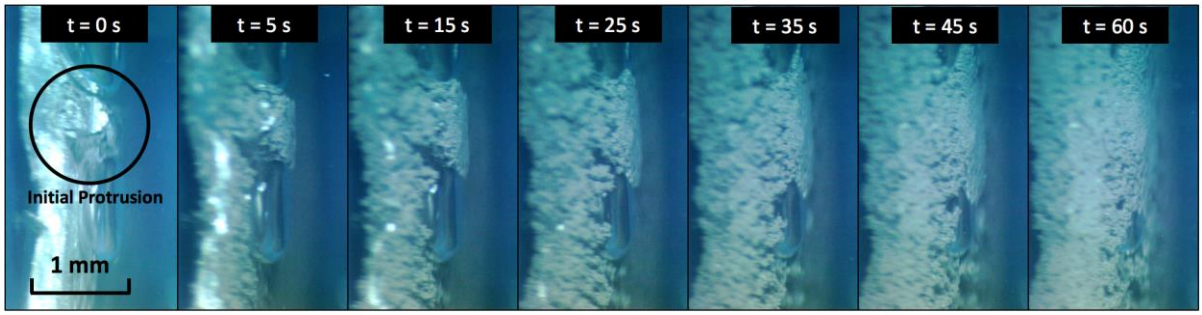

Figure 5.4 Manually perturbed lithium surface will grow flat under the dendrite suppression effect of PVDF film.

To further demonstrate the benefit of piezoelectric effect on suppressing the lithium dendrite growth, Li vs Cu coin cells were assembled to evaluate the performance of PVDF film separator in a half cell configuration. Two type of cells were compared: cell with two NP films as separator (NPNP), cell with one P+ film at the lithium surface and one P+ film at the copper surface (P+P+). The second cell type is assembled so that both P+ were placed in the orientation to suppress the dendrite formation on its respective electrode surface. Unlike the in-situ cell setup, in the Li vs Cu coin cell, both lithium and copper electrode are in direct contact with the separator, which is the reason that we put two PVDF films, one for each electrode. Figure 5.5 shows that P+P+ cells can survive more cycles without short circuits than NPNP cells under the same current density. Under a typical current density (1 mA/cm^2), the P+P+ cell can survive 300 cycles (175 hours) without showing any short circuit failure while NPNP cells can only survive 180 cycles (about 110 hours). In the highlighted area by the red circle, it is clear there was a voltage break down for the NPNP cell, indicating short circuit, while for the P+P+ cell, the voltage is very stable over the whole testing period. As suggested by most researchers, lithium metal battery is more vulnerable to short circuit failures at larger current density. So more

experiments data would be collected for different current density to confirm the consistent P+ superiority over NP film. But with the current results we have, it is clear that P+ film performs better than NP film even in a Li vs Cu half-cell scenario.

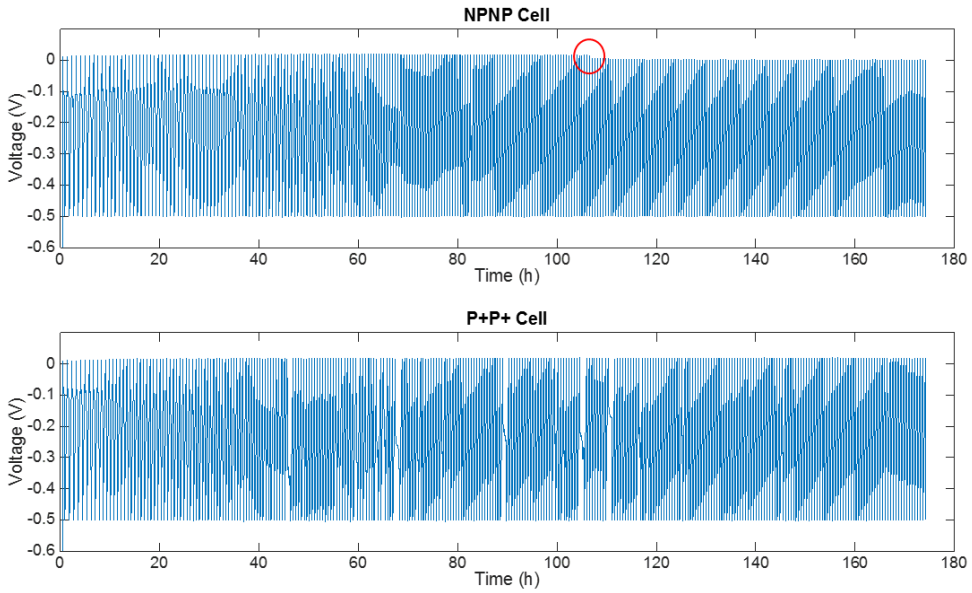

Figure 5.5 Comparison of survived cycles for P+P+ cells and NPNP cells.

To test the performance of polarized PVDF film in a full cell configuration, we chose LTO as the cathode material as it doesn't suffer from intercalation stress and has a stable voltage plateau at around 1.5V against Li [115]. LTO vs Li coin cells were assembled with one P+ film at the lithium surface (LTO P+). The cell was charge/discharged with 1C rate to allow enough lithium to be transported during each cycle to form dendrites and potentially cause short-circuit. Figure 5.6 shows LTO P+ cells can survive 1000 cycles without short circuits. However, due to using the commercial $LiPF_6$ electrolyte, the Coulomb efficiency (Figure 5.7) decreases quickly over the first few cycles, but stabilizes around 75%, which is consistent with literature values.

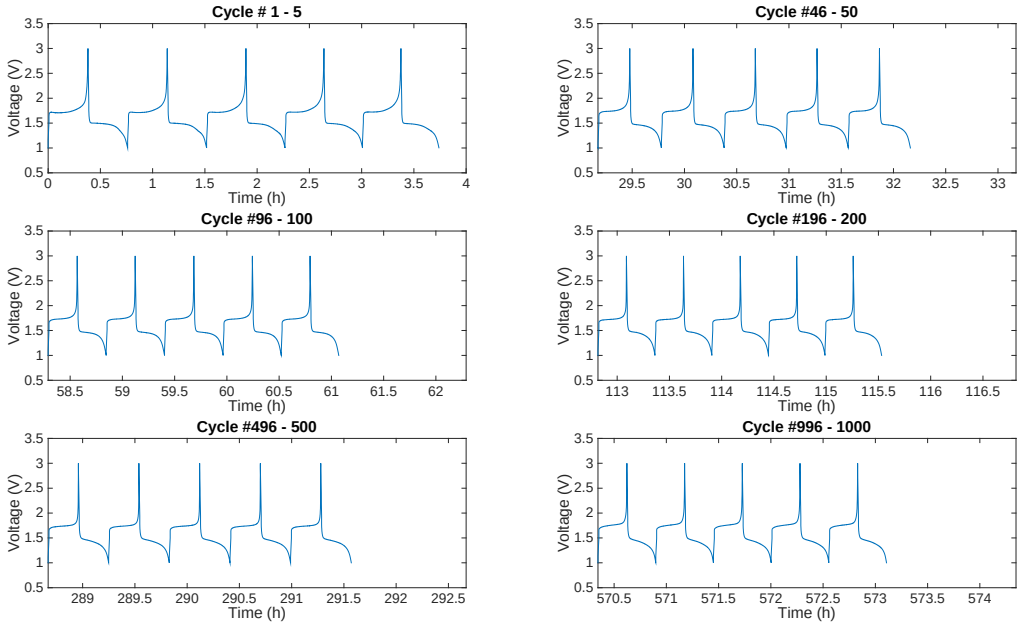

Figure 5.6 LTO P+ cell cycling performance over 1000 cycles.

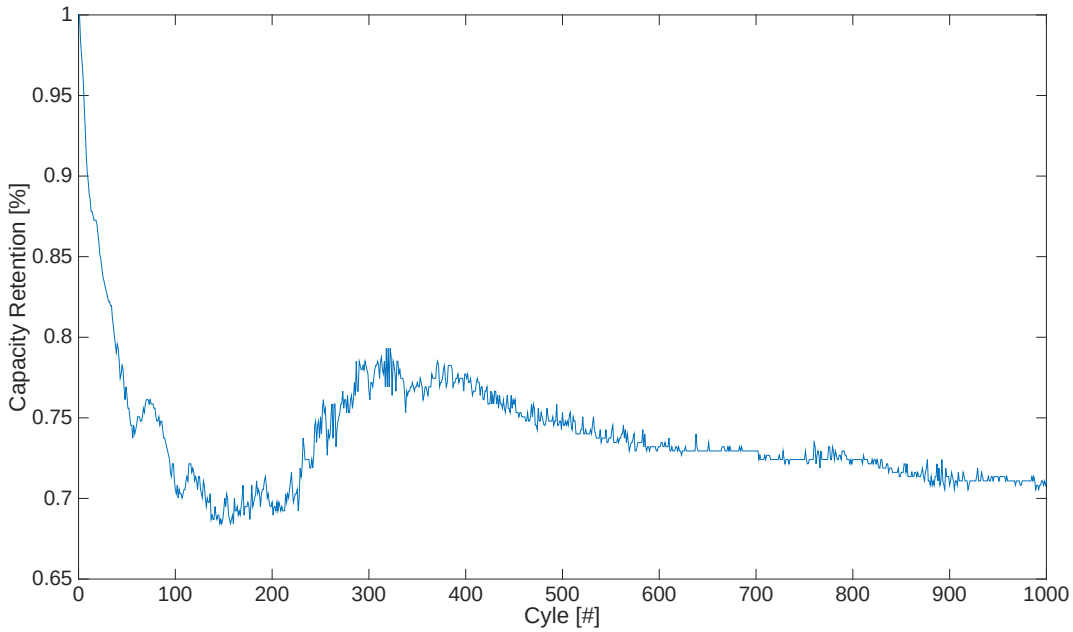

Figure 5.7 Coulomb efficiency of LTO P+ cell over 1000 cycles.

5.4 Conclusion

We discovered that using polarized PVDF film as separator can help suppressing lithium dendrite growth and stabilizing the lithium metal surface morphology during the charging process of lithium metal battery. This can be explained by the negative over-potential generated by the piezoelectric feedback of the PVDF film when it's deformed by the surface protrusions. The concept of using piezoelectric material to suppress lithium dendrite growth provides us a new direction to explore to solve the challenges in lithium metal battery design.

Chapter 6

Design of Power Fluid Battery System

6.1 Introduction

Advanced battery technology is critical for vehicle electrification. The performance of current Li-ion batteries faces several significant challenges in capacity, charging time, cycling life and cost. The United States Advanced Battery Council (USABC) has requested that a battery pack in electrical vehicles (EVs) should be able to support for a driving range of 400 miles, 80% of capacity retention after 1000 cycles, and product quality guarantee of 15 calendar years [116]. These standards, although pursued diligently by researchers, are difficult to reach for many battery chemistries with the current pack design. To compensate the capacity drop in severe temperature weather conditions and capacity loss associated with charge/discharge cycling, battery packs in current EVs are designed with up to 50% over-capacity, which significantly increases the weight and reduces the driving range per charge. Meanwhile, current battery packs usually take hours to be fully charged. For example, it takes 9.5 hours for a Tesla 85kwh battery pack to be charged with a 240 volt single charger to provide a driving distance of about 300 miles. Battery cost is a critical factor that hinders the popularization of EVs. Taking the Tesla as an example, customers need to pay an additional $10,000 simply to upgrade the default 60kwh battery to an 85kwh one [117].

The high battery cost is partly due to the fact that battery packs need intensive re-engineering of customized size and shape to fit in the different vehicle model and demand sophisticated cooling systems. In addition, it is very expensive to take advantage of new battery chemistries during the 8-10 year service time of a battery pack since it requires changing the entire back. To address these challenges, we propose an innovative fluidic battery system composed of many micro batteries [118] for EV and other energy storage applications.

6.2 Advantages

As shown in Figure 6.1, each micro battery is a self-contained Li-ion battery enclosed in an insulating shell, and can charge/discharge wirelessly or through contacts. Unlike the traditional "flow battery" which requires two active chemical components dissolved in liquids and charge/discharge through a membrane and redox reactions, the micro battery is each solid-state and self-contained. Thus it does not have the challenges associated with the tradition flow battery such as low energy density, corrosion, need of a secondary containment vessel, and relatively complicated controls for flow and mixing. At the same time, the architecture can offer high energy density, power density, and performance of a Li-ion battery. To maximize the benefit of this design, all solid state lithium metal battery would be ideal since the specific energy is high.

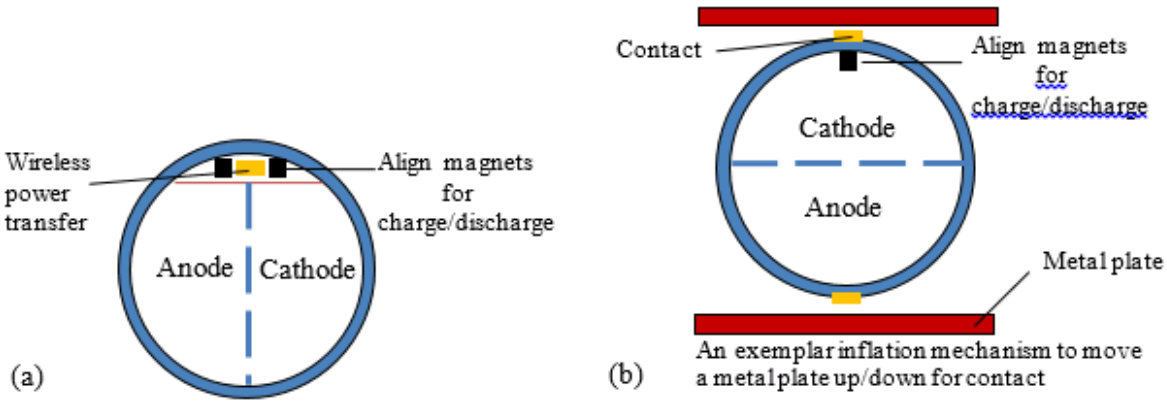

Figure 6.1 Schematic of a micro battery. Each micro battery is a self-contained Li-ion battery enclosed in an insulating shell, and can charge/discharge (a) wirelessly or (b) through contacts.

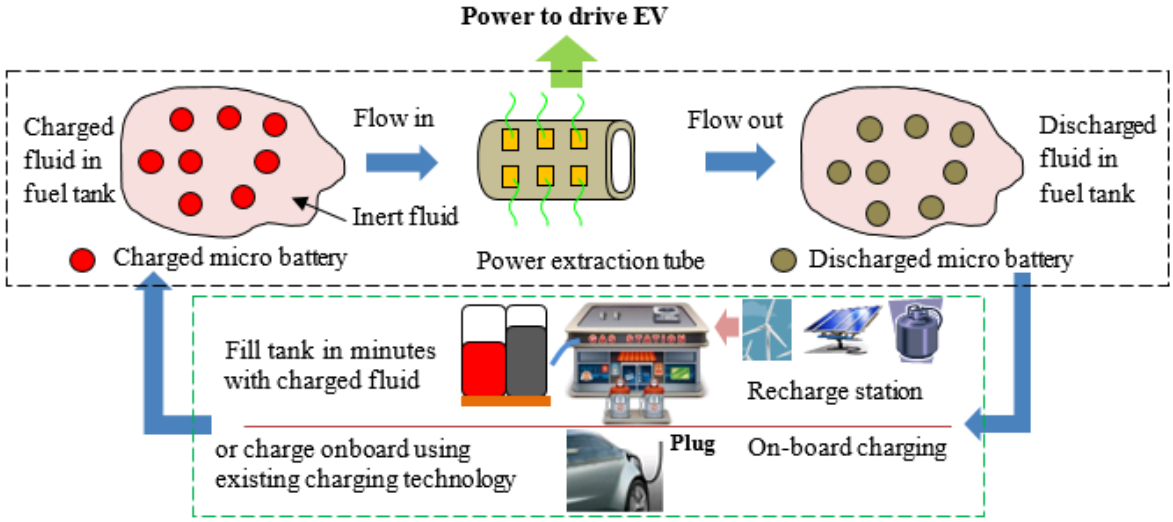

Figure 6.2 Micro batteries are carried by an inert fluid to form a power fluid, which can be charged by the grid or renewable energy sources such as solar and wind at the charge station. An operator refills the car tank with charged fluid (many charged micro batteries) and sucks the discharged fluid (discharged micro batteries) into the charge station to be charged and reused. The process only takes minutes.

Thousands of such micro batteries are carried by an inert fluid to form a power fluid, as shown in Figure 6.2. The fluid can be charged by the grid or renewable energy sources such as solar and wind at the charge station. In fact, the charge station can use the current gas station infrastructure. An operator refills the car just like with petrol. He fills the car tank with charged fluid (many charged micro batteries) and sucks the discharged fluid (discharged micro batteries) into the charge station to be charged and reused. The process only takes minutes. Some key advantages of the proposed micro battery system include: (1) Battery scaling with vehicle life. An average vehicle lasts 10 years. As it ages, the range extends as battery capacity grows with advances in the micro batteries. The proposed micro battery technique would enable progressive improvements of vehicle performance instead of fixed by a production date. (2) Efficient battery operation. The micro battery eliminates the large over-capacity design in the current battery packs, significantly reducing the weight and cost. (3) Ongoing battery recycling. Instead of waiting for the scrap yard, the battery is changed regularly either in refueling or in the maintenance process. (4) Reduced copper wiring. With the cells wireless and mobile, the amount of copper wiring needed for the assembly should drop. (5) Heat self-dissipation. Carry fluid acts as the heat dissipation mechanism, eliminating the need for separate battery temperature cooling fluid. (6) Onboard charging. The battery can also be charged onboard using existing battery charging technology. (7) Flexible geometry. The micro battery can essentially go into a storage space of any geometry, allowing uniform design of battery configurations for diverse applications. (8) Ultra-high safety. Each micro battery is contained in an insulating shell. When an accident happens and damages the system, the micro battery automatically disengages from output. Even if a micro battery itself is severely damaged, the damage is contained within itself and has minimum impact on other micro batteries or the overall operation.

In the following we focus on analyzing several key characteristics of the micro battery system to evaluate its potential benefit and physical limitations. The first question is whether such a micro battery system can provide sufficient energy density since the carry fluid will take space. The volumetric energy density of the system can be estimated by the packing density of micro batteries. Each micro battery is a sphere with a radius *r*. It is widely known that the close packing density, η, of mono-sized spheres is $\pi / 3\sqrt{2}$ =0.74. This is also the maximum possible packing density among mono-sized spheres [119]. The packing density of identical ellipsoids can reach 0.75, which is even higher [120]. When two sizes of spherical micro batteries are used, the smaller spheres can fill in the gap between the larger ones, increasing the overall packing density up to 0.93 [121].

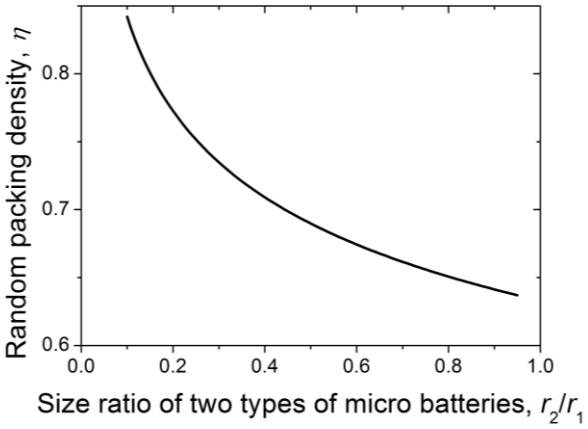

Figure 6.3 Random packing density of a system with two types of micro batteries of different sizes. Their size ratio affects the random packing density.

The lower bound of the packing density can be calculated from random packing [122], [123]. For a system compose of spheres of two given radii r_1 and r_2, the volume ratio of the two spheres affects the packing density. With the appropriate volume ratio, the random packing density reaches an optimized value for a given r_2 / r_1 ratio. For random packing of micro

batteries of two different sizes, our study gives the optimized packing densities for various r_2 / r_1 ratios, as shown in Figure 6.3. By choosing the appropriate radius ratio, the random packing density can easily go over 0.8. These results suggest that even with random packing, the energy density of the system can easily surpass the convention battery pack with over capacity. With appropriate fluid pressure and flow control, the system can achieve states near close packing, allowing even more efficient use of the space.

The conventional battery packs are designed with significant overcapacity. For example, the 35% overcapacity of the Volt battery packs, although is already quite impressive in industry, is still a large amount of unused volume or mass. This overcapacity alone translates to an effective packing density of 0.65 without considering other system overhead such as the cooling system, which further reduces the system level energy density. Thus the micro battery system can achieve volumetric energy density higher than the conventional battery pack using the same battery chemistry.

The next question is whether the micro battery system can provide sufficient specific energy density. We will show that the specific energy density, or energy per unit mass, of the micro battery system will be significantly higher in comparison to the conventional battery pack. Denote the mass densities of the micro battery and the carry fluid by ρ_b and ρ_f, respectively. The mass packing density of the micro battery system, λ, defined as the ratio between the mass of the energy storage material and the mass of the system, is given by

$$\lambda = \frac{\rho_b}{\rho_b + \left(1/\eta - 1\right)\rho_f}. \tag{6.1}$$

The mass density of the carry fluid is smaller than that of the battery, making $\lambda > \eta$. Take a battery with $LiMn_2O_4$ (LMO) cathode and graphite anode as an example. The capacity ratio of LMO cathode/graphite anode in a battery cell is typically 0.9. Based on the theoretical capacities of LMO and graphite, which are 148 mAh/g and 372 mAh/g, respectively, their mass ratio is 2.26 in a battery cell. The densities of Mn_2O_4 and graphite are about 3.25 g/cm^3 and 2.2 g/cm^3, respectively. These quantities give an effective $\rho_b =$ 2.83 g/cm^3. If the carry liquid is water with ρ_f =1 g/cm^3 and the packing density is $\eta = 0.75$, Eq. (1) gives $\lambda = 0.9$. In other words, 90% of the system mass is used for energy storage.

The micro battery system can be maintained at a uniform operation temperature without sophisticated cooling systems due to the small battery size and each battery being fully surrounded by the inert fluid. While in conventional battery packs, dedicated cooling components are needed, yet still resulting in temperature gradient and associated thermal stress and electrode dissolution, and both can cause severe battery degradation. To evaluate the potential weight reduction from the micro battery system, we take the Volt battery pack as an example. The Volt's T-shaped battery pack consists of 288 individual cells arranged into 9 modules. Plastic frames hold pairs of lithium-ion cells that sandwich an aluminum cooling fin. The design and construction of these aluminum plates is critical to ensuring an even temperature distribution with no hot or cool spots across the flat, rectangular cell. The approximate weight of them is 86.7 kg, taking 44% of the weight of the whole battery pack [124]. The proposed micro battery system, however, can make use of the surrounding inert fluid as a coolant at the same time, thus saving the space and weight of the cooling components of the conventional battery packs, making it remarkably efficient in terms of specific energy density and thermal control. With 35% overcapacity and 44% cooling system overhead, the overall effective mass packing

density of the conventional battery pack is about 0.36. The micro battery system can achieve a mass packing density of up to 0.9 for mono-sized micro batteries, which translates to a system weight of only 40% of the conventional battery pack. The weight reduction is even higher for a two-sized micro battery system.

Now we analyze whether the micro battery system can provide sufficient power density. Here we assume that electricity will be extracted from a cross-section of the micro battery system parallel to a collecting plate. This will provide a conservative estimation since the collecting plate can be in a three dimensional form to access more micro batteries at the same time. In this cross-section micro batteries essentially form a two dimensional circle packing. The close packing density is $\pi / 2\sqrt{3}$ =0.91, while the random packing density is 0.84. Therefore the power density will be 80~90% of that can be provided by a battery cell in terms of volume. The specific power will be higher since $\lambda > \eta$. At the system level, a conventional battery pack has 35%~50% overcapacity, leading to an effective 0.65~0.5 packing density, or 65%~50% of the power that can be provided by a battery cell. Considering the 44% cooling system overhead, the overall effective mass packing density of the conventional battery pack is about 0.36~0.28. In other words, the system level specific power is about 28%~36% of that can be provided by a battery cell. Therefore the micro battery system has the capability to provide power density or specific power better than the current battery pack. In addition, the small size of each micro battery offers other benefits. Studies have shown an inverse relationship between the power density and size [125]. In a battery cell, factors such as phase transition, polarization, and fracturing of the electrodes can limit the power density. Multiple mechanisms have been reported to cause battery degradation [88], [126], [127]. The micro battery architecture offers opportunities to improve the battery performance in these areas.

With COMSOL multi-physics, we performed several numerical studies on the interaction between the carry fluid and the micro batteries. Figure 6.4(a) shows the flow of carry fluid with many micro batteries between two parallel plates. There are two holes at the right end for the fluid to exit. The micro batteries concentrate and pack spontaneously around the exit region. The simulations suggest the possibility of using a burst of flow to control the arrangement of micro batteries for charging/discharging. Figure 6.4(b) demonstrates heat self-dissipation of the system. The environmental temperature is 20^{o}C. Operating in the air, the battery temperature rises to 58^{o}C, an increase of 38^{o}C. With carry fluid moving even at a very low velocity of 0.1mm/s, the temperature rise of the battery is less than $0.5\ ^{o}$C. The simulations suggest that the carry fluid is very effective in dissipating heat and maintaining a constant operating temperature. We find that the flow for moving micro batteries and for dissipating heat can work at quite different velocity zones. This de-coupling would provide a significant degree of freedom in experimental control.

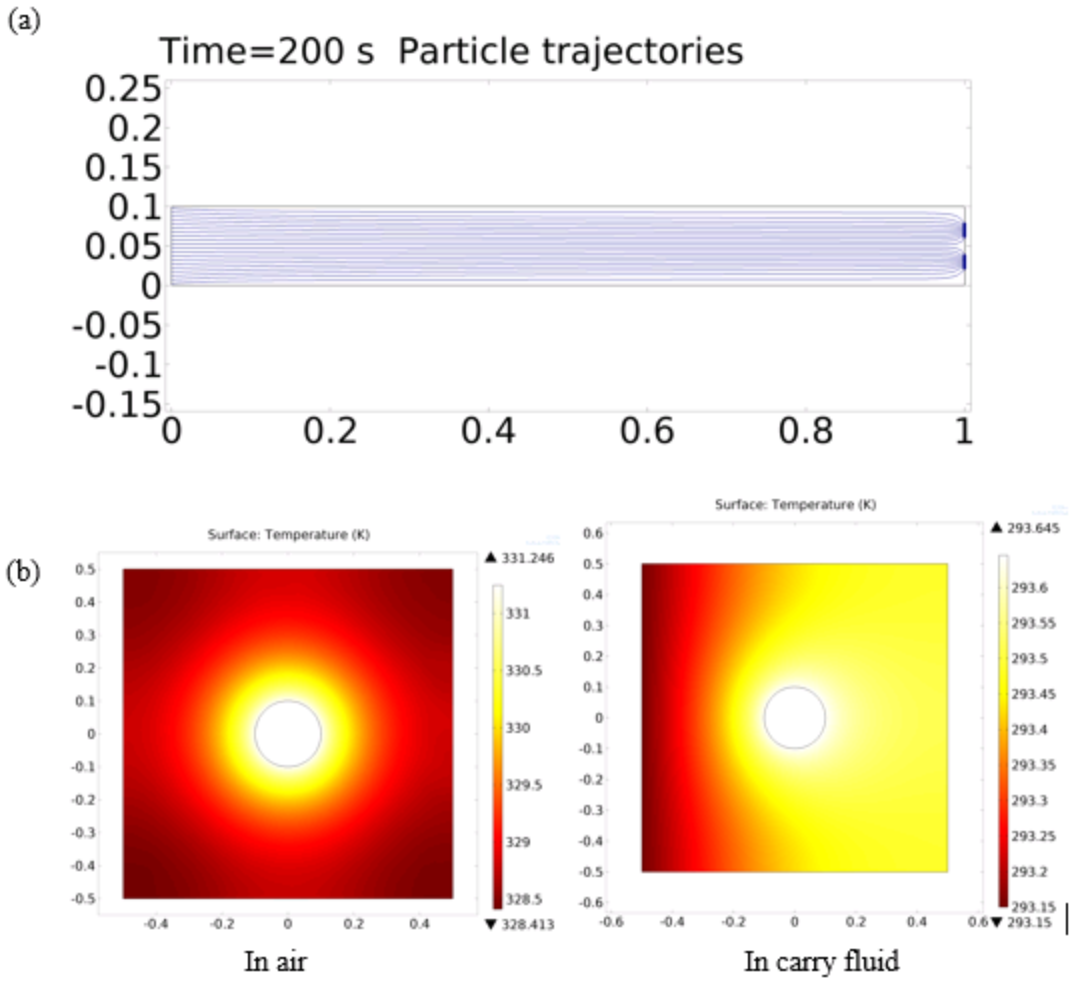

Figure 6.4(a) Flow of carry liquid between two plates. Micro batteries concentrate spontaneously at the two holes on the right end. (b) Temperature distribution of a battery cell in the air (left) and in the carry fluid with a flow velocity of 0.1mm/s (right). The battery temperature rises 38^{o}C in air but less than 0.5^{o}C with the carry fluid.

6.3 Prototype Designs

Theoretical analysis was followed up by attempts to build prototypes with centimeter-size bubble batteries. The first prototype (Figure 6.5) used ping-pong balls to contain coin cells with electrodes made from copper foils glued onto the exterior surface of the shell. The discharging station was built with two parallel PCB plates. The contact between the current collector and the

batteries was achieved by inflation of a square shape balloon. Magnetic alignment was implemented to make sure the orientation of the battery was correct. The purpose of the prototype was to demonstrate the mechanism of the engagement of the battery, and the attempt was successful to light up a LED.

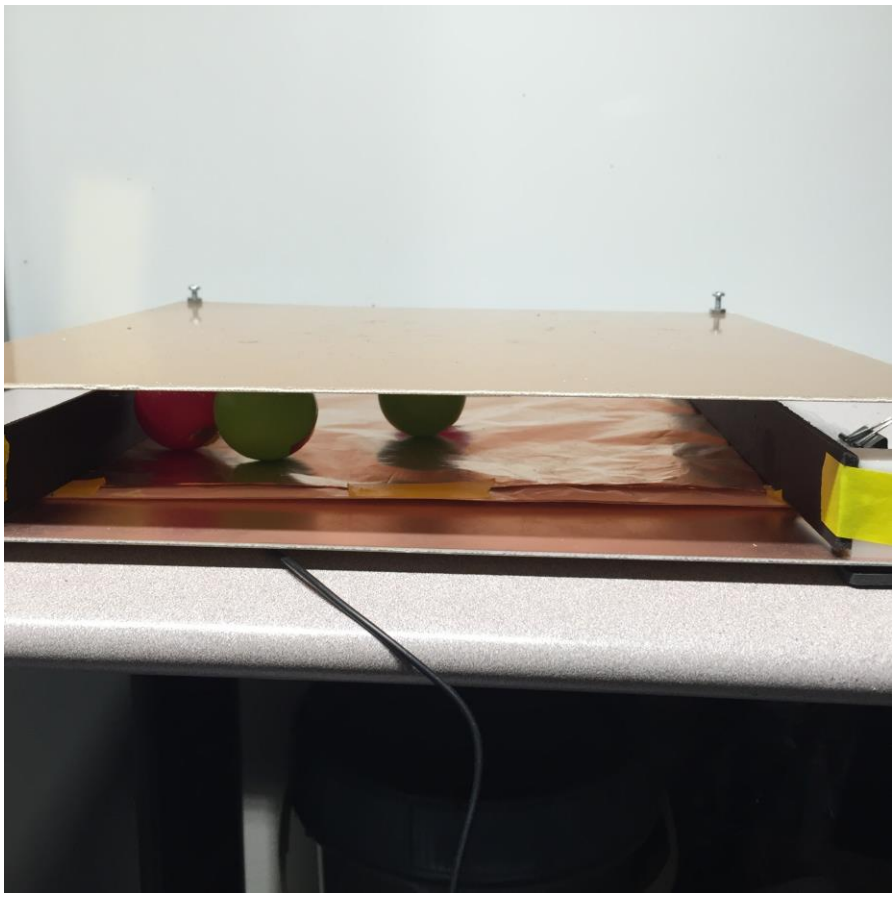

Figure 6.5 Overview of prototype 1.

An improved version of the spherical configuration bubble battery system was built later that was powerful enough to lift heavy objects such as one gallon water (Figure 6.6). In this prototype, the ping-pong balls were replaced by 3D-printed plastic shells. Each battery can provide 12V voltage output and 0.1A continuous current by connecting four coin cells in series inside. The engagement mechanism was improved by using movable plates powered by an

electronics-controlled stepper motor. The operation of the system can be smoothly achieved with buttons on the control pad.

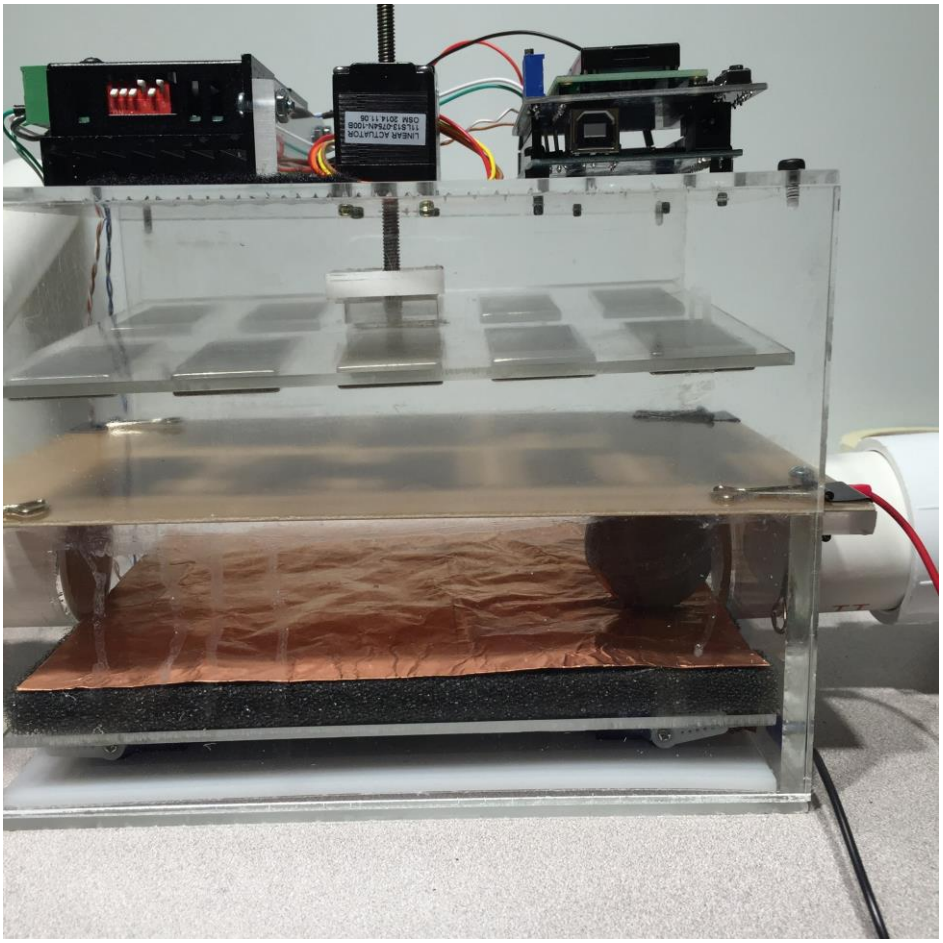

Figure 6.6 Overview of prototype 2

A new goal was proposed by our research partner at Denso to build a prototype that is powerful enough to drive an electric golf cart. As a first step of design, a quick search was done to find the proper golf cart to provide the power and energy requirement parameters. As a result, the Club Car i2 was recommended based on its lightweight and reasonable motor output. It is built based on aluminum frame and has a 48 motor with a power of 2.4kW. The original battery pack is six 8V batteries, with each cell rated at 165Ah under 0.05C (About 100Ah under 0.75C). The draw current by the motor is about 50A, with a peak current 300A. The rated range of

driving per charge is about 0.5h, which means the usable capacity of the battery pack is only about 25Ah. The battery package occupies 90cm*40cm*30cm space. The goal is to build an equivalent battery package with bubble battery design.

We proposed a cylindrical configuration for the bubble battery (Figure 6.7). Instead of putting the alignment magnet on the side of the cylinder shell, the magnet is attached to one end of the cylinder. The batteries flowing in would be sorted by rotating sideways (Figure 6.8). Then they would be in the correct orientation before entering the discharging station. A curved surface was used to make the rotation easier. Each cylinder bubble battery would provide 25.9V voltage output, 10A continuous discharging current and 2.5Ah capacity.

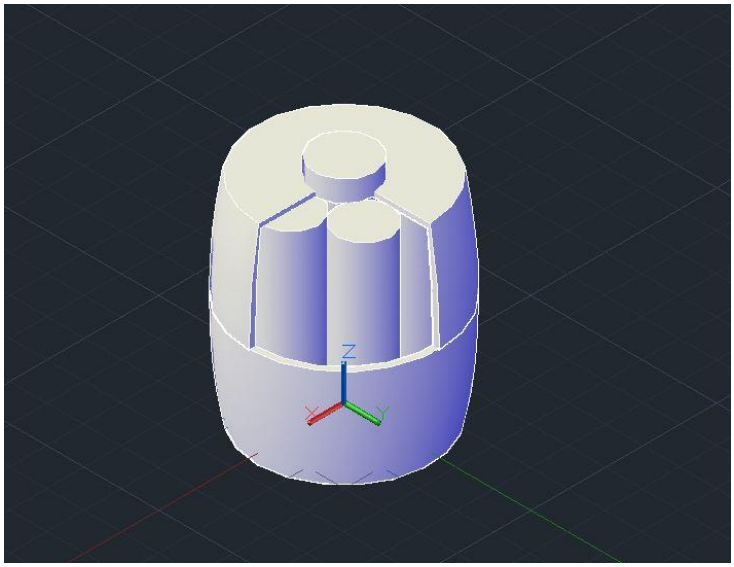

Figure 6.7 Cylindrical bubble battery.

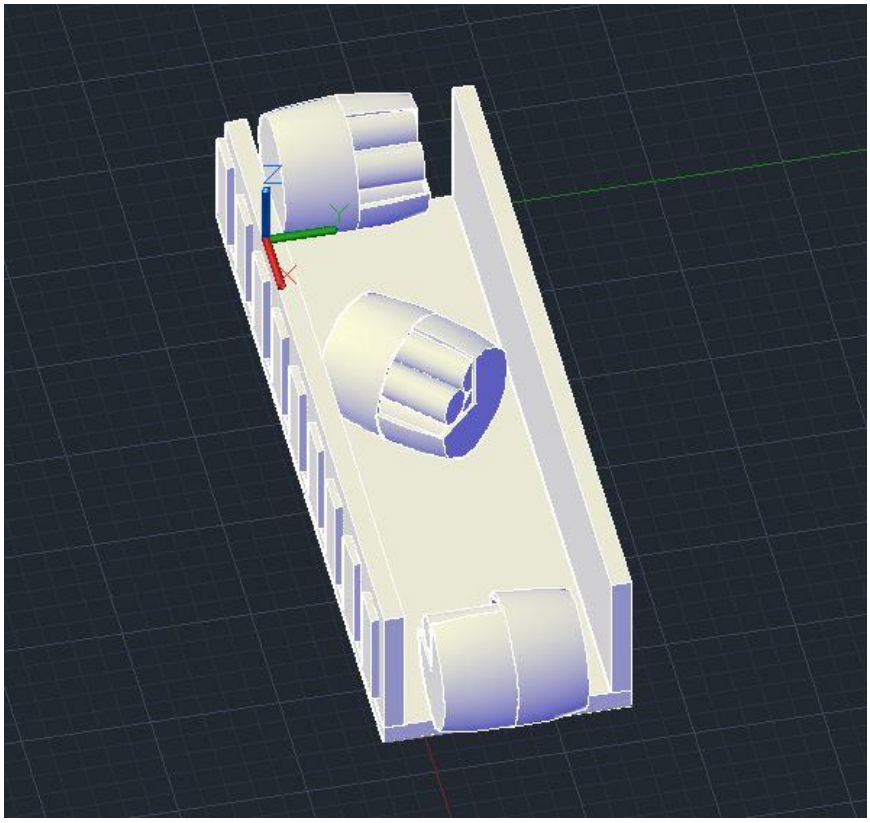

Figure 6.8 Illustration of the orienting process

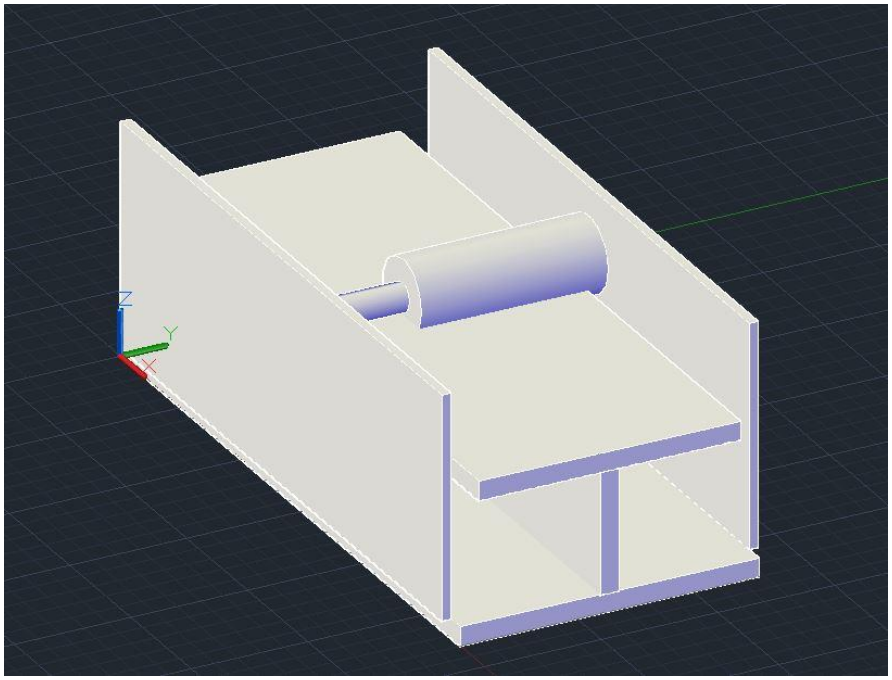

Figure 6.9 Engagement Layer

The discharge station was also modified to accommodate the new battery configuration. Vertical movement of the current collecting plates was replaced with horizontal movement (Figure 6.9). Acrylic was used as the main material to build the station.

A picture of the sample cylindrical bubble battery is shown in Figure 6.10. Thick copper foil was used as electrode on both ends. The black and white colors of 3D printing materials were to indicate positive and negative sides respectively.

Figure 6.10 A sample cylindrical bubble battery

The AutoCAD design image was shown in Fig. 6.11. Four layers were included in the unit. The top layer is a temporary tank that stores batteries with random orientations. The second layer will sort every battery that flows by into the correct orientation. The third layer will be a

temporary tank for the correctly oriented batteries. The bottom layer is for the engagement and discharge. The unit can be connected to channels via the inlet and outlet for battery to flow in and out.

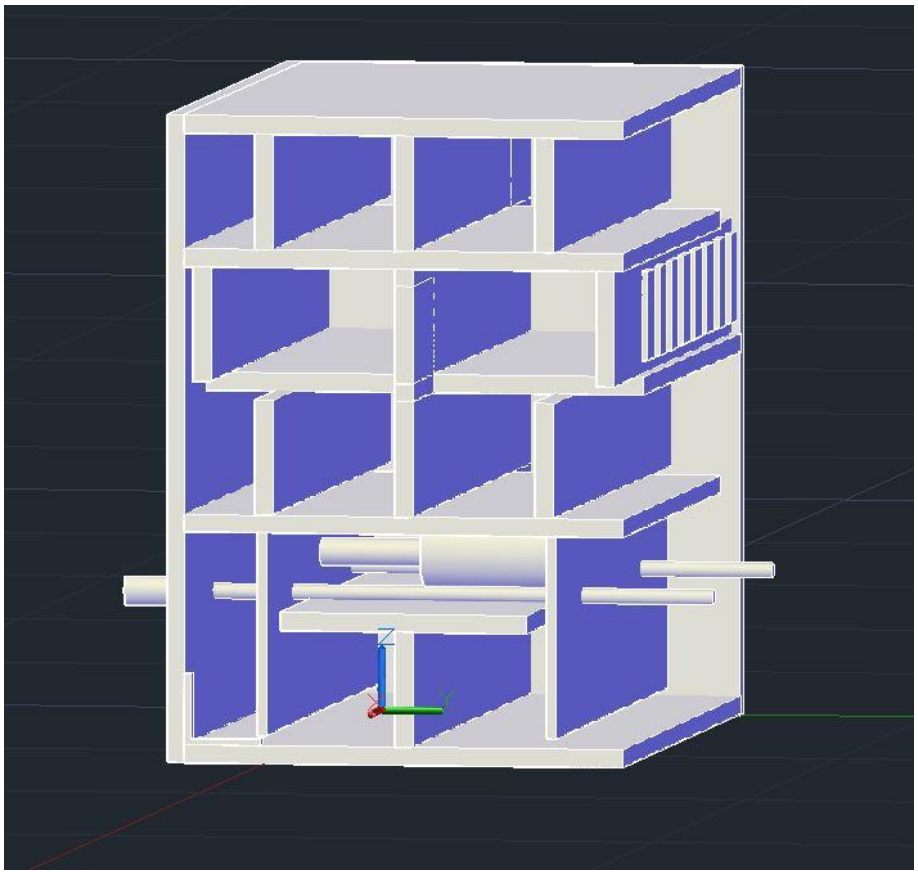

Figure 6.11 Overview of the AutoCAD design.

Two angles of the discharge station were shown in Figure 6.12. Copper braids were used as current collector on the engagement layer.

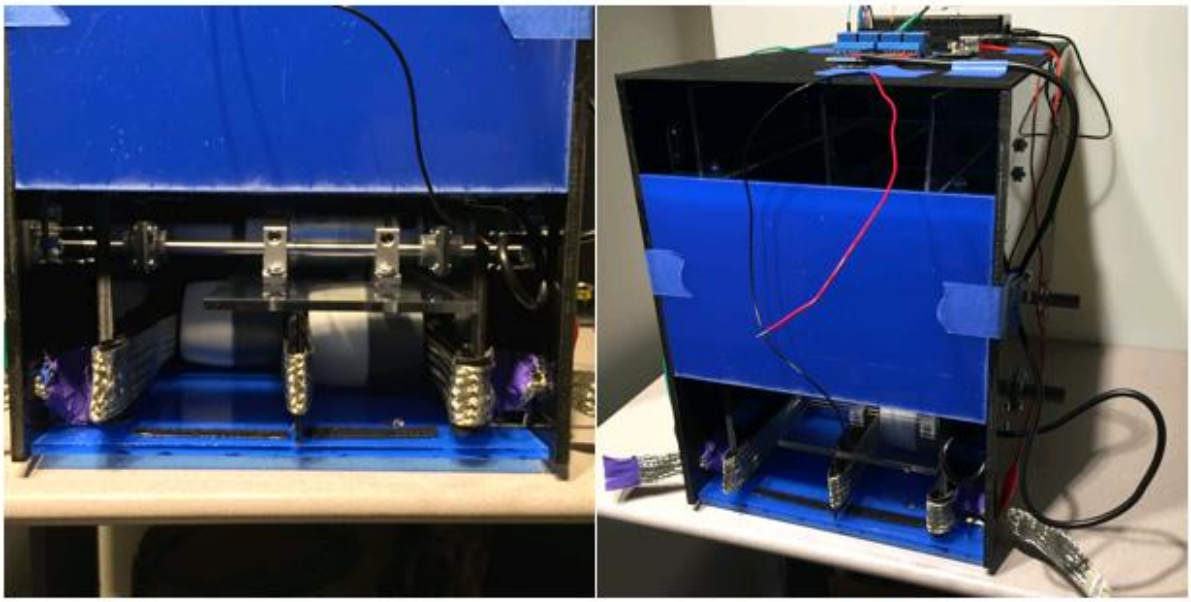

Figure 6.12 Overview of prototype 3.

A test was run to show that the package indeed can provide 56V voltage output and 50A current. One major challenge in this prototype is that the stainless steel cases used in the 18650 cylindrical cells are causing problems in the magnetic alignments. It can be eliminated if we go to smaller scale and manufacture the micro batteries using materials that are not attractive to magnets. In fact, alignment would be much easier with smaller size bubble batteries due to the reduced weight.

6.4 Conclusion

In summary, the micro battery system discussed in this letter can potentially resolve several major challenges in the conventional battery pack. Our analysis suggests that it can provide higher energy and power density while at the same time provides unique capabilities such as battery scaling with vehicle life, superfast refilling or “charging”, efficient battery

operation, ongoing battery recycling, heat self-dissipation, and flexible geometry. Three iteration of prototypes were made to demonstrate the alternatives of engaging the bubble batteries. The prototypes were proved to be able to support the power requirements. Potentially, lithium metal battery could be an ideal candidate chemistry for the bubble batteries to maximize the energy density advantage.

Chapter 7

Conclusions and Future Work

7.1 Conclusions

In this dissertation, the role of mechanical stress and deformation in lithium metal battery design is thoroughly studied. At the start, the failure mechanisms of lithium metal battery were studied with in-situ cell and material characterization methods. The in-situ cell was able to provide real time observation of the lithium metal surface morphology evolution, which showed that lithium dendrite could penetrate the separator and cause short circuit. At the same time, as the dendrite might break away from the substrate, Coulomb efficiency is lost. SEI growth turned out to be highly coupled with the dendrite growth process in lithium metal battery, where the large volume change associated with the lithium deposition and dissolution would crack the SEI, leading to reformation of SEI and thus more impedance growth.

With the insights from the experimental study, two models were developed to analyze the dendrite suppression problem. The first model simulated the concurrent evolution of dendrite morphology and SEI layer, and the results revealed that the coupling between dendrite growth and SEI penetration is a positive feedback. As the SEI gets stretched, the cracked area would have larger deposition current comparing to the flat region where the SEI layer is intact, thus further promoting dendrite growth. The broken down SEI film would get repaired again with new SEI formation, thus leading to more impedance growth over time. The V shape formed naturally at the bottom of the dendrite also explained why it is easy to have dead lithium as

dendrite can break away from the substrate easily. The second model was based on linear stability analysis, and the results provided design criterion for thin film aiming to suppress the dendrite growth effectively. The analysis explained why many current solid electrolytes fail due to the lack of thickness or modulus.

The modeling work motivates the exploration of new strategies to suppress lithium dendrite growth. Piezoelectric feedback mechanism was proposed and tested with porous PVDF film as separator. A counter overpotential would form across the piezoelectric film when the dendrite deforms the film locally. The piezoelectric overpotential then cancels out the concentration overpotential and can effectively suppress further dendrite growth.

At last, a novel battery system design with many micro batteries carried by an inert fluid was proposed to achieve higher energy and power density than conventional pack design. Theoretical analysis proved that the new system design also has advantages in battery scaling with vehicle life, superfast refilling or "charging", efficient battery operation, ongoing battery recycling, heat self-dissipation, and flexible geometry. Three prototype systems were fabricated to demonstrate the feasibility of the design.

7.2 Future Work

Models developed in this dissertation can be augmented further to 3D structure simulation, which could produce results even closer to the observed lithium dendrite structures. Surface energy anisotropy is possibly a reason why the deposited lithium prefers certain orientation and grain size, thus might be the root cause of dendritic deposition. Adding surface energy module into the modeling can potentially provide further insights in electrolyte design and SEI modification.

Piezoelectric feedback mechanism as a lithium dendrite suppression strategy is a brand new concept, which would need further testing and study to find the optimum material to serve the purpose. Combination of this mechanism with the relatively mature solid electrolyte designs may achieve impressive performance given the right tuning. This could be a new direction to explore for lithium metal researchers, and one might be able to find a solution to finally bring lithium metal battery to the market.

Appendices

Appendix A XRD results for different versions of PVDF films

To validate the XRD results for the polarized PVDF film, we did XRD analysis for three other film samples: nonpolarized PVDF, Pure PVDF and PVDF with ZnO particles embedded. As shown in Figure A.1, PVDF film with ZnO particles embedded shows strong peaks for ZnO between 30 degrees and 60 degrees. On the other hand, nonpolarized PVDF and polarized PVDF films show consistent peaks for the corresponding phases of PVDF similar to those of pure PVDF film. This proves that the PVDF film used in the follow up experiments indeed free of ZnO particles and process the desired phase for piezoelectric feedback properties.

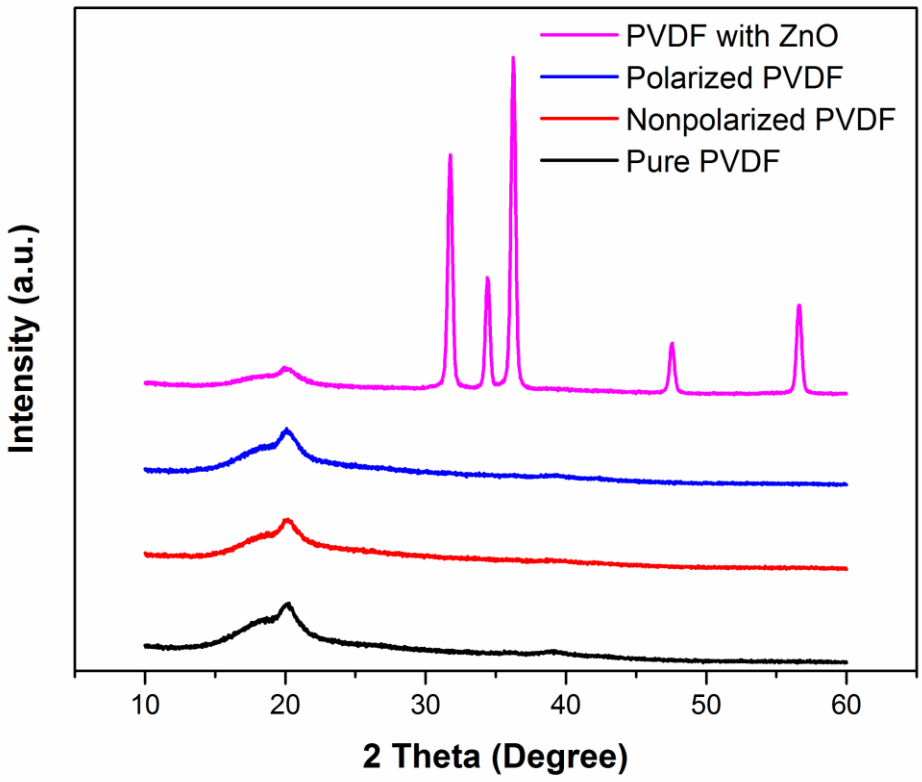

Figure A.0.1 Comparison of XRD Results for (i) PVDF film with ZnO particles embedded; (ii) Polarized PVDF film with ZnO removed; (iii) Non-Polarized PVDF film with ZnO removed; (iv)

Pure PVDF film. Both polarized PVDF and Non-Polarized PVDF films show clear removal of ZnO and same peaks as the pure PVDF film.

Appendix B Cell assembly tips for polarized piezoelectric films

Due to the transparency, it would be hard to distinguish the orientation of polarization for PVDF films when assemble the cells with them. To deal with this challenge, the following procedures were developed. For in-situ cell, the film was cut into square shape, and a slight mark was cut on the edge of the square to indicate the polarization orientation (Figure A.2 (a)). This shape and marking cut insured that the correct orientation of the film can be identified even after the film was soaked in electrolyte and turned into transparent film. For coin cell, the film was cut into round shape, and an extra tail oriented to one direction (Figure A.2 (b)). This also insured the identification of the polarized orientation of the film. The extra tail was then cut off after the film was placed in the coin cell for consistency.

(a) (b)

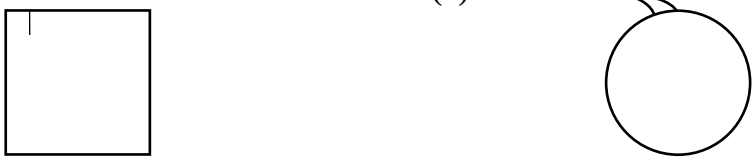

Figure A.0.2 (a) Schematics of marking cut to indicate the orientation of the film for in-situ cell fabrication. In this case, when put in this orientation, the front surface is the "+" side of the film and the back surface is the "– "side of the film, so that there would be a polarization voltage when the film is squeezed with pressure. (b) Schematics of marking tail to indication the orientation of the film for coin cell fabrication. In this case, when put in this orientation, the front surface is the "+" side of the film and the back surface is the "– "side of the film, so that there would be a polarization voltage when the film is squeezed with pressure.

Bibliography

[1] J. S. Dunning, W. H. Tiedemann, L. Hsueh, and D. N. Bennion, "A Secondary, Nonaqueous Solvent Battery," *J. Electrochem. Soc.*, vol. 118, no. 12, p. 1886, 1971.

[2] J. B. Goodenough and K.-S. Park, "The Li-Ion Rechargeable Battery: A Perspective," *J. Am. Chem. Soc.*, vol. 135, no. 4, pp. 1167–1176, Jan. 2013.

[3] A. Chrisafis and A. Vaughan, "France to ban sales of petrol and diesel cars by 2040," *The Guardian*, 06-Jul-2017.

[4] D. Lin, Y. Liu, and Y. Cui, "Reviving the lithium metal anode for high-energy batteries," *Nat. Publ. Gr.*, vol. 12, no. 3, pp. 194–206, 2017.

[5] J. Tollefson, "Car industry: Charging up the future," *Nature*, vol. 456, no. 7221, pp. 436–440, 2008.

[6] P. Albertus, S. Babinec, S. Litzelman, and A. Newman, "Status and challenges in enabling the lithium metal electrode for high-energy and low-cost rechargeable batteries," *Nat. Energy*, vol. 3, no. 1, pp. 16–21, 2018.

[7] O. Crowther and A. C. West, "Effect of Electrolyte Composition on Lithium Dendrite Growth," *J. Electrochem. Soc.*, vol. 155, no. 11, p. A806, 2008.

[8] I. Yoshimatsu, T. Hirai, and J. Yamaki, "Lithium Electrode Morphology during Cycling in Lithium Cells," no. October, pp. 2422–2427, 1988.

[9] D. Aurbach, E. Zinigrad, H. Teller, and P. Dan, “Factors Which Limit the Cycle Life of Rechargeable Lithium (Metal) Batteries,” vol. 147, no. 4, pp. 1274–1279, 2000.

[10] A. Jana, D. R. Ely, and R. E. García, “Dendrite-separator interactions in lithium-based batteries,” *J. Power Sources*, vol. 275, pp. 912–921, Nov. 2014.

[11] J.-M. Tarascon and M. Armand, “Issues and challenges facing rechargeable lithium batteries,” *Nature*, vol. 414, p. 359, Nov. 2001.

[12] G. Bieker, M. Winter, and P. Bieker, “Electrochemical in situ investigations of SEI and dendrite formation on the lithium metal anode.,” *Phys. Chem. Chem. Phys.*, vol. 17, no. 14, pp. 8670–9, 2015.

[13] D. Aurbach, B. Markovsky, A. Shechter, Y. Ein-Eli, and H. Cohen, “A Comparative Study of Synthetic Graphite and Li Electrodes in Electrolyte Solutions Based on Ethylene Carbonate-Dimethyl Carbonate Mixtures,” *J. Electrochem. Soc.* , vol. 143 , no. 12 , pp. 3809–3820, Dec. 1996.

[14] M. B. Pinson and M. Z. Bazant, “Theory of SEI Formation in Rechargeable Batteries: Capacity Fade, Accelerated Aging and Lifetime Prediction,” *J. Electrochem. Soc.*, vol. 160, no. 2, pp. A243–A250, Dec. 2012.

[15] L. Liu, J. Park, X. Lin, A. M. Sastry, and W. Lu, “A thermal-electrochemical model that gives spatial-dependent growth of solid electrolyte interphase in a Li-ion battery,” *J. Power Sources*, vol. 268, pp. 482–490, Dec. 2014.

[16] H. Park, T. Yoon, J. Mun, J. H. Ryu, J. J. Kim, and S. M. Oh, “A Comparative Study on Thermal Stability of Two Solid Electrolyte Interphase (SEI) Films on Graphite Negative Electrode,” *J. Electrochem. Soc.*, vol. 160, no. 9, pp. A1539–A1543, Jul. 2013.

[17] D. Aurbach, E. Zinigrad, Y. Cohen, and H. Teller, “A short review of failure mechanisms of lithium metal and lithiated graphite anodes in liquid electrolyte solutions,” *Solid State Ionics*, vol. 148, no. 3–4, pp. 405–416, Jun. 2002.

[18] I. Weesman, “BETWEEN SURFACE CHEMISTRY , CORRELATION MORPHOLOGY , CYCLING EFFICIENCY AND PROPERTIES OF Li ELECTRODES IN,” vol. 39, no. 1, pp. 51–71, 1994.

[19] D. Aurbach, “Review of selected electrode–solution interactions which determine the performance of Li and Li ion batteries,” *J. Power Sources*, vol. 89, no. 2, pp. 206–218, 2000.

[20] E. Zinigrad, D. Aurbach, and P. Dan, “Simulation of galvanostatic growth of polycrystalline Li deposits in rechargeable Li batteries,” *Electrochim. Acta*, vol. 46, no. 12, pp. 1863–1869, 2001.

[21] S. Frisco, D. X. Liu, A. Kumar, J. F. Whitacre, C. T. Love, K. E. Swider-Lyons, and S. Litster, “Internal Morphologies of Cycled Li-Metal Electrodes Investigated by Nano-Scale Resolution X-ray Computed Tomography,” *ACS Appl. Mater. Interfaces*, vol. 9, no. 22, pp. 18748–18757, Jun. 2017.

[22] C. T. Love, O. A. Baturina, and K. E. Swider-Lyons, “Observation of Lithium Dendrites at Ambient Temperature and Below,” *ECS Electrochem. Lett.* , vol. 4 , no. 2 , pp. A24–A27, Jan. 2015.

[23] L. Kong, Y. Xing, and M. G. Pecht, “In-situ Observations of Lithium Dendrite Growth,” *IEEE Access*, pp. 8387–8393, 2018.

[24] H. Ghassemi, M. Au, N. Chen, P. A. Heiden, and R. S. Yassar, “Real-time observation of lithium fibers growth inside a nanoscale lithium-ion battery,” *Appl. Phys. Lett.*, vol. 99, no. 12, p. 123113, Sep. 2011.

[25] K. N. Wood, E. Kazyak, A. F. Chadwick, K.-H. Chen, J.-G. Zhang, K. Thornton, and N. P. Dasgupta, “Dendrites and Pits: Untangling the Complex

Behavior of Lithium Metal Anodes through Operando Video Microscopy," *ACS Cent. Sci.*, vol. 2, no. 11, pp. 790–801, Nov. 2016.

[26] A. J. Leenheer, K. L. Jungjohann, K. R. Zavadil, J. P. Sullivan, and C. T. Harris, "Lithium Electrodeposition Dynamics in Aprotic Electrolyte Observed in Situ via Transmission Electron Microscopy," *ACS Nano*, vol. 9, no. 4, pp. 4379–4389, Apr. 2015.

[27] B. L. Mehdi, J. Qian, E. Nasybulin, C. Park, D. A. Welch, R. Faller, H. Mehta, W. A. Henderson, W. Xu, C. M. Wang, J. E. Evans, J. Liu, J.-G. Zhang, K. T. Mueller, and N. D. Browning, "Observation and Quantification of Nanoscale Processes in Lithium Batteries by Operando Electrochemical (S)TEM," *Nano Lett.*, vol. 15, no. 3, pp. 2168–2173, Mar. 2015.

[28] Y. Li, Y. Li, A. Pei, K. Yan, Y. Sun, C.-L. Wu, L.-M. Joubert, R. Chin, A. L. Koh, Y. Yu, J. Perrino, B. Butz, S. Chu, and Y. Cui, "Atomic structure of sensitive battery materials and interfaces revealed by cryo–electron microscopy," *Science (80-.).*, vol. 358, no. 6362, p. 506 LP – 510, Oct. 2017.

[29] J. L. Barton and J. O. Bockris, "The Electrolytic Growth of Dendrites from Ionic Solutions," *Proc. R. Soc. A Math. Phys. Eng. Sci.*, vol. 268, no. 1335, pp. 485–505, 1962.

[30] J. W. Diggle, A. R. Despic, and J. O. Bockris, "The Mechanism of the Dendritic Electrocrystallization of Zinc," *J. Electrochem. Soc.* , vol. 116 , no. 11 , pp. 1503–1514, Nov. 1969.

[31] C. Monroe and J. Newman, "Dendrite Growth in Lithium/Polymer Systems: A Propagation Model for Liquid Electrolytes under Galvanostatic Conditions ," *J. Electrochem. Soc.* , vol. 150 , no. 10 , pp. A1377–A1384, Oct. 2003.

[32] C. Monroe and J. Newman, "The Effect of Interfacial Deformation on Electrodeposition Kinetics," *J. Electrochem. Soc.* , vol. 151 , no. 6 , pp. A880–A886, Jun. 2004.

[33] C. Monroe and J. Newman, "The Impact of Elastic Deformation on Deposition Kinetics at Lithium/Polymer Interfaces," *J. Electrochem. Soc.*, vol. 152, no. 2, p. A396, 2005.

[34] A. Ferrese, P. Albertus, J. Christensen, and J. Newman, "Lithium Redistribution in Lithium-Metal Batteries," *J. Electrochem. Soc.* , vol. 159 , no. 10 , pp. A1615–A1623, Jan. 2012.

[35] a. Ferrese and J. Newman, "Mechanical Deformation of a Lithium-Metal Anode Due to a Very Stiff Separator," *J. Electrochem. Soc.*, vol. 161, no. 9, pp. A1350–A1359, Jun. 2014.

[36] J.-N. Chazalviel, "Electrochemical aspects of the generation of ramified metallic electrodeposits," *Phys. Rev. A*, vol. 42, no. 12, pp. 7355–7367, Dec. 1990.

[37] C. Brissot, M. Rosso, J.-N. Chazalviel, and S. Lascaud, "Dendritic growth mechanisms in lithium/polymer cells," *J. Power Sources*, vol. 81–82, pp. 925–929, Sep. 1999.

[38] C. Brissot, M. Rosso, J. -N. Chazalviel, and S. Lascaud, " In Situ Concentration Cartography in the Neighborhood of Dendrites Growing in Lithium/Polymer-Electrolyte/Lithium Cells," *J. Electrochem. Soc.* , vol. 146 , no. 12 , pp. 4393–4400, Dec. 1999.

[39] J. Yamaki, S. Tobishima, K. Hayashi, K. Saito, Y. Nemoto, and M. Arakawa, "A consideration of the morphology of electrochemically deposited lithium in an organic electrolyte," *J. Power Sources*, vol. 74, no. 2, pp. 219–227, Aug. 1998.

[40] L. Chen, H. W. Zhang, L. Y. Liang, Z. Liu, Y. Qi, P. Lu, J. Chen, and L.-Q. Chen, "Modulation of dendritic patterns during electrodeposition: A nonlinear phase-field model," *J. Power Sources*, vol. 300, pp. 376–385, Dec. 2015.

[41] R. Aogaki and T. Makino, “Theory of powdered metal formation in electrochemistry—morphological instability in galvanostatic crystal growth under diffusion control,” *Electrochim. Acta*, vol. 26, no. 11, pp. 1509–1517, Nov. 1981.

[42] L.-G. Sundström and F. H. Bark, “On morphological instability during electrodeposition with a stagnant binary electrolyte,” *Electrochim. Acta*, vol. 40, no. 5, pp. 599–614, Apr. 1995.

[43] M. Haataja, D. J. Srolovitz, and A. B. Bocarsly, “Morphological Stability during Electrodeposition,” *J. Electrochem. Soc.*, vol. 150, no. 10, p. C708, 2003.

[44] M. Haataja, D. J. Srolovitz, and A. B. Bocarsly, “Morphological Stability during Electrodeposition: II. Additive Effects ,” *J. Electrochem. Soc.* , vol. 150 , no. 10 , pp. C708–C716, Oct. 2003.

[45] Z. Li, J. Huang, B. Yann Liaw, V. Metzler, and J. Zhang, “A review of lithium deposition in lithium-ion and lithium metal secondary batteries,” *J. Power Sources*, vol. 254, pp. 168–182, May 2014.

[46] X.-B. Cheng, R. Zhang, C.-Z. Zhao, F. Wei, J.-G. Zhang, and Q. Zhang, “A Review of Solid Electrolyte Interphases on Lithium Metal Anode,” *Adv. Sci.*, vol. 3, no. 3, p. 1500213, 2016.

[47] M. Kerner, N. Plylahan, J. Scheers, and P. Johansson, “Thermal stability and decomposition of lithium bis(fluorosulfonyl)imide (LiFSI) salts,” *RSC Adv.*, vol. 6, no. 28, pp. 23327–23334, 2016.

[48] I. A. Shkrob, Y. Zhu, T. W. Marin, and D. Abraham, “Reduction of Carbonate Electrolytes and the Formation of Solid-Electrolyte Interface (SEI) in Lithium-Ion Batteries. 1. Spectroscopic Observations of Radical Intermediates Generated in One-Electron Reduction of Carbonates,” *J. Phys. Chem. C*, vol. 117, no. 38, pp. 19255–19269, Sep. 2013.

[49] P. Murmann, R. Schmitz, S. Nowak, N. Ignatiev, P. Sartori, I. Cekic-Laskovic, and M. Winter, "Electrochemical Performance and Thermal Stability Studies of Two Lithium Sulfonyl Methide Salts in Lithium-Ion Battery Electrolytes," *J. Electrochem. Soc.* , vol. 162 , no. 9 , pp. A1738–A1744, Jan. 2015.

[50] J. J. Hu, G. K. Long, S. Liu, G. R. Li, and X. P. Gao, "A LiFSI–LiTFSI binary-salt electrolyte to achieve high capacity and cycle stability for a Li–S battery," *Chem. Commun.*, vol. 50, no. 93, pp. 14647–14650, 2014.

[51] N. Takenaka, Y. Suzuki, H. Sakai, and M. Nagaoka, "On Electrolyte-Dependent Formation of Solid Electrolyte Interphase Film in Lithium-Ion Batteries: Strong Sensitivity to Small Structural Difference of Electrolyte Molecules," *J. Phys. Chem. C*, vol. 118, no. 20, pp. 10874–10882, May 2014.

[52] L. Suo, Y.-S. Hu, H. Li, M. Armand, and L. Chen, "A new class of Solvent-in-Salt electrolyte for high-energy rechargeable metallic lithium batteries," *Nat Commun*, vol. 4, p. 1481, Feb. 2013.

[53] J. Qian, W. a Henderson, W. Xu, P. Bhattacharya, M. Engelhard, O. Borodin, and J.-G. Zhang, "High rate and stable cycling of lithium metal anode.," *Nat. Commun.*, vol. 6, p. 6362, 2015.

[54] J. Heine, P. Hilbig, X. Qi, P. Niehoff, M. Winter, and P. Bieker, "Fluoroethylene Carbonate as Electrolyte Additive in Tetraethylene Glycol Dimethyl Ether Based Electrolytes for Application in Lithium Ion and Lithium Metal Batteries," *J. Electrochem. Soc.* , vol. 162 , no. 6 , pp. A1094–A1101, Jan. 2015.

[55] L. Suo, W. Xue, M. Gobet, S. G. Greenbaum, C. Wang, Y. Chen, W. Yang, Y. Li, and J. Li, "Fluorine-donating electrolytes enable highly reversible 5-V-class Li metal batteries," *Proc. Natl. Acad. Sci.*, Jan. 2018.

[56] K. Kanamura, S. Shiraishi, and Z. Takehara, "Electrochemical deposition of

lithium metal in nonaqueous electrolyte containing (C2H5)4NF(HF)4 additive," *J. Fluor. Chem.*, vol. 87, no. 2, pp. 235–243, 1998.

[57] Y. Lu, Z. Tu, J. Shu, and L. A. Archer, "Stable lithium electrodeposition in salt-reinforced electrolytes," *J. Power Sources*, vol. 279, pp. 413–418, 2015.

[58] C. Snehashis and A. L. A., "Lithium Fluoride Additives for Stable Cycling of Lithium Batteries at High Current Densities," *Adv. Electron. Mater.*, vol. 2, no. 2, p. 1500246, Feb. 2016.

[59] Y. V. Mikhaylik and I. Kovalev, "High Energy Rechargeable Li-S Cells for EV Application: Status, Remaining Problems and Solutions," *US Pat. no. US2006208701-A1*, 2006.

[60] W. Li, H. Yao, K. Yan, G. Zheng, Z. Liang, Y.-M. Chiang, and Y. Cui, "The synergetic effect of lithium polysulfide and lithium nitrate to prevent lithium dendrite growth," *Nat. Commun.*, vol. 6, p. 7436, Jun. 2015.

[61] L. Zhen, Y. Lixia, Y. Ziqi, S. Yongming, L. Yang, J. Yan, S. Yue, X. Ying, Z. Zhaoliang, and H. Yunhui, "Insight into the Electrode Mechanism in Lithium-Sulfur Batteries with Ordered Microporous Carbon Confined Sulfur as the Cathode," *Adv. Energy Mater.*, vol. 4, no. 7, p. 1301473, May 2014.

[62] G. Zheng, S. W. Lee, Z. Liang, H.-W. Lee, K. Yan, H. Yao, H. Wang, W. Li, S. Chu, and Y. Cui, "Interconnected hollow carbon nanospheres for stable lithium metal anodes.," *Nat. Nanotechnol.*, vol. 9, no. 8, pp. 618–623, Aug. 2014.

[63] G. A. Umeda, E. Menke, M. Richard, K. L. Stamm, F. Wudl, and B. Dunn, "Protection of lithium metal surfaces using tetraethoxysilane," *J. Mater. Chem.*, vol. 21, no. 5, pp. 1593–1599, 2011.

[64] G. Ma, Z. Wen, Q. Wang, C. Shen, J. Jin, and X. Wu, "Enhanced cycle performance of a Li–S battery based on a protected lithium anode," *J. Mater. Chem. A*, vol. 2, no. 45, pp. 19355–19359, 2014.

[65] G. Ma, Z. Wen, M. Wu, C. Shen, Q. Wang, J. Jin, and X. Wu, “A lithium anode protection guided highly-stable lithium–sulfur battery,” *Chem. Commun.*, vol. 50, no. 91, pp. 14209–14212, 2014.

[66] A. Manuel Stephan and K. S. Nahm, “Review on composite polymer electrolytes for lithium batteries,” *Polymer (Guildf).*, vol. 47, no. 16, pp. 5952–5964, 2006.

[67] A. Sakuda, A. Hayashi, and M. Tatsumisago, “Sulfide Solid Electrolyte with Favorable Mechanical Property for All-Solid-State Lithium Battery,” *Sci. Rep.*, vol. 3, p. 2261, Jul. 2013.

[68] N. Kamaya, K. Homma, Y. Yamakawa, M. Hirayama, R. Kanno, M. Yonemura, T. Kamiyama, Y. Kato, S. Hama, K. Kawamoto, and A. Mitsui, “A lithium superionic conductor,” *Nat. Mater.*, vol. 10, p. 682, Jul. 2011.

[69] M. F., H. A., T. K., and T. M., “New, Highly Ion-Conductive Crystals Precipitated from Li2S–P2S5 Glasses,” *Adv. Mater.*, vol. 17, no. 7, pp. 918–921, Mar. 2005.

[70] H. Akitoshi, H. Shigenori, M. Hideyuki, T. Masahiro, and M. Tsutomu, “Preparation of Li2S–P2S5 Amorphous Solid Electrolytes by Mechanical Milling,” *J. Am. Ceram. Soc.*, vol. 84, no. 2, pp. 477–479, Dec. 2004.

[71] R. Kanno and M. Murayama, “Lithium Ionic Conductor Thio-LISICON: The Li2 S - GeS2 - P 2 S 5 System ,” *J. Electrochem. Soc.* , vol. 148 , no. 7 , pp. A742–A746, Jul. 2001.

[72] G. M. Stone, S. A. Mullin, A. A. Teran, D. T. Hallinan, A. M. Minor, A. Hexemer, and N. P. Balsara, “Resolution of the Modulus versus Adhesion Dilemma in Solid Polymer Electrolytes for Rechargeable Lithium Metal Batteries,” *J. Electrochem. Soc.* , vol. 159 , no. 3 , pp. A222–A227, Jan. 2012.

[73] Y. Zhu, X. He, and Y. Mo, "Origin of Outstanding Stability in the Lithium Solid Electrolyte Materials: Insights from Thermodynamic Analyses Based on First-Principles Calculations," *ACS Appl. Mater. Interfaces*, vol. 7, no. 42, pp. 23685–23693, Oct. 2015.

[74] E. Quartarone and P. Mustarelli, "Electrolytes for solid-state lithium rechargeable batteries: recent advances and perspectives," *Chem. Soc. Rev.*, vol. 40, no. 5, p. 2525, 2011.

[75] M. W. H., "Polymer Electrolytes for Lithium-Ion Batteries," *Adv. Mater.*, vol. 10, no. 6, pp. 439–448, Jan. 1999.

[76] A. N. B., K. Shintaro, J. Edward, T. L. E., V. Kumar, R. Maria-Louisa, K. Miriam, S. Meike, S. Wolfgang, W. W. W., B. D. S., S. J. Campbell, M. R. D., and K. Ho-Cheol, "Flexible Ion-Conducting Composite Membranes for Lithium Batteries," *Adv. Energy Mater.*, vol. 5, no. 14, p. 1500265, May 2015.

[77] K. (Kelvin) Fu, Y. Gong, J. Dai, A. Gong, X. Han, Y. Yao, C. Wang, Y. Wang, Y. Chen, C. Yan, Y. Li, E. D. Wachsman, and L. Hu, "Flexible, solid-state, ion-conducting membrane with 3D garnet nanofiber networks for lithium batteries," *Proc. Natl. Acad. Sci.*, vol. 113, no. 26, p. 7094 LP – 7099, Jun. 2016.

[78] W. Zhou, S. Wang, Y. Li, S. Xin, A. Manthiram, and J. B. Goodenough, "Plating a Dendrite-Free Lithium Anode with a Polymer/Ceramic/Polymer Sandwich Electrolyte," *J. Am. Chem. Soc.*, vol. 138, no. 30, pp. 9385–9388, Aug. 2016.

[79] R. Bouchet, S. Maria, R. Meziane, A. Aboulaich, L. Lienafa, J.-P. Bonnet, T. N. T. Phan, D. Bertin, D. Gigmes, D. Devaux, R. Denoyel, and M. Armand, "Single-ion BAB triblock copolymers as highly efficient electrolytes for lithium-metal batteries," *Nat. Mater.*, vol. 12, p. 452, Mar. 2013.

[80] M. Singh, O. Odusanya, G. M. Wilmes, H. B. Eitouni, E. D. Gomez, A. J.

Patel, V. L. Chen, M. J. Park, P. Fragouli, H. Iatrou, N. Hadjichristidis, D. Cookson, and N. P. Balsara, "Effect of Molecular Weight on the Mechanical and Electrical Properties of Block Copolymer Electrolytes," *Macromolecules*, vol. 40, no. 13, pp. 4578–4585, Jun. 2007.

[81] L. Yingying, D. S. K., M. S. S., and A. L. A., "Ionic Liquid-Nanoparticle Hybrid Electrolytes and their Application in Secondary Lithium-Metal Batteries," *Adv. Mater.*, vol. 24, no. 32, pp. 4430–4435, Aug. 2012.

[82] L. Yingying, K. Kevin, K. Yu, T. Zhengyuan, and A. L. A., "Ionic-Liquid–Nanoparticle Hybrid Electrolytes: Applications in Lithium Metal Batteries," *Angew. Chemie*, vol. 126, no. 2, pp. 498–502, Nov. 2013.

[83] S. Choudhury, R. Mangal, A. Agrawal, and L. A. Archer, "A highly reversible room-temperature lithium metal battery based on crosslinked hairy nanoparticles," *Nat. Commun.*, vol. 6, p. 10101, 2015.

[84] E. Peled, "The Electrochemical Behavior of Alkali and Alkaline Earth Metals in Nonaqueous Battery Systems—The Solid Electrolyte Interphase Model," *J. Electrochem. Soc.* , vol. 126 , no. 12 , pp. 2047–2051, Dec. 1979.

[85] D. Lu, Y. Shao, T. Lozano, W. D. Bennett, G. L. Graff, B. Polzin, J. Zhang, M. H. Engelhard, N. T. Saenz, W. A. Henderson, P. Bhattacharya, J. Liu, and J. Xiao, "Failure Mechanism for Fast-Charged Lithium Metal Batteries with Liquid Electrolytes," *Adv. Energy Mater.*, vol. 5, no. 3, p. 1400993, 2015.

[86] Y. S. Cohen, Y. Cohen, and D. Aurbach, "Micromorphological Studies of Lithium Electrodes in Alkyl Carbonate Solutions Using in Situ Atomic Force Microscopy," *J. Phys. Chem. B*, vol. 104, no. 51, pp. 12282–12291, Dec. 2000.

[87] M. Safari, M. Morcrette, A. Teyssot, and C. Delacourt, "Multimodal Physics-Based Aging Model for Life Prediction of Li-Ion Batteries," *J. Electrochem. Soc.* , vol. 156 , no. 3 , pp. A145–A153, Mar. 2009.

[88] X. Lin, J. Park, L. Liu, Y. Lee, A. M. Sastry, and W. Lu, "A Comprehensive Capacity Fade Model and Analysis for Li-Ion Batteries," *J. Electrochem. Soc.* , vol. 160 , no. 10 , pp. A1701–A1710, Jan. 2013.

[89] R. Mogi, M. Inaba, S.-K. Jeong, Y. Iriyama, T. Abe, and Z. Ogumi, "Effects of Some Organic Additives on Lithium Deposition in Propylene Carbonate," *J. Electrochem. Soc.* , vol. 149 , no. 12 , pp. A1578–A1583, Dec. 2002.

[90] I. Epelboin, M. Froment, M. Garreau, J. Thevenin, and D. Warin, "Behavior of Secondary Lithium and Aluminum-Lithium Electrodes in Propylene Carbonate," *J. Electrochem. Soc.* , vol. 127 , no. 10 , pp. 2100–2104, Oct. 1980.

[91] C. Monroe and J. Newman, "Dendrite Growth in Lithium/Polymer Systems," *J. Electrochem. Soc.*, vol. 150, no. 10, p. A1377, 2003.

[92] D. Aurbach, A. Zaban, Y. Gofer, Y. E. Ely, I. Weissman, O. Chusid, and O. Abramson, "Recent studies of the lithium-liquid electrolyte interface Electrochemical, morphological and spectral studies of a few important systems," *J. Power Sources*, vol. 54, no. 1, pp. 76–84, Mar. 1995.

[93] K. Hayashi, Y. Nemoto, S. Tobishima, and J. Yamaki, "Mixed solvent electrolyte for high voltage lithium metal secondary cells," *Electrochim. Acta*, vol. 44, no. 14, pp. 2337–2344, Mar. 1999.

[94] D. Aurbach, I. Weissman, A. Zaban, and O. Chusid, "Correlation between surface chemistry, morphology, cycling efficiency and interfacial properties of Li electrodes in solutions containing different Li salts," *Electrochim. Acta*, vol. 39, no. 1, pp. 51–71, 1994.

[95] N. P. W. Langenhuizen, "The Effect of Mass Transport on Li Deposition and Dissolution," *J. Electrochem. Soc.* , vol. 145 , no. 9 , pp. 3094–3099, Sep. 1998.

[96] R. Mogi, M. Inaba, S.-K. Jeong, Y. Iriyama, T. Abe, and Z. Ogumi, "Effects

of Some Organic Additives on Lithium Deposition in Propylene Carbonate," *J. Electrochem. Soc.* , vol. 149 , no. 12 , pp. A1578–A1583, Dec. 2002.

[97] Y. Qin, Z. Chen, J. Liu, and K. Amine, "Lithium Tetrafluoro Oxalato Phosphate as Electrolyte Additive for Lithium-Ion Cells," *Electrochem. Solid-State Lett.* , vol. 13 , no. 2 , pp. A11–A14, Feb. 2010.

[98] J. K. Stark, Y. Ding, and P. A. Kohl, "Dendrite-Free Electrodeposition and Reoxidation of Lithium-Sodium Alloy for Metal-Anode Battery," *J. Electrochem. Soc.* , vol. 158 , no. 10 , pp. A1100–A1105, Oct. 2011.

[99] W. Xu, J. Wang, F. Ding, X. Chen, E. Nasybulin, Y. Zhang, and J.-G. Zhang, "Lithium metal anodes for rechargeable batteries," *Energy Environ. Sci.*, vol. 7, no. 2, pp. 513–537, 2014.

[100] M. Wu, Z. Wen, Y. Liu, X. Wang, and L. Huang, "Electrochemical behaviors of a Li3N modified Li metal electrode in secondary lithium batteries," *J. Power Sources*, vol. 196, no. 19, pp. 8091–8097, Oct. 2011.

[101] M. B. Armand, M. J. Duclot, and P. Rigaud, "Polymer solid electrolytes: Stability domain," *Solid State Ionics*, vol. 3, pp. 429–430, 1981.

[102] E. M. Gutman, *Mechanochemistry of solid surfaces*. World Scientific, 1994.

[103] Z. Y. Huang, W. Hong, and Z. Suo, "Nonlinear analyses of wrinkles in a film bonded to a compliant substrate," *J. Mech. Phys. Solids*, vol. 53, no. 9, pp. 2101–2118, Sep. 2005.

[104] A. Ferrese and J. Newman, "Modeling Lithium Movement over Multiple Cycles in a Lithium-Metal Battery," vol. 161, no. 6, pp. 948–954, 2014.

[105] J. Wolfenstine, J. L. Allen, J. Sakamoto, D. J. Siegel, and H. Choe, "Mechanical behavior of Li-ion-conducting crystalline oxide-based solid electrolytes: a brief review," *Ionics (Kiel).*, vol. 24, no. 5, pp. 1271–1276,

2018.

[106] D. Wang, W. Zhang, W. Zheng, X. Cui, T. Rojo, and Q. Zhang, “Towards High-Safe Lithium Metal Anodes: Suppressing Lithium Dendrites via Tuning Surface Energy,” *Adv. Sci.*, vol. 4, no. 1, p. 1600168–n/a, Jan. 2017.

[107] G. Liu and W. Lu, “A Model of Concurrent Lithium Dendrite Growth, SEI Growth, SEI Penetration and Regrowth,” *J. Electrochem. Soc.*, vol. 164, no. 9, pp. A1826–A1833, 2017.

[108] F. Ding, W. Xu, G. L. Graff, J. Zhang, M. L. Sushko, X. Chen, Y. Shao, M. H. Engelhard, Z. Nie, J. Xiao, X. Liu, P. V Sushko, J. Liu, and J.-G. Zhang, “Dendrite-Free Lithium Deposition via Self-Healing Electrostatic Shield Mechanism,” *J. Am. Chem. Soc.*, vol. 135, no. 11, pp. 4450–4456, Mar. 2013.

[109] K. Murata, S. Izuchi, and Y. Yoshihisa, “An overview of the research and development of solid polymer electrolyte batteries,” *Electrochim. Acta*, vol. 45, no. 8, pp. 1501–1508, 2000.

[110] K. J. Harry, K. Higa, V. Srinivasan, and N. P. Balsara, “Influence of Electrolyte Modulus on the Local Current Density at a Dendrite Tip on a Lithium Metal Electrode,” *J. Electrochem. Soc.*, vol. 163, no. 10, pp. 2216–2224, 2016.

[111] Y. Lu, Z. Tu, and L. A. Archer, “Stable lithium electrodeposition in liquid and nanoporous solid electrolytes,” *Nat. Mater.*, vol. 13, p. 961, Aug. 2014.

[112] K. Liu, P. Bai, M. Z. Bazant, C.-A. Wang, and J. Li, “A soft non-porous separator and its effectiveness in stabilizing Li metal anodes cycling at 10 mA cm-2 observed in situ in a capillary cell,” *J. Mater. Chem. A*, vol. 5, no. 9, pp. 4300–4307, 2017.

[113] K. Liu, A. Pei, H. R. Lee, B. Kong, N. Liu, D. Lin, Y. Liu, C. Liu, P. chun Hsu, Z. Bao, and Y. Cui, “Lithium Metal Anodes with an Adaptive ‘Solid-Liquid’ Interfacial Protective Layer,” *J. Am. Chem. Soc.*, vol. 139, no. 13, pp.

4815–4820, 2017.

[114] Y. S. Kim, Y. Xie, X. Wen, S. Wang, S. J. Kim, H. K. Song, and Z. L. Wang, "Highly porous piezoelectric PVDF membrane as effective lithium ion transfer channels for enhanced self-charging power cell," *Nano Energy*, vol. 14, pp. 77–86, 2015.

[115] Y. Lu, Z. Tu, and L. A. Archer, "Stable lithium electrodeposition in liquid and nanoporous solid electrolytes," *Nat. Mater.*, vol. 13, no. 10, pp. 961–969, 2014.

[116] USABC, "EV Battery Goals," 2014. [Online]. Available: http://www.uscar.org/guest/publications.php.

[117] Tesla Motors, "Tesla model S introduction," 2014. [Online]. Available: http://www.teslamotors.com/.

[118] G. Liu, P. Powell, and W. Lu, "Nano-batteries in a carry fluid as power supply: Freeform geometry, superfast refilling, and heat self-dissipation," *Appl. Phys. Lett.*, vol. 105, no. 25, p. 253902, Dec. 2014.

[119] T. C. Hales, J. Harrison, S. McLaughlin, T. Nipkow, S. Obua, and R. Zumkeller, *Discrete Comput. Geom.*, vol. 44. 2010.

[120] A. Bezdek, W. Kuperberg, P. Gritzmann, and B. Sturmfels, *Applied Geometry and Discrete Mathematics: The Victor Klee Festschrift*. 1991.

[121] D. R. Hudson, "Density and Packing in an Aggregate of Mixed Spheres," *J. Appl. Phys.*, vol. 20, p. 154, 1949.

[122] S. Torquato, T. Truskett, and P. Debenedetti, "Is random close packing of spheres well defined?," *Phys. Rev. Lett.*, vol. 84, no. 10, pp. 2064–7, Mar. 2000.

[123] A. B. Hopkins, F. H. Stillinger, and S. Torquato, "Disordered strictly jammed binary sphere packings attain an anomalously large range of densities," *Phys. Rev. E*, vol. 88, no. 2, p. 022205, Aug. 2013.

[124] General Motors, "The Chevrolet Volt Cooling/Heating Systems Explained," 2011. [Online]. Available: http://gm-volt.com/2010/12/09/the-chevrolet-volt-coolingheating-systems-explained/.

[125] R. Yazami, *Nanomaterials for Lithium-Ion Batteries: Fundamentals and Applications*. Taylor & Francis Group, 2014.

[126] E. Bohn, T. Eckl, M. Kamlah, and R. McMeeking, "A Model for Lithium Diffusion and Stress Generation in an Intercalation Storage Particle with Phase Change," *J. Electrochem. Soc.*, vol. 160, no. 10, pp. A1638–A1652, Jul. 2013.

[127] M. Zhu, J. Park, and a. M. Sastry, "Fracture Analysis of the Cathode in Li-Ion Batteries: A Simulation Study," *J. Electrochem. Soc.*, vol. 159, no. 4, p. A492, 2012.